OROGRAPHIC PRECIPITATION OVER THE ISLAND OF OAHU

A DISSERTATION SUBMITTED TO THE GRADUATE DIVISION OF THE UNIVERSITY OF HAWAIʻI AT MĀNOA IN PARTIAL FULFILLMENT OF THE REQUIREMENTS FOR THE DEGREE OF DOCTOR OF PHILOSOPHY

IN

ATMOSPHERIC SCIENCE

DECEMBER 2017

By Thomas E. Robinson Jr.

Dissertation Committee:

Steven Businger, Chairperson

Pao-Shin Chu

Albert Kim

Tim Li

Alison Nugent

Keywords: Orographic Precipitation, Modeling, Hawaiian Weather

Acknowledgements

I would like to thank the Office of Mauna Kea Management for funding my orographic meteorology research. I am very grateful to Gary Barnes who served as a committee member before leaving the island. He helped to strengthen the content of my research. I would like to thank Michael Bell who also served as a committee member. He provided me opportunities in field campaigns such as the Hawaiian Educational Radar Opportunity (HERO), which is a major part of this research, and the Convective Transport of Active Species in the Tropics (CONTRAST). Tiziana Cherubini also played a crucial role in providing the WRF output from the Mauna Kea Weather Center, and I am thankful for her contribution as well.

Abstract

To demonstrate the relationship between orographic vertical motion and precipitation, a linear diagnostic upslope model has been developed to provide a high-resolution picture of terrain induced vertical motion and precipitation over the Island of Oahu. The model is called the Hawaiian Orographic Precipitation (HOP) model. The HOP model demonstrates that vertical motions often exist near the surface that are on the order of 10 m s^{-1}, agreeing with direct observations along the Ko‘olau Mountain ridge. The HOP model vertical motion and Orographic Rainfall Index (ORI) are correlated with precipitation during the month of February 2015, but the microphysics of the HOP model is insufficient to produce a meaningful diagnosis of the actual precipitation during that time period. The ORI and orographic vertical motion are closely related indicating that the vertical motion is more important than the moisture in determining where precipitation occurs in the area of the mountains. Three case studies demonstrate that the linear model performs well when the Froude Number is above 1, and is at its best when the precipitation is light and falls out over the mountain. The HOP model does not perform well in light wind and synoptically forced weather conditions.

The high-resolution terrain gradient from the HOP model is smoothed and applied to the Weather Research and Forecasting (WRF) model in a new method for calculating the lowest level vertical motion. During the month of January 2016, the WRF model produces less precipitation than is observed at rain gauges around the Island of Oahu, but the new method produces more precipitation than the original. During a stormy period on 09 March 2012, the new method produces a different vertical motion pattern that affects the predicted weather over the island. The skill of the modified WRF model is improved during the 09 March 2012 storm by using the new method.

Table of Contents

List of Tables

List of Figures

Introduction

The interaction of the horizontal wind with the orography of the Island of Oahu plays an important role in the distribution of clouds and precipitation. Moist adiabatic isotherms tilt upwards on the windward Koʻolau Mountains while the air rises along the slope, and isotherms slope downward on the leeward side reflecting sinking motion (Van Nguyen et al. 2010). The upward motion causes clouds and precipitation, with the precipitation pattern being strongly correlated with the shape of the mountain ridge (Schroeder 1977). Many modeling studies (Harley and Chen 2010, Murphy and Businger 2011, Van Nguyen et al. 2010) have been conducted over Oahu, but none have grid spacing higher than 0.5 km because of the computational expense of using a full physics model. This study will use a high-resolution (approximately 50 m grid spacing) linear orographic upslope model named the Hawaiian Orographic Precipitation (HOP) model to investigate the vertical wind speed caused by the interaction of an idealized horizontal wind with the topography of Oahu. The HOP model will then diagnose the vertical wind speed and the results will be compared with observations on the windward Koʻolau Mountains. A new method for calculating the lowest-level vertical motion in the Weather Research Forecasting (WRF) model will also be investigated using the HOP model terrain, and the forecast accuracy will be compared to the current operational WRF during the month of January 2016 and in a case study of the March 9, 2012 record breaking hail storm.

A. Background

1) Orographic Precipitation Over Oahu

Operational weather forecasters in Hawaiʻi have a good understanding of local effects during typical weather conditions. When atypical situations arise, the forecasters have a more difficult

time understanding what small-scale features will be produced from the island-atmosphere interaction (Robert Ballard, NWS SOO, personal communication, September 23, 2014). High-resolution modeling of the orographic effects of the Island of Oahu can provide forecasters with the insight that they lack during these uncommon events, such as terrain anchored flash floods, thunderstorms, and downslope wind storms, in addition to providing additional guidance during typical trade wind weather patterns.

The precipitation over the mountains on the Hawaiian Islands can be orders of magnitude higher than over the surrounding ocean (Kodama and Businger 1998). The most rainfall over the islands occurs above 500 m and along the slopes facing the prevailing wind. Precipitation tends to fall over an extended period of time and not just a single convective event. The absence of a trade wind inversion combined with the aforementioned factors provides the most likely scenario and location for heavy precipitation events (Kodama and Barnes 1997). Moist southeasterly winds and synoptic disturbances are often involved in flooding and are enhanced by orographic effects (Murphy and Businger 2011, Kodama and Barnes 1997, Lyman et al. 2005). Rainfall events that do not produce flooding occur within the trade wind flow (Van Nguyen et al. 2010, Chen and Nash 1994, Chen and Feng 1995).

Over Windward Oahu, rainfall distribution patterns often follow the shape of the Koʻolau Mountains, signaling a strong connection between the orography and rainfall (Schroeder 1977). During days with moderate to strong easterly winds, air travels upwards along the slopes following upward tilted adiabatic isotherms (Van Nguyen et al. 2010). This rising motion can lead to precipitation. While incoming wind speed is important, other local factors other than orography that influence rainfall on Oahu are the moisture content of the incoming air, the height of the lifted condensation level (LCL), and the height of the trade wind inversion which is related

to the cloud depth (Hartley and Chen 2010). During heavy precipitation events, conditional instability combined with strong low-level lifting provided by the eastern slopes of the Ko‘olaus produce storms that anchor to the mountains (Schroeder 1977, Murphy and Businger 2011). High-resolution modeling can quantify the strength of the vertical motion over the Ko‘olaus as well as provide information about where precipitation will most likely be enhanced by the interaction of the flow with the orography.

2) Orographic Precipitation Modeling

Houze (2012) provides a recent overview of the understanding of orographic precipitation. As air approaches a barrier, the flow can follow the slope of the barrier upwards (as opposed to being blocked). Houze shows that when air is able to follow a mountain slope upwards, clouds tend to form on the windward side of the mountain. If there is sufficient preexisting moisture embedded in the approaching air, the rising air cools, condensation occurs, and the increased water-vapor flux is converted into cloud water. After collision and coalescence occur, the cloud water is converted into precipitation. If the approaching air is unstable, convection can be triggered and anchored by the terrain.

Lin et al. (2001) shows that precipitation can be represented by:

$$P = E(wq)\frac{L_s}{c_s} \tag{1}$$

where P is the total precipitation (m), E is the precipitation efficiency, w is the change of height with time (m s^{-1}), q is the moisture (g g^{-1}), L_s is the horizontal storm scale (m), and c_s is the storm speed (m s^{-1}). Then they split w into two parts

$$w = w_{oro} + w_{env} \tag{2}$$

where w is the vertical motion, w_{oro} is the orographically enhanced vertical motion, and w_{env} is the vertical motion of the environment. Because w_{oro} is a function of mountain height h(x,y), the orographic vertical motion can be represented by

$$w_{oro} = \frac{Dh(x,y)}{Dt} = \vec{v} \cdot \nabla h \tag{3}$$

where t is time, and $\vec{v}$ is the horizontal wind vector. Lin then continues to expand the gradient of mountain height (∇h) into horizontal components so that the full equation for w_{oro} is

$$w_{oro} = u\frac{\partial h}{\partial x} + v\frac{\partial h}{\partial y} \tag{4}$$

with u and v representing the zonal and meridional wind components, respectively. With this equation for w_{oro}, Lin shows that vertical motion is generated by the horizontal wind colliding with a mountain barrier and being forced upwards. The strength of the vertical motion is dependent on the strength of the horizontal wind, the slope of the mountain, the shape of the mountain relative to the wind, and the height of the mountain.

Additional factors that influence orographic precipitation from equations 1 and 4 are high precipitation efficiency, a strong low-level jet, synoptically forced environmental lifting from a slow moving synoptic weather system, high moisture content, and instability (Lin et al. 2001). Kirshbaum and Durran (2004) found that cellular mountain storms produce higher rain rates and more average precipitation. They found cellularity was influenced by mountain width, residence time of air parcels in a cloud, the height of a convective cloud cap, and the environmental wind shear.

Nugent et al. (2014) investigated the influence of the horizontal wind on orographic precipitation using a 2D and 3D version of the WRF model using a typical sounding from the Dominica Experiment. During light wind events, orographic precipitation tends to be thermally

driven and precipitation falls on the windward and lee side. During high wind events, the precipitation is mechanically driven and precipitation tends to fall only the windward side. Wind speed was the most important factor in determining the amount of precipitation that occurs. The relative humidity is also important, but it may be increased by the faster winds causing more evaporation over the ocean. Over Dominica, the diurnal effects of heating are not that strong because the strong horizontal wind leads to mechanically driven precipitation enhancement, as opposed to a diurnal thermal cycle, such as the propagating rain band over the island of Hawaii (Chen and Feng 1995).

Watson and Lane (2012) used a mountain's concavity and length to conduct an idealized study on and the effects they have on precipitation using the WRF model. One of the idealized mountains consisted of a ridge with a length of 50 km from the maximum height to half of the maximum height in the direction along the ridge, which they called the short arm mountain. The other mountain was the same except it was twice the size in the direction along the ridge, which they called the long arm mountain. When the wind blew directly into the vertex of a short arm concave mountain with a low aspect ratio, precipitation maxima occurred over the vertex (center) of the mountain cirque. After comparing the two model runs, they found that a smaller armed mountain led to a 61% precipitation enhancement compared to just 42% for the larger. Most of the headwall features on Oahu's windward side are tall relative to their short concave arms (Fig 1).

Watson and Lane also changed the wind direction slightly to see if that would influence the location of the precipitation maximum. They found that mountain precipitation was sensitive to small changes in wind direction, with the rain standard deviations having values close to the mean. This implies that there was a lot of variance in the precipitation based on the wind

direction. The precipitation maximum also shifted to the side that was normal to the wind. The horizontal scale of the mountains in Watson and Lane's study is about 200 km, but the headwall features of the Ko'olau Mountains are generally between 1 km and 10 km and in some places they are even smaller. High-resolution modeling will show that even for small-scale concave mountain shapes, the ascent forced by the mountain is sensitive to the wind direction and will be strongest when the horizontal flow is directed towards the middle of the cirque.

There are an abundance of orographic modeling studies (Watson and Lane 2012, Van Nguyen et al. 2010, Kunz and Kottmier 2006, Schar and Smith 1993, Kirshbaum and Durran 2004, Nugent et al. 2014) with varying levels of model complexity and computational demand. All of these modeling studies relate the flow to some variation of the Froude number

$$Fr = \frac{U}{Nh} \tag{5}$$

where Fr is the Froude Number, U is the wind speed normal to the mountain (m s^{-1}), N is the Brünt-Vaisala frequency (s^{-1}), and h is the mountain height (m). When the wind speed is high and the stability is low for a mountain of constant height, the Froude number is high and air can flow up and over the barrier. When the wind is weak or there is strong static stability, the air is blocked from flowing over the mountain. Three-dimensional linear models can capture blocking (Kunz and Kottmier 2006), but upslope two-dimensional linear models cannot.

When the kinetic energy of the prevailing flow is sufficient to ascend over a mountain barrier, two-dimensional linear modeling of orographic precipitation can reasonably be applied (Hughes et al. 2009). Smith (2003) begins his derivation of a linear orographic precipitation model with vertically integrated cloud-water density $q_c(x,y)$ and hydrometeor density $q_s(x,y)$

$$\frac{Dq_c}{Dt} = S(x,y) - \frac{q_c}{\tau_c} \tag{6}$$

$$\frac{Dq_s}{Dt} = \frac{q_c}{\tau_c} - \frac{q_s}{\tau_f} = \frac{q_c}{\tau_c} - P(x,y) \tag{7}$$

where t is time, τ_c is the time constant for cloud water conversion to rain water, τ_f is the time constant for hydrometeor fallout, P is precipitation, and S is the sum of background water generation and the local generation created by terrain. Values of τ_c vary greatly and are a function of the atmospheric conditions (Jiang and Smith 2003). S is represented by

$$S(x,y) = S_\infty + C_w \vec{v} \cdot \nabla h(x,y) \tag{8}$$

where C_w is a coefficient relating condensation rate to vertical motion and S_∞ is the background moisture. Smith and Barstad (2004) further expand S using the Clausius-Clapeyron equation to get

$$S(x,y) = \frac{C_w}{H_w} \int_0^\infty w(x,y,z) e^{-\frac{z}{H_w}} dz \tag{9}$$

where H_w is the height of the center of mass of the moisture column and w(x,y,z) is the three dimensional distribution of the vertical motion. The height of the moist layer is represented by

$$H_w = \frac{R_v T_{SFC}^2}{L_v \gamma} \tag{10}$$

where T_{SFC} is the reference surface temperature (K), γ is the environmental lapse rate (K m^{-1}), L_v = 2.5 x 10^6 J kg^{-1} is the latent heat, and R_v=461 J kg^{-1} K^{-1} is the gas constant for water vapor. A freezing layer can be added within the model to provide for different phases and fall speeds of hydrometeors to improve precipitation output. (Barstad and Schuller 2011). NO HOP STUFF

B. Motivation and Goals

Because a full physics model such as WRF is too computationally expensive to run at very high resolution, a simple linear model must be used to resolve the small details of the vertical

motion along the Ko‘olau Mountains. In order to test out a Hawaiian specific model with a simpler microphysics scheme than the one used by Smith and Barstad (2004), the Hawaiian Orographic Precipitation (HOP) model is developed. This model uses the same equations as the Smith model, but a different method for calculating the microphysics. The HOP model considers the moisture where the vertical motion is lifting air, so at some height Z_{top}, $w(x,y,Z_{top})=0$ m s^{-1} and at the bottom $w(x,y,0)=w_{oro}$. The cloud top height (Z_{top}) is determined by finding where the temperature increases with height while the relative humidity drops considerably which is typically the trade wind inversion (TWI) over the Island of Oahu. Equation 9 can be solved directly, so there is no need for a Fourier transform. By using an algorithm to find the TWI as Z_{top} and solving equation 9 directly, the HOP model provides a more specific application of the linear model over the Island of Oahu.

Under resolving the terrain gradient can lead to an underestimation of precipitation (Lyman et al. 2005), so the HOP model has a horizontal grid spacing of 51.7 m x 55.6 m (0.0005° x 0.0005°), matching the resolution of data from the United States Geological Survey (USGS). The model will be able to show that the vertical motion generated by the interaction of the horizontal winds with the mountains causes very strong vertical motions near the surface, which results in precipitation enhancement. In order to show that the vertical velocities generated by the HOP model are realistic, wind observations have been taken at points along the Ko‘olau Mountains. Correlations between the HOP model output and precipitation are done to determine if the HOP model produces output that is useful for operational forecasters to use in conjunction with a full physics model as well as determining if precipitation along the Ko‘olau Mountains is a linear process.

The HOP model is great for resolving the details of the orographic vertical motion, but it is too simple to be the primary model used by operational forecasters over the Hawaiian Islands, so a full physics model such as WRF is needed to produce an actual operational forecast. The WRF model algorithm for calculating vertical motion on the lowest level is to smooth the terrain heights of higher-resolution terrain data and calculate the gradient from these heights, which leads to an under resolved terrain gradient. A new algorithm is developed to use the high-resolution terrain gradient from the HOP model, where this gradient is scaled to the WRF model domain. The enhanced terrain gradient is then used to calculate the vertical motion on the lowest sigma level of the WRF model. The high resolution terrain gradient scaling allows for more details of the terrain gradient to be preserved for this boundary condition calculation. By using a more realistic terrain gradient, the model output forecast improves.

Methods and Data

A. Observations

1) Vertical and Horizontal Wind Measurements

Several sites along windward slopes of Oahu were chosen to conduct wind measurements using a Kestrel 4500 Pocket Weather Tracker. Wind measurements were taken by holding the Kestrel up at approximately 2 m perpendicular to the ground (90°) to obtain the average wind speed and the peak wind gust for the horizontal wind. The Kestrel was also held parallel to the ground (0°) at a height of approximately 1 meter to obtain the average vertical wind speed and peak wind gust. Using a digital level, the tilt of the Kestrel was kept at ±3° from being horizontal or vertical at any given time. The locations for wind measurements (Fig 2) were the Pali Lookout (P), the Diamond Head Trail Summit (D), the windward peak of Koko Crater Summit (K), along the eastern side of the Makapu‘u Lighthouse Trail, and the backside of Koko-Head (H). Each location was selected for accessibility, safety, typical windy nature, and location on an upslope incline relative to the wind direction. Observations were made between 20 October and 27 November 2015.

2) WSR-88D Radar Data

The operational HOP model is verified by comparing the output to radar observations from the Weather Surveillance Radar – 1988 Doppler (WSR-88D) located on the Island of Moloka‘i at 21.132°N, 157.179°W (PHMO). The S-band (10.0 cm wavelength) radar has a nominal peak output of 750 kW, pulse width of 1.57 μs, and pulse repetition frequency between 318 and 1304 s^{-1} (Crum and Alberty 1993). The Level II radar data are converted to a 51.7 m x 55.6 m grid

over the Island of Oahu to match the HOP model grid, but no smoothing is applied so the resolution of the radar data is mostly unchanged.

3) Hawaiian Education Radar Opportunity Data

During the Hawaiian Educational Radar Opportunity (HERO), an X-band (3 cm) Doppler on Wheels (DOW) radar was deployed in Kahaluʻu at 157.840°W, 21.459°N (Fig 3) as part of the intense observational period 7 (IOP7) (Bell et al. 2015). The DOW was run from 2034 UTC on 03 November 2014 until 0239 UTC on 04 November 2014. IOP7's event description is listed as Kahaluʻu Orographic Trade Showers (Bell et al. 2015). A radiosonde was launched at 2140 UTC on 03 November 2014 during IOP7 of the HERO project recording height change, pressure, temperature, wind speed, and wind direction.

4) Oahu Rain Gauge Data

Daily rain gauge data from around the Island of Oahu was obtained from the National Center for Environmental Information daily summaries dataset. There were 56 rain gauges that reported rainfall data across the island. The locations of the gauges (Fig 4) are spread out across the Island of Oahu, but the majority are on the eastern windward part of the island to the east of 158°W. The data runs from January 3 – January 30, and the reports are in millimeters of rain per 24-hour period from starting at 8am the previous day. The minimum observable amount is 0.3 mm.

B. The Hawaiian Orographic Precipitation Model

1) Model Derivation

Utilizing the w_{oro} equation (4), a 51.7 m x 55.6 m grid is used to analyze the orographically induced vertical motion over Oahu. High-resolution terrain data (0.0005°) from the USGS are

used to calculate w_{oro} based on the wind fields and mountain geometry applying equation (4). The boundaries of the model are set over the ocean so that ∇h is 0 m s^{-1} and there is no orographic vertical motion. Only the horizontal winds and mountain geometry determine the calculated vertical motion for the vertical velocity calculation of the HOP model, so the effects of stability, friction, moisture, and blocking are ignored. The high-resolution vertical motion induced by the Ko‘olau mountains is quantified for the first time in this research to investigate the detailed impact the mountains have on precipitation location, initiation, and intensity. As long as flow blocking and precipitation loading are not strong at a given time, the HOP model will provide accurate orographic vertical motion output (Hughes et al. 2009).

A non-linear shallow water model can be used to assess mountain blocking (Schar and Smith 1993). Because blocking is a nonlinear process, the HOP model does not include vertical motion generated by blocking. Instead, it calculates convergence as the flow slows while approaching the mountain. The mass continuity equation on height coordinates can be used to diagnose vertical motion

$$\nabla(\rho\bar{v}) + \frac{\partial(\rho w)}{\partial z} = 0 \tag{11}$$

where ρ is the density of air. Switching to finite forward differencing in the vertical, finite center differencing in the horizontal, and assuming that vertical motion and density go to 0 at the surface (z = 0 m), the equation used by the HOP model to calculate vertical motion due to divergence over the ocean is

$$w = -\Delta z \left[\begin{array}{l} \dfrac{u(x+1,y)-u(x-1,y)}{4\Delta x} + \\ \dfrac{v(x,y+1)-v(x,y-1)}{4\Delta y} + \\ u(x,y)\dfrac{\rho(x+1,y)-\rho(x-1,y)}{4\rho(x,y)\Delta x} + \\ v(x,y)\dfrac{\rho(x,y+1)-\rho(x,y-1)}{4\rho(x,y)\Delta y} \end{array} \right] \tag{12}$$

Equation 12 is used over the ocean and where the terrain is flat.

Precipitation is added to the model by starting with the linear model from Smith and Barstad (2004). The orographic precipitation is calculated starting from equation (9) and by considering only the moisture where the vertical motion is due to the orographic vertical motion process to the top of the cloud. At some height Z_{top}, $w(x,y,Z_{top}) = 0$ m s^{-1} while $w(x,y,0) = w_{oro}$. In the HOP model, the cloud top height (Z_{top}) is determined by finding where the temperature increases with height while the relative humidity drops considerably. Typically this is found to be at the height of the trade wind inversion (TWI) and finding it follows the procedure set out by Cao, et al. (2007). In the case of a weak or shallow trade wind inversion, the relative humidity drop is used as a means of finding the cloud top. There is no vertical cap to finding Z_{top}, so if there is no TWI, the routine finds the first large relative humidity drop off or strong inversion to use as the cloud top. When there is no low-level stable layer, Z_{top} becomes the tropopause. By using the height of the base of the inversion, any overshooting cloud tops are ignored. In addition to finding the TWI, the lifted condensation level (LCL) can also be found using Espy's equation (Espy 1841)

$$LCL = \frac{T_s - T_{dew}}{\Gamma_d - \Gamma_{dew}} \tag{13}$$

where T_s is the surface temperature, T_{dew} is the surface dew point, Γ_d is the dry adiabatic lapse rate, and Γ_{dew} is the dew point lapse rate estimated at 2 °C km^{-1}.

The Hawaiian Orographic Precipitation model assumes a linear decay of w from the LCL to the top of the cloud, so the equation for w becomes

$$w(z) = \left(\frac{w_{oro}}{Z_{top}} z + w_{oro} \right) \tag{14}$$

making the new equation for the moisture source created due to the vertical motion induced by the mountain (and switching S to p_{oro})

$$S = p_{oro} = \frac{C_w}{H_w} \int_0^{\infty} \left[\left(\frac{w_{oro}}{Z_{top}} z + w_{oro} \right) e^{-\frac{z}{H_w}} \right] dz = w_{oro} C_w \left[\frac{(Z_{top} - H_w) + H_w e^{-\frac{Z_{top}}{H_w}}}{Z_{top}} \right] \tag{15}$$

The full precipitation for the model comes from substituting equation (15) into equation (6) and substituting the result into equation (7). This method does not use a Fourier transform like Smith's model, instead the value of each variable is calculated and plugged into the formula.

Lin et al. (2001) suggested an index for estimating where orographic precipitation will occur

$$P_o = U \frac{\partial h}{\partial x} q \tag{16}$$

where P_o is the general index for orographic precipitation, U is the low level wind, h is the mountain height, and q is the water vapor mixing ratio. This index has been further developed into the Orographic Rainfall Index (ORI), which is used by operational forecasters to locate potential areas of heavy orographic precipitation (Cooporative Institute for Research in the Atmosphere 2010).

$$ORI = TPW(\vec{v} \cdot \nabla h) \tag{17}$$

where TPW is the total precipitable water in the column (mm). The operational ORI used by the National Weather Service is calculated using the horizontal winds at 850 hPa from the Global Forecast System (GFS) model to calculate the orographic vertical motion. The HOP model will calculate ORI based on w_{oro}, so equation (17) expressed in terms of the HOP model is

$$ORI = TPW * w_{oro} \tag{18}$$

2) HOP Model Experiments

The HOP model experiments are summarized in Table 1. The first experiment (HOP1) is an idealized run of the HOP model. The horizontal winds are set to a constant 10 m s^{-1} at all altitudes across the entire domain and are then varied 360° by 5° increments. The value of w_{oro} is calculated at each grid point. The horizontal winds are then set to be 45° across the entire domain, but the speed is changed from 5 m s^{-1} to 20 m s^{-1} in increments of 5 m s^{-1}.

The second experiment (HOP2) is a run of the HOP model to calculate the w_{oro} output. The model was initialized with WRF output from the model run closest to the HOP time so that the WRF output was never more than 12 hours old. The times were selected to match the times of observations taken with the Kestrel as described in Section 1. The modeled vertical motion is compared to the observations to determine if the HOP model produces values of w_{oro} that are of the correct order of magnitude.

During the month of February 2015, the HOP3 experiment consists of daily operational HOP model runs. The model output is then compared to the 30-minute averaged radar reflectivity from the PHMO radar site. To compare the model and radar data, boxes have been created in the area of the Koʻolau Mountain Range. The locations of the boxes are numbered on the map in Fig 5. The boxes each cover 0.03° in the north-south direction and are located mostly over the

orography. The Kaneohe Peninsula, for example, is excluded because it is mostly flat and the HOP model uses the blocking equation (12) instead of the w_{oro} calculation equation (4). Within each of the boxes, the maximum averaged reflectivity can be compared to a maximum output variable from the HOP model (w_{oro}, P_{oro}, P, or ORI), and plotted. The model values are compared to the radar reflectivity to investigate the correlation. To improve the signal to noise ratio, the HOP output maxima from the boxes for a given time step are averaged, and the same averaging is done for the reflectivity maxima. The averaged HOP model output is compared to the averaged reflectivity.

A case study during the period from 0000UTC – 1800UTC on 09 March 2012 provides the scenario for the next HOP experiment (HOP4). The HOP model, using the horizontal winds and total precipitable water from the WRF model, calculates the w_{oro} and ORI to be compared with the 15 minute averaged radar reflectivities in the same way as HOP3 using the boxes from Fig 5. The HOP model also calculates the Froude number for each time step.

The next case study takes place around 2140 UTC on 03 November 2013 during the HERO IOP7. HOP5 uses winds and moisture from the HERO sounding described below in section 3, whereas HOP6 uses output from the WRF model for the same time. The w_{oro} and ORI output are compared to the corresponding precipitation cell that is observed at or downwind from the area of maximum vertical motion. If multiple vertical motion maxima are located upwind from a cell, the strongest vertical motion is used.

The final case study (HOP7) takes place on 24 August 2015 where the HOP model was run for a 24-hour period. This set up is the same as HOP4. The WRF output is used to initialize the model, and comparison to radar data is done by correlating w_{oro} and ORI to radar reflectivity in the boxes in Fig 5.

3) HOP Model Input

For experiments HOP2, HOP3, HOP4, HOP6, and HOP7, the lowest level wind output from the WRF model with 3 km grid spacing that was run operationally by the Mauna Kea Weather Center is used to initialize the HOP model. The details of the WRF model are found in the next section. All other necessary variables used in diagnosing the precipitation such as density, moisture, and temperature also come from the lowest level, LCL, and inversion level of the WRF model. Some advantages of using the WRF output to initialize HOP are that the wind comes from a full physics model where blocking is already considered, the wind field slows as it approaches the mountain causing convergence, friction is already factored into the wind field, and the moisture, wind, and density variables are all available across the entire domain. Because the wind, density, and moisture patterns are on a 3000 m grid, the large grid variables are downscaled using a bilinear interpolation, so Δx and Δy are both equal to 3000 m. The Δz term is a function of x and y and is the height of the lowest sigma level at each grid point in the WRF model, with a value of approximately 17.2 m. The operational HOP model will use WRF variables when running, so the HOP model can produce output operationally.

The HOP5 experiment uses the winds and TPW from the sounding launched during IOP7 of the HERO project. Using the assumption that the winds are only changing vertically and not horizontally, the winds at a given height in the sounding are used at the matching height on the terrain. Because the wind direction and speed only varies with height, horizontal winds are the same everywhere at a given height. The wind is linearly interpolated between two sounding data points to match a given height on the terrain. Any heights below the initialization height of the sounding are set to 0 m s^{-1}.

C. WRF Model Vertical Motion Lower Boundary Condition

1) WRF Model Set Up

The WRF model is run on a 220 x 170 single domain with 3000 m grid spacing encompassing the main Hawaiian Islands. There are 40 vertical levels spaced on the order of tens of meters for the levels nearest the ground, with first model level at ~17m above the surface, and gradually increasing in distance between levels with height. Input data for the WRF model are the one-degree National Center for Environmental Prediction (NCEP) FNL Operational Model Global Tropospheric Analyses datasets.

The WRF physics package used includes (i) WRF Single-Moment 6-class scheme, which resolves ice, snow and graupel processes suitable for high-resolution simulations (Hong and Lim, 2006); the Mellor-Yamada-Janjic (MYJ) planetary boundary layer scheme (Janjic, 2002) which solves the prognostic equation for the TKE; the RRTM longwave-shortwave radiation scheme (Mlawer et al, 1997); and a simple downward integration allowing efficiently for clouds and clear-sky absorption and scattering (Dudhia, 1989). The physics set up is the same as the set up for the Mauna Kea Weather Center operational WRF model runs.

2) WRF Modification

During each time step of the WRF model, the vertical motion near the surface is calculated in a subroutine called set_w_surface contained in the module file named module_bc_em.f90, and called by solve_em.f90. The subroutine calculates the vertical motion by taking the difference between the terrain height at the point of interest and the height at the next point in the meridional or zonal direction, multiplying the difference by the meridional or zonal wind

respectively, adding those quantities together in the given direction, dividing by double the grid spacing, and then adding the zonal and meridional components together. The equation is

$$w(i,j) = 0.5dy\left(v(i,j+1)\left[h(i,j+1) - h(i,j)\right] + v(i,j)\left[h(i,j) - h(i,j-1)\right]\right) + 0.5dx\left(u(i+1,j)\left[h(i+1,j) - h(i,j)\right] + u(i,j)\left[h(i,j) - h(i-1,j)\right]\right) \quad (19)$$

where w is the vertical motion calculated by WRF in the lowest sigma level, i and j are the points in the zonal and meridional direction, dx and dy are the WRF grid spacing in the zonal and meridional direction, u and v are the horizontal winds in the zonal and meridional direction, and h is the terrain height.

The high-resolution terrain gradient calculation from the HOP model is utilized in the new WRF vertical motion calculation. First, the distance between each point in the 51.7 m x 55.6 m HOP model grid is calculated. Next, the gradient of the terrain is found for all of the points over the Island of Oahu. Then a latitude and longitude square is formed around each point in the WRF model, and the values of the high-resolution terrain gradients in the zonal and meridional direction are averaged within each box. This causes a smoothing of the gradient in the area surrounding a grid point instead of smoothing the terrain heights by taking the value at the grid point.

A new subroutine named hires_w_surface is then added to file module_bc_em.F90. The subroutine calculates the vertical motion using the equation

$$w(i,j) = v(i,j)\frac{dh}{dy}(i,j) + u\frac{dx}{dx}(i,j) \quad (20)$$

where dh/dx and dh/dy are the averaged gradient of the terrain in the zonal and meridional direction. WRF reads in the gradient from the binary file created in the preprocessing stage described above, and then calculates the vertical motion. By using this method, other portions of

the model where the terrain would be used are unaffected, but the vertical motion calculation is more representative of the interaction between the surface wind and the slope of orography. The subroutine is called for every time step of the WRF run.

3) Model Runs

The original (CTRL) and modified (EXP) WRF models are run daily producing 30-hour forecasts starting at 1800 UTC for the month of January 2016. The first 6 hours of the forecast are ignored to allow for spin up because the initial vertical motion is calculated using the original method in both models. This allows both models to have the same initial state for all variables. After ignoring the first 6 forecast hours, the output data from each model run is a 24-hour time series starting at 0000 UTC. Model verification of precipitation is done using the rainfall observations from the National Center for Environmental Information. Any time periods without and recorded observations are ignored.

A case study is run using a WRF forecast for 24 hours starting at 0000 UTC on 09 March 2012. First, the original WRF model control run is performed. The HOP model is then set to run at 3000 m resolution using the horizontal winds from the control run to check to see if it produces a similar forecast for vertical motion. Next, the EXP model is run to compare forecasts with the CTRL run. The CTRL and EXP models are compared to the PHMO radar data to determine which produced a better nonprobabalistic forecast using a 2x2 contingency table.

HOP Model Results

A. Idealized Horizontal Winds (HOP1)

An idealized study is conducted to determine how sensitive the orographic vertical motion is to wind speed and direction. The HOP model is initialized using constant 10 m s^{-1} winds from the same direction over the entire island of Oahu. This idealized simulation is used to investigate how a particular wind direction determines the location and strength of orographically induced vertical motion. The model is run for every 5° incremental rotation in wind direction around the compass.

Because of the small cirques along the eastern side of the Koʻolaus in Fig 1, the pattern shows a shift in where vertical motion maxima are located based on the wind direction, similar to Watson and Lane (2012). The northeasterly winds in Fig 6b and Fig 6c show the most continuous response in the vertical motion along the Koʻolau Mountain Range; the other two wind directions produce intermittent breaks. The northeasterly winds (Fig 6b and Fig 6c) allow for the most widespread vertical motion, whereas the north or east wind directions produce more localized areas of enhanced vertical motion.

When the wind is blowing from the north (Fig 6a), the north facing arms of the cirques produce the vertical motion, and the east facing arms do not (Fig 6d). The opposite is true when the wind is from the east. This is most obvious to the south of the Kaneohe Peninsula. The north winds in Fig 6a produce a line of upward motion along the windward part of the Koʻolaus where the mountains are oriented mostly east to west. Contrastingly in Fig 6d, the upward motion is shifted to the valleys to the south of the feature in Fig 6a as well as to the west where the mountains are oriented in a more north to south direction. Small differences similar to these can

be seen along the whole Ko‘olau range. The strongest vertical motion occurs when the wind is blowing in the same direction as the strongest terrain gradient.

The vertical motion in the small individual cirques along the Ko‘olau Mountains is also shifted based on the wind direction. The two northern cirques between 21.40° N and 21.425° N are facing to the east and are approximately 0.01° in latitude (~1000 m) wide, and to the south is an elongated cirque that extends off of the domain (Fig 7). When the wind is from the north, the upward motion on two east facing cirques is on the southern arms. Downward motion occurs on the northern arms of the cirques. Along the southern cirque, there is very little upward motion with only a very small area above 10 m s^{-1}. When the wind is from the east (Fig 8), the upward motion in the northern cirques occurs more toward the middle of the cirque in the area that is normal to the wind. Downward motion only occurs in a small area in the second cirque to the west of a small peak, with only weak scattered downward motion happening along the arms. On the southern cirque, a relatively large area of upward motion above 10 m s^{-1} occurs along the whole east-facing portion, including the northern arm that is shared with the middle cirque.

When the wind blows from the southwest, air that follows the mountains will travel downward along the steep east face of the Ko‘olau Mountains (Fig 9). There are several areas where the downward motion reaches 10 m s^{-1} inside of the easterly-facing cirques. The mountain gradient is in the opposite direction of the southwest wind, so the terms on the right hand side of equation 3 have opposite signs. If there is flow changing from subcritical to supercritical, an abrupt change in static stability, or vertically propagating waves breaking (Durran 1990), downslope windstorms could be initiated at the locations where the downward motion is the strongest.

The second sensitivity test involves changing wind speeds. Using a 45° northeast wind, the wind speeds of 5, 10, 15, and 20 m s^{-1} were input into the HOP model and the location and magnitude of the vertical motion was calculated. This wind direction was chosen because it is representative of the prevailing northeasterly winds. The maximum vertical wind speed is 42.8 m s^{-1} and occurs during the 20 m s^{-1} horizontal wind model run (Fig 10d). At the same point in the other runs, the maximum also occurs, but is scaled down linearly from 0.25, 0.5, and 0.75 of 42.8 m s^{-1} for the 5 m s^{-1}, 10 m s^{-1}, and 15 m s^{-1} runs respectively (for example, in Fig 10c, the 42.8 m s^{-1} x 0.75 = 32.1 m s^{-1}). The wind speed affects the magnitude of the vertical motion, but not the location of where the vertical motion occurs because the location depends on how the terrain gradient is oriented to the wind.

Although the pattern of vertical motion does not change along the mountains, the area of intense vertical motion does. The small cirque just to the south of the one labeled with the high wind speed is facing to the northeast. The light horizontal winds produce a small area of vertical motion in the range of 5 m s^{-1} (Fig 10a). When the horizontal wind speed is 10 m s^{-1}, the area of vertical motion above 5 m s^{-1} encompasses more of that same cirque and a small area of vertical motion around 12.5 m s^{-1} is observed (Fig 10b). As the horizontal wind is increased to 15 m s^{-1}, the entire cirque is producing vertical motion that is at least 5 m s^{-1} and a larger area of at least 12.5 m s^{-1} compared to the 10 m s^{-1} horizontal wind (Fig 10c). With winds of 20 m s^{-1}, the area around the vertex of the cirque is producing vertical velocities above 15 m s^{-1} with a maximum above 25 m s^{-1} (Fig 10d). The same type of behavior is exhibited in all of the cirques along the entire windward side of the Ko‘olau Mountains. As the horizontal wind increases, the area of enhanced vertical motion also increases.

B. Vertical Wind Observations (HOP2)

On 20 October 2015 around 1500 HST at the Pali Lookout, the one-minute average vertical wind was stronger than the horizontal wind for nine of the ten observation pairs (Fig 11a). The maximum vertical wind speed measured was 14.9 m s^{-1}, and the maximum horizontal speed was 11.6 m s^{-1}. On 24 October 2015, the one-minute averaged vertical wind was again stronger than the horizontal wind for nine of the ten observation pairs (Fig 11b). The vertical wind at the Pali is consistently stronger than the horizontal wind, because the steep slope of the terrain is tilted more vertically than horizontally. This can be understood through vector addition. If the total three dimensional wind speed following the terrain surface is 14.14 m s^{-1} and the mountain is on a 45° angle, the horizontal and vertical components will both be 10 m s^{-1}. If the total wind speed is 10 m s^{-1} and the slope of the mountain is 60°, then the horizontal component of the wind is 5 m s^{-1} and the vertical is 8.66 m s^{-1}. When the slope of the terrain in greater than 45°, the magnitude of the vertical component of the wind will be higher than the horizontal.

At other locations, the vertical winds are either weaker or comparable to the horizontal wind. At the Diamond Head site, the five-minute averaged vertical wind was 5.1 m s^{-1} and the max speed during that time period was 8.4 m s^{-1}. In the five minutes following that, the average horizontal wind was 6.0 m s^{-1} with a max speed of 10.5 m s^{-1}. The two-minute averaged winds at the Makapu‘u site alternate back and forth between the vertical and horizontal winds being higher (Fig 12a). While the wind was being measured at this site, water droplets were observed, but no precipitating clouds were in the area. Ocean waves breaking on the bottom of the cliff were creating a large amount of spray, and the vertical wind was strong enough to lift the water droplets of size 0.12-0.14 cm (Gunn and Kizner 1949) up the side of the mountain.

At the Koko-Head site, the horizontal wind, which gusted up over 17 m s^{-1}, was consistently stronger than the vertical wind (Fig 12b). Lower along the path where the wind was weaker, the horizontal wind was still stronger than the vertical wind (not shown). In these three locations, the slope of the orography is not as steep as it is at the Pali Lookout, but the observed vertical wind speed is still in the same order of magnitude as the horizontal wind speed.

The HOP model using horizontal winds from the operational WRF model produces vertical wind speeds that are of the same order of magnitude as the observed vertical wind speeds (Table 2). On 24 October, the HOP model produced vertical wind speeds that were higher than the observed values at the Pali Lookout. Three days later, the modeled vertical wind speeds were lower than the observations. On 27 October, the modeled and observed wind speeds have a linear relationship from the hours of 1000 HST to 1400 HST, but the modeled winds are only about 45% as strong as the observed vertical speeds (Fig 13). The average percent difference between the modeled and observed values was only 10%, but the standard deviation was 25% indicating a large spread. On average, the model is representing the vertical wind speeds, but the run-to-run variability is very high.

The HOP model input influences the performance of the prediction of w. On 05 November, the model input horizontal wind speed was 7.4 m s^{-1} at the Pali Lookout, but the actual wind speed was measured at 4.1 m s^{-1}. In this case, the predicted vertical wind speed was greater than the actual vertical wind speed. The model represents an instantaneous state of the atmosphere, but the observations are averages over a few minutes. Scaling the vertical motion by dividing the actual average wind speed of 4.1 m s^{-1} by the model input wind speed of 7.4 m s^{-1} and multiplying by the modeled vertical wind speed of 13.0 m s^{-1}, the new, scaled vertical wind

speed would be 7.2 m s^{-1}, much closer to the 8.5 m s^{-1} observed. At the Diamond Head peak, the modeled horizontal wind speed was 11.3 m s^{-1}, but the observed speed was 6.0 m s^{-1}, leading to a new vertical motion of 4.2 m s^{-1}, again closer to the actual vertical speed of 5.1 m s^{-1}. The modeled vertical motion would perform better with more accurate horizontal wind input. The model is not expected to exactly match the observations because the model points are not exactly the same as the locations sampled. The observation and model pairings show that the HOP model does produce realistic values for vertical velocity near the surface because the values are on the same order of magnitude.

C. Real-time HOP Model Runs (HOP3)

The high-resolution HOP model produces output by solving equations 4 for the vertical motion (w_{oro}), equation 14 for the orographic enhancement to precipitation (p_{oro}), equation 15 for the total precipitation (precip), and equation 17 for the orographic rainfall index (ORI). The model was run every 12 hours and produced hourly output using real-time WRF operational output for variables such as temperature, moisture, and winds during the month of February 2015.

Comparing the ORI (Fig 14a) and w_{oro} (Fig 14b) to the reflectivity shows that there is generally a correlation between these output variables and actual radar reflectivity. In general, the very small values of $w_{oro} < 1$ m s^{-1} (and low ORI) correspond with values of radar reflectivity below 15 dBZ, which would be a rain rate of 0.18 mm h^{-1} using the operational WSR-88D Z-R relationship used in Hawai‘i (Birchard 1999). When $w_{oro} > 20$ m s^{-1} (ORI > 600 mm m s^{-1}), 89% of the reflectivity values in the same box from Fig 5 are between 20 – 45 dBZ (0.47 – 54 mm h^{-1}), a sign that light to heavy precipitation is occurring.

When the box-maxima are averaged together for a single hour (30 minutes on either side of the top of the hour) as in Fig 15 the correlation is even stronger with $R^2 = 0.54$ for w_{oro} and $R^2 = 0.47$ for ORI. The ORI and w_{oro} are closely related again, implying that the w_{oro} is the important term in the ORI equation and not the TPW. The mesoscale variation of the vertical motion generated by the horizontal winds interacting with the mountains is the primary driving factor in determining where precipitation is happening and is more important than the spatial distribution of the moisture.

When the averaged $w_{oro} < 4$ m s^{-1}, the reflectivities are generally below 15 dBZ. When the averaged $w_{oro} > 15$ m s^{-1}, 83% of the reflectivities are above 20 dBZ. These thresholds provide guidance about whether or not rain is occurring over a certain location in the first set of thresholds, and whether rain is occurring over the Koʻolau Mountains in general for the second set. The lower threshold implies that when the winds are weak, there is not enough lift generated by the orographic vertical motion to promote precipitation in clouds. On the other hand when the horizontal winds are strong and the orographic vertical motion is large, there is a large enough moisture flux to enhance clouds that will rain. Vertical motions of at least 15 m s^{-1} are large enough to almost always produce precipitation enhancement over the Koʻolau Mountains.

The precipitation part of the HOP model did not produce promising results. Some of the p_{oro} values were above 50 mm of rain in an hour, which was very unrealistic compared to the observations. To attempt to filter out some of the unrealistic results, the p_{oro} and total precipitation fields were arbitrarily capped at 1.27 mm (0.05 inches) and 2.54 mm (0.1 inches) respectively. By looking at only the small values of precipitation, a slight correlation was observed (Fig 16a). When the reflectivity is greater than 20 dBZ, the p_{oro} value was always at least 0.01 inches. The precipitation from the HOP model shows a similar threshold of 0.01

inches required for the reflectivity to be at least 20 dBZ (Fig 16b). This method for calculating precipitation is not effective because the HOP model is too simplified with respect to microphysics, uses too many assumptions, and relies on WRF data that is not on the same grid spacing as HOP. Using a Fourier transform (Smith and Barstad 2005) is a much better method for finding orographic precipitation.

Using the relationship between w_{oro} and radar reflectivity (Fig 15b), the orographic rainfall pattern can be calculated using the Tropical Z-R relationship (Fig 17). The cumulative precipitation that is greater than 5 mm occurs mostly around and above the 400 m terrain height contour. This is where the terrain gradient is the strongest. The larger cirques have longer areas of precipitation, as well as having the highest precipitation values. The very long easterly-facing cirque that extends from about 21.32 N to 21.36 N has the longest continuous area of precipitation, including several locations where the total is above 25 mm. To the north near 21.45 N, the cirques also have high total precipitation values, but the pattern is discontinuous because the cirques are much smaller. The highest precipitation values occur within the cirques where the gradient of the terrain is the steepest.

Along the westerly-facing side of the Ko‘olaus, atypical wind from southwesterly direction creates the situation where the precipitation is comparable to the east facing side. The large valley near 21.34 N and 157.8 W has a concave shape open to southwesterly winds, and displays the longest continuous pattern of precipitation. This area also contains relatively high precipitation totals.

CASE STUDIES

Three case studies using the HOP model have been conducted for different weather events over the Koʻolau Mountains. The first case study is for a 24-hour period starting at 00 UTC on 09 March 2012 (Table 1 HOP4). During this time, heavy precipitation occurred along the Koʻolau Mountains, and a super cell formed along the windward side that eventually traveled over Kaneohe and caused a tornado in Lanikai. The HOP model is run using the 3-km WRF hourly output from the 00 UTC model run. The ORI and w_{oro} from the high resolution HOP model are compared to the 15-minute averaged radar reflectivity from the PHMO radar. The maxima of w_{oro}, ORI, and reflectivity are averaged in the same way as the operational runs from the previous section. The HOP model is also run using the GFS 850 hPa winds for comparison to the lowest sigma level WRF wind HOP run to contrast with the National Weather Service's operational ORI.

The second case study is for one-hour starting at 2100 UTC on 03 November 2013. The HOP model is run using winds from a radiosonde launched at 2140 UTC, and the winds are extrapolated across the entire grid with the height of the mountain at a given location matching with the wind from the radiosonde at the same height (Table 1 HOP5). A second HOP model run is done using the WRF model output for 2200 UTC (Table 1 HOP6). The LCL is also calculated from the sounding using equation (13). The model output is compared to radar output taken during the Hawaiian Educational Radar Experience (HERO) using a Doppler on Wheels (DOW) located near the mouth of the Waiheʻe Stream in Kahaluʻu. The radar data are filtered so that the normalized coherent power is greater than 0.2, the Correlation Coefficient (ρ_{HV}) is greater than 0.9, and the velocity is greater than 0.5 m s^{-1}. The radar data are averaged over one

hour starting at 2100 UTC. The maxima of vertical motion are compared to the maxima in downstream reflectivity.

The final case study is for 24-hours starting at 0100 UTC on 24 August 2015 (Table 1 HOP7). During this time, a mesoscale convective complex moved over the Island of Oahu, but the winds were light. A plan position indicator (PPI) view of the radar showed that the entire island was covered by precipitation, and wide spread flooding occurred. The HOP model was initialized with the WRF model run output from the 12 UTC 23 August run. The model output is compared to the 15-minute averaged radar reflectivity, similar to the first case study.

A. Heavy Rain Along the Ko‘olaus: 09 March 2012 (HOP4)

For the 24 hour run between 0000 and 2300 UTC on 09 March 2012, the HOP model run with WRF operational output shows significant promise in providing guidance to when and where the most potential for extreme rain and storm development will occur along the Ko‘olau Mountains. Because the HOP model ORI and w_{oro} show best correlation actual precipitation, the focus will be on using ORI and w_{oro}. The radar reflectivity correlations with ORI ($R^2_{ORI} = 0.61$) and vertical motion ($R^2_{Woro}=0.60$) are better (Fig 18) than the month of February 2015. The w_{oro} > 15 m s^{-1} threshold for precipitation holds true for this case, with the lowest reflectivity being 32.3 dBZ when w_{oro} = 15.7 m s^{-1}. During the 24 period, there are no instances when w_{oro} < 4 m s^{-1} and precipitation is occurring in every diagnostic run of the HOP model.

The vertical motion maxima in the HOP model from the boxes in Fig 5 can be compared to the 15-minute averaged reflectivity from the PHMO radar. The precipitation occurring on 09 March 2012 stays focused over the Ko‘olau Mountains from 0600 UTC to 1800 UTC, with the exception being the formation of a super cell between 1500 and 1600 UTC. During this period,

the Froude number remains above one (Table 3) indicating that the kinetic energy of the incoming flow is strong enough to climb over the mountain and blocking does not play a significant role in producing orographic precipitation. At 0600 UTC (Fig 19), the highest values of vertical motion calculated from the HOP model do not match up with the highest values of reflectivity in the boxes. This is likely due to the incoming moisture not matching up with the location of the highest vertical motion. The second and third highest values of w_{oro} (14.0 m s^{-1} and 14.2 m s^{-1}) are observed with very light showers in the vicinity. The next two highest are found just to the north, but the precipitation is very light in this area as well. The area where the reflectivity is the highest is the area where the vertical motion maxima are the smallest. The lowest maximum value w_{oro} = 6.9 m s^{-1} is actually closest to the reflectivity maximum. The incoming showers were more to the north, which is why there is more precipitation in that area. The vertical motion calculation does not account for the moisture, so the HOP model must be considered with the actual moisture field in mind.

A loop of reflectivity during this time shows that the moisture is moving towards the north and west with southeasterly cloud-layer winds pushing all of the lifted moisture in that direction. The southern extent of the precipitation stays very close to 157.90W, 21.45N, the area where the w_{oro} maxima are 13.6 m s^{-1} and 12.0 m s^{-1}. Although the reflectivity and vertical motion maxima are not collocated at this time, it is possible that the upward motion feeding the precipitation is to the south of where the precipitation occurred. This would agree with precipitation falling downwind, as observed by Schroeder (1977).

At 1500 UTC, the rainfall is still falling over the Koʻolau Mountains. There is still strong vertical motion on the southeastern part of the island in Fig 20, but that area remains dry. There is typically relatively strong vertical motion on the slope of the mountains in this location

because the slope of the mountain is steep, but it is often dry because the mountains in this area are not tall enough to push air to the LCL. To the north of that, the strongest vertical motion for the entire 24 hour period is w_{oro} = 26.2 m s^{-1}. The two maximum vertical velocities to the north of that are w_{oro} = 24.4 m s^{-1} and w_{oro} = 23.5 m s^{-1}. These three points, which show the strongest vertical motion over the island, are collocated with the highest radar reflectivities. The greatest precipitation discerned by the radar extends downwind, aligned with the average in-cloud wind direction depicted by the wind barbs (Fig 20), which are calculated by taking the average of the winds in the layer from the LCL equation (13) to the top of the cloud (Z_{top}).

The ORI and w_{oro} are very closely related (Fig 21a). The correlation of the ORI and w_{oro} is R^2 = 0.92 whereas the correlation between the ORI and TPW is only R^2 = 0.03 (Fig 21b). The ORI output from the HOP model is expected to closely resemble the w_{oro} output because they have the same main term and the moisture does not vary much over such a small area. In a mesoscale domain in the presence of mountains, the difference in the orographic vertical motion is more important than the changes in atmospheric moisture in determining where precipitation will occur.

The HOP model was run using winds from the 850-hPa level of the GFS model and compared to the HOP model using the lowest level WRF winds. The GFS winds were temporally spaced at 3-hour increments, so the WRF winds at the corresponding times were used. The GFS ORI does not correlate with radar reflectivies as well as the WRF ORI. The maxima from the boxes in Fig 5 are averaged for a given time and compared with the 15 minute averaged reflectivity (Fig 22). The vertical motion calculated using the WRF winds has a coefficient of determination R^2 = 0.43 compared to R^2 = 0.33 for the GFS using corresponding times. Over the entire 24 hour period, the ORI calculated using the WRF winds the R^2 = 0.60

(Fig 18b). The increase in temporal resolution of the WRF model leads to better correlation between the WRF HOP and radar reflectivity.

The two different model winds produce vertical motion that is not in a one-to-one relationship (slope of the best-fit line of 0.61) and is also not well correlated ($R^2 = 0.28$) (Fig 23). Using the GFS winds, the vertical motion is higher for 6 of the 8 output times, and the GFS HOP is higher than the WRF HOP by at least 20%, 4 of the 8 times. The two different runs agree at one point, which happens to occur at 1500 UTC (Fig 20 WRF, Fig 24 GFS), both having $w_{oro} = 18.5$ m s^{-1}. In the WRF HOP run, this is the maximum and matches up with the maximum in reflectivity in Fig 20. In the GFS HOP run, the vertical motion maximum occurs when $w_{oro} = 21.9$ m s^{-1} and the reflectivity is the third highest (Fig 22). For this case, using the WRF winds with the HOP model to find ORI is an improvement over the operational GFS winds used by the National Weather Service.

B. Light Trade Wind Shower Enhancement: 03 November 2013 (HOP5 and HOP6)

During the HERO project, the Doppler On Wheels radar system was deployed to the Kahaluʻu site on 03 November 2013. Rain showers occurred over the Koʻolau Mountains between 2100 and 2200 UTC, and full volume scans were used to create the composite reflectivity images (Fig 25). Weak echoes are observed at the beginning of the hour, with maximum values between 10 and 15 dBZ. A collection of hydrometeors causing an area of weak radar reflectivity began to move onshore, and as it encountered the mountains at 2138 UTC (Fig 26), light to moderate showers developed over the terrain. Over the next half hour, the showers dissipated.

There are six mountain-enhanced rain "cells" observed (Fig 26); using the term cell to mean an area of reflectivity with a maximum reflectivity of at least 10 dBZ that is surrounded by an area of 0 dBZ or lower. The second most northerly cell had the strongest radar returns with a maximum of 33.1 dBZ. The next strongest were the two south cells at 25.3 and 22.4 dBZ. To the west of the cell with 25.3 dBZ, another cell formed with a reflectivity maximum of 14.8 dBZ.

A radiosonde was launched at the DOW site at 2140 UTC, which happened to coincide with the time that the showers developed over the mountains (Table 1 HOP5). The Froude number calculated from equation (5) using the temperature variables from the sounding and the lowest level wind is 1.15. For each point on the terrain, the wind at the terrain height in the sounding was used to run the HOP model to calculate w_{oro}. The HOP model results are overlaid on the radar reflectivity (Fig 27) showing the areas with the strongest upward motion. The wind remained northeasterly from the surface through the cloud layer (Fig 28). Each storm cell occurs downwind of a corresponding maximum in w_{oro} except for the 25.3 dBZ echo. By subjectively matching the w_{oro} maxima with their corresponding down wind reflectivity maxima by eye (Fig 29), the HOP model shows a remarkable correlation of $R^2 = 0.93$.

The operational HOP model forced using the lowest sigma level WRF winds (Table 1 HOP6) produced a similar pattern of vertical motion maximums, but the range of values for vertical motion was lower (Fig 30). Nevertheless, the HOP model output for 2200 UTC maxima compared to the reflectivity had a correlation of $R^2 = 0.94$. The brevity of the precipitation did not allow for rain to fall downstream from the mountain for very long. In this case, the precipitation is short lived and all falls out quickly, and the HOP model performs at its best.

Using the average reflectivities from 2100 UTC – 2200 UTC, a correlation between the reflectivities and vertical motion is $R^2 = 0.68$ (Fig 31). There appears to be an outlier with the

20.5 m s^{-1} data point. The largest area of precipitation occurs downwind from this location (Fig 27), so when the moisture was lifted to the trade wind inversion, it may have become more spread out instead of focused over a smaller location. When averaged over time, the reflectivity is lower than expected compared to a location where radar echoes occurred for more than one volume scan. For the rest of the cirques, the vertical motion and average reflectivity match up well. If the outlier data point is removed, then $R^2 = 0.94$ (not shown).

C. Mesoscale Convective Complex: 24 August 2015 (HOP7)

This case study is presented as an example of a synoptic-scale forcing with light winds in which the HOP model is not applicable. As tropical storm Kilo moved past the Hawaiian Islands, an area of tropical moisture turned into a mesoscale convective complex (MCS) and strengthened over Oahu on 24 August 2015. The precipitation from the MCS covered the entire Island of Oahu (Fig 32), and the convective areas caused intense and widespread rainfall leading to flash floods. Over 3.5 inches of rain was observed at the Honolulu International Airport. The winds were mostly light, and varied between upslope and downslope along the Ko‘olaus with Froude numbers well below 1.

The linear upslope nature of the HOP model does not produce a meaningful correlation between vertical motion and precipitation during a weak wind synoptic event. The averaged vertical motion maxima do not match well with the averaged reflectivity maxima. The best-fit line has a negative slope indicating that higher values of w_{oro} actually match up with lower values of reflectivity. The high w_{oro} values are along the Ko‘olau Mountains near the peaks at 1500 and 1600 UTC in Fig 32, but the higher reflectivities display broad areas of elevated reflectivity that are not tied to the terrain. To the west of Kaneohe is a w_{oro} maximum of 5.1 m s^{-1}

and the most northern w_{oro} maximum is 3.1 m s^{-1} (Fig 32a). The reflectivity associated with the higher vertical motion is much lower than the reflectivity associated with the weaker vertical motion.

The average of the maximum values of w_{oro} at 1500 UTC is 4.2 m s^{-1} (Fig 32a), and at 1600 UTC in is 6.3 m s^{-1} (Fig 32b). Every box that maxima were found in had an increase from 1500 UTC to 1600 UTC, yet the reflectivity decreased over the Ko‘olaus and over the entire island in general. The correlation between the HOP model vertical motion and reflectivity is negative with $R^2 = 0.029$ (Fig 33). The influence of vertical motion generated by the horizontal wind interacting with the orography is not the driving force of this synoptic event, so the HOP model is unable to simulate any of the precipitation enhancements due to the topography. In this case, the synoptic scale dynamics are more important than mesoscale influence of the mountains.

WRF Model Terrain Gradient Modification

The HOP model has very fine horizontal resolution of the terrain of Oahu; however, the model is simple and does not include all of the complicated processes of the atmosphere. In contrast, the WRF model incorporates a lower-resolution grid. This allows the WRF model to complete calculations of the computationally expensive processes of the atmosphere, which are not included in the HOP model, in a reasonable time frame. In the preprocessing stage of a WRF run the high-resolution terrain is smoothed to fit the WRF model grid spacing. When the model calculates vertical motion, the detail of the terrain gradient is lost because of the smoothing of the terrain. To recapture the terrain detail, a new method of calculating the vertical motion in the lowest level of the WRF model has been developed using the terrain gradient derived in the HOP model. This new method provides the WRF model with a better representation of the vertical motion at the lowest level of the model, which leads to an improvement in the skill of precipitation prediction.

A. Model Set Up and Validation

The WRF model is set up to run with a single domain of 3 km grid spacing for 24 hours starting at 0000 UTC 09 March 2012 using National Center for Environmental Prediction (NCEP) FNL (final) data obtained from the National Center of Atmospheric Research's Research Data Archive website. The model grid is 220 points in the east-west direction and 170 points in the north-south direction, and 40 vertical layers encompassing all of the Hawaiian Islands. The vertical coordinates are terrain following with the lowest vertical level at approximately 17 m above the ground. The grid mimics the second nested grid of the operational WRF model run at the Mauna Kea Weather Center and is described in the Data and

Methods section. Model output is produced every 15 minutes for high temporal resolution. Two model runs were performed; the first was run normally (CTRL) and the second was run employing the hires_w_surface subroutine (EXP).

To verify that the terrain gradient and vertical motion calculation of the HOP model is similar to the WRF model, the HOP model is run in dry mode with the same terrain and lowest level horizontal winds as the 3 km WRF model. The vertical motion from the HOP model is then compared to the WRF model over the Island of Oahu. Additionally, a comparison of a location along the windward side of Oahu on the upward slope of the Koʻolau Mountains (21.437 N, 157.859 W) is used to compare the values of vertical motion from both models for a 60-hour period starting at 0 UTC 01 November 2014.

Rain gauge data are used to compare the WRF models to observations during the month of January 2016. The total daily rainfall from 0800 HST is used for both the observations and model as the daily total. The model totals are taken at the closest latitude and longitude to each of the 56 rainfall observation locations (Fig 4). The data are added together for the entire month for comparison.

Level II radar data from the NEXRAD Weather Surveillance Radar 88 Doppler Molokaʻi (PHMO) site are used to assess the precipitation pattern during the period from 0003 UTC to 1801 UTC on 09 March 2012. The radar data were switched to a gridded netCDF format on an 800 x 632 point grid with resolution of 0.00428°. Only the 0.5° elevation angle data were used for the analysis.

B. WRF Model and Linear Model Comparison

During the 60-hour comparison between the HOP and WRF models over windward Oahu on 01 November 2014, the vertical motion from the two models are nearly identical and very well correlated (Fig 34). The best line fit has a slope of 0.91, indicating that the WRF model vertical motion is slightly larger than the HOP model during the 60-hour period. The differences in the vertical motions are most likely due to the WRF model and HOP model not using the exact same code, different compiler options, and different precision in their calculations. The strong correlation of $R^2 = 0.96$ indicates that for this time period, the two models are generating the same trend in vertical motion. At 1500 UTC on 09 March 2012, the vertical motion of the HOP model and WRF model look identical over the Island of Oahu (Fig 35). The strong correlation between the two models is due to the models using the same basic equation to calculate the vertical motion. Additionally, the two models are using the same input winds.

C. Effects of Using the Enhanced Terrain Gradient

1) Gradient Differences

The terrain gradient for the old method (Fig 36a) is an order of magnitude lower than the gradient produced by the new EXP WRF (Fig 36b). To the west of the Kaneohe Peninsula, both models have a local maximum (orange in Fig 36b and green in Fig 37) but the gradient in EXP is about 0.045, and in CTRL is about 0.007. In this case the two models agree on the location of the strongest terrain incline, but the magnitude of the gradient of the EXP model is approximately 6.5 times higher than the CTRL. To the north and slightly west, there are two points with the same color on both images (yellow in Fig 36b and orange in Fig 37). The location is again the same, but the values are about 3.5 times different.

There are several sections where the EXP model is producing a different shape of the terrain as well. Over the Kaneohe Peninsula on the eastern part of the island, the EXP terrain includes some of the small hills, whereas the CTRL model sees this region as flat. On the southeast corner of the island, the EXP model shows strongest variation in terrain, over 0.12 m/m, but the CTRL model has this region as flat. The cliffs along the ocean on the eastern side of Oahu are very steep (Fig 1), so the EXP model is clearly showing an improvement over the CTRL model.

The terrain gradient over the western side of the island also shows a more realistic gradient in the EXP model. The northwest section of Oahu is mostly flat along the coast with high mountains just inland. This is well represented in the EXP model along the northern and western sections along the coast going out to Kaena Point (the northwest corner of Oahu). In the CTRL model, these mountain gradients are more scattered and not nearly as strong.

2) January 2016 Comparisons

Rain gauge data are compared to model data during the month of January 2016 (Table 4). Throughout the entire month, the rain gauges recorded 1219.4 mm of rain. The EXP model produced more overall precipitation at the rain gauge locations (709.4 mm) compared to the CTRL model runs (668 mm). Although this is only a 6% increase, it turns out to be about 1.4 mm (0.05 inches) per day. The percent error in comparing EXP and CTRL to the observations is 41.8% and 45.2% respectively. The EXP model produces more precipitation and is closer to the observations that the CTRL model during the month of January.

The EXP model does a slightly better job than CTRL during the month of January when precipitation actually occurs. In considering only when rainfall was observed, the EXP model's

percent error is 22.7%, but the CTRL model is 23.2%. This small improvement is due to the EXP model usually producing more precipitation.

A box that contains the rain gauges with the bounds being between 21.325°N – 21.400°N and 157.75°W – 157.85°W was analyzed to consider rainfall only in the region of the Koʻolau Mountain slope. There was 434 mm of rain observed at these stations during the month of January. The CTRL model produced 202 mm of precipitation, whereas the EXP model predicted 191 mm. There were many times that precipitation was predicted but did not occur. Considering only when precipitation occurred, the CTRL and EXP models both over predicted the amount of precipitation. The CTRL model had an average of 311% error for rainfall predicted during an observed rainfall event. The EXP model did better with an average of 279% error for the same period.

The rain gauge at 21.33°N, 157.80°W is along the slope of the mountain. The EXP model produced more precipitation than CTRL at this location (Table 5). On January 6, the EXP model predicted 1.7 mm, but the CTRL model predicted 1.4 mm. The actual precipitation was 37.8 mm. Both models missed the big precipitation event at the rain gauge, but the EXP model is clearly showing more precipitation, especially in the area of the Koʻolau Mountains (Fig 38). When precipitation is occurring over the Koʻolau Mountains, the EXP model produces higher precipitation in that area. The increased terrain gradient causes an increase in the lowest level vertical motion, which leads to an increase in the enhancement of orographic precipitation.

3) Case Study of 09 March 2012

On 09 March 2012, strong wind shear and very large buoyancy associated with a vigorous short wave trough aloft caused a super cell to form over Kaneohe. The EXP and

CTRL model runs produced different vertical motion patterns. The upward motion is stronger along most of the Ko‘olau Mountains’ windward side in the EXP run (Fig 39). This is a result of the increased gradient along the slope of the mountain. On the northern part of the island, a difference in the range of 0.7 m s^{-1} occurs. In reality, there is a small mountain in that area over 500 m high (Fig 1), but that feature is absent in the 3 km terrain. Along the southeast coast, there is a difference of 0.8 m s^{-1} associated with a small cliff right near the coast that is also absent in the low-resolution WRF terrain. Each point along the mountain slope where the vertical motion is larger in the EXP run (Fig 39) is associated with either a small cirque or a very sharp terrain gradient in the high-resolution terrain (Fig 1).

The change in vertical motion caused changes in the modeled precipitation patterns. The EXP model produced precipitation that was mainly focused over the Ko‘olau Mountains, with a distinct northern and southern maximum (Fig 40a). There was also some precipitation right off the southeast coast. In the CTRL run (Fig 40b), a large area of precipitation occurred along the northeastern part of the island that extended well off to the northeast. The modeled precipitation swath is much larger and the rainfall totals are much higher, especially over the northern part of the island and ocean. There was some precipitation that fell over the southeastern part of the island, but the main focus of the event occurred to the north. The positive difference between subtracting Fig 40a and Fig 40b shows that the EXP model run puts more precipitation over the mountains in the southeastern part of the island as well as just to the south of the northern peak of the Ko‘olaus (Fig 41). The EXP created an increase in vertical motion over the windward slope of the mountains leading the model to produce precipitation that is more focused over the mountains. Heavy precipitation events often occur in conjunction with terrain anchoring

(Schroeder 1977). The precipitation is more anchored to the mountains in the EXP run because of the increase in vertical motion along the slope.

The PHMO radar made observations every 4 minutes and 40 seconds (+- 1 second) at the 0.5° elevation angle. Between 0003 UTC and 1801 UTC, there were 232 observations. During that time period, radar reflectivity returns were observed over the Koʻolau Mountains for almost the entire time period (Fig 42), with most of the reflectivities occurring near the northern peak, to the west and southwest of Kaneohe, and within the southeastern valleys of the island. The storm is anchored to the terrain consistent with the EXP model run. These areas of high hydrometeor concentration from the radar coincide with the areas of rainfall forecast by the EXP model better than the CTRL model (Fig 40). The area to the west and southwest of Kaneohe shows up in both the high activity region (Fig 42) and the EXP model (Fig 41).

Qualitatively, the average reflectivity pattern (Fig 43) matches well with the precipitation pattern produced by the EXP model (Fig 40a), with most of the rainfall occurring along the mountains and then extending to the northwest over the ocean. The average reflectivity pattern does not show a large preference for development on the northern Koʻolaus. Heavy precipitation occurs to the north and northeast of the island as shown by the CTRL run (Fig 40b). Neither model was able to produce the super cell that moved over the Kaneohe Peninsula. The average reflectivity pattern matches much more closely with the precipitation produced by the EXP run. By using a more realistic pattern of terrain gradient in the WRF model, the upward motion along the windward side of the Koʻolau Mountains is increased, and the precipitation forecast is improved, matching much more closely to the radar reflectivity pattern. An operational forecaster looking at these model runs would produce a better forecast by following the EXP run over the CTRL run.

D. Nonprobabalistic Forecasts of Rainfall

The 15-minute WRF model precipitation output is compared to the radar reflectivity in order to examine how well the model performs using the 2x2 contingency table method from Wilks (2006, Chapter 7). The nonprobabalistic discrete variable measured is the occurrence of rainfall at a given location. The observed values of rainfall come from the PHMO radar using a 30-minute average of the data for every 15 minutes of time starting from 0000 UTC to 1730 UTC on 09 March 2012. For example, the average reflectivity at a given point at 0300 UTC would be the average of radar reflectivity from 0245 UTC to 0315 UTC. In order for a the model forecast to be considered a hit, a radar reflectivity of at least 15 dBZ must occur in a grid box that precipitation is forecast to fall, or an adjacent grid box to the predicted precipitation point in any horizontal direction. By using this method along with the 30-minute reflectivity average, some spatial and temporal leeway is given to the model. False alarms occur when the model predicts precipitation, but the radar reflectivities in the predicted grid box and adjacent points are all less than 15 dBZ. Misses occur when there is precipitation in a grid box, but the model forecasts none. Correct rejections happen when the model correctly predicts no precipitation in a grid box. The EXP model has fewer hits, more misses, less false alarms, and more correct rejections than the CTRL model (Table 6). The proportion of correct forecasts for the EXP model (0.94) is slightly better than for the CTRL model (0.93). The CTRL model is overall wetter, and has almost exactly double the number of false alarms as the EXP model. The false alarm ratio is 0.06 for EXP compared to 0.11 for EXP, meaning 11% of the forecasted precipitation occurring in the CTRL model did not occur, leading to an increase in threat score from 0.79 for the EXP run compared to 0.76 for the CTRL run. The number of bad forecasts (false alarms and misses)

in the EXP model (3310) compared to the CTRL model (3842) leading to the probability of a correct rejection to be 0.56 for EXP but 0.54 for CTRL. The CTRL model is has a higher probability of a hit (0.069) compared to EXP (0.061), but the probabilities are very close to each other. The Gilbert Skill Score for EXP is higher at 0.725 and for CTRL is 0.698. The models are producing statistically similar results because most of the dynamics and physics are identical, but the increase in model skill can only be attributed to the improved methodology of calculating the lowest level vertical motion.

The EXP and CTRL runs have similar patterns where they had the most hits (Fig 44a and b), which lines up with where precipitation occurred. The increased misses that the EXP model experienced (Fig 44c) happened in the northern part of the domain over the ocean, especially to the northwest. The increase in low-level vertical motion may have caused more precipitation to occur over the mountains and prevented the advection of some of the heavier precipitation over the ocean away from the orography (Fig 40). The higher vertical motion is causing more anchoring to the mountains in EXP. The CTRL model had more misses off the eastern coast of Oahu (Fig 44d), especially to the east of Kaneohe.

There is a large reduction in false alarms for EXP (Fig 44e) compared to CTRL (Fig 44f). The model over predicts precipitation over the ocean, especially to the northeast of the island (Fig 40b), which is the cause of most of the false alarms. There are also more false alarms over the ocean just to the north and east of the Kaneohe Peninsula. Because the CTRL model does not focus the precipitation more along the mountain similar to what happened in reality, the model produces an abundance of false alarms that do not occur in the EXP model. Both models have a similar false alarm pattern over southern central Oahu where the terrain influence is less important because the orography is lower. The pattern for correct rejections is very similar in

both models, with the EXP model (Fig 44g) having a few more correctly forecasted dry areas on the southern part of the Koʻolau Mountains than the CTRL model (Fig 44h).

The number of correct forecasts (hits and correct rejections) is higher in the EXP model (52490) than the CTRL model (51227), but this is especially true over the ocean to the east of the state. The EXP model (Fig 45a) and CTRL model (Fig 45b) have large differences in accuracy counts over the ocean. To the northeast of the domain and to the north and east of the Kaneohe Peninsula, the EXP model is clearly outperforming the CTRL model. The CTRL model over predicts precipitation in that area (Fig 40b). Over the Koʻolau Mountains, the two models have very similar counts of accurate forecasts, but the EXP model does produce higher hit counts on the southeastern part of the island. This is where the EXP model produces more precipitation than the CTRL model (Fig 41). The enhanced lowest level vertical motion calculation is providing for a more accurate depiction of precipitation occurrence than the normal calculation done by the WRF model because the terrain-induced vertical motion is closer to reality in the EXP model.

The false alarms over the ocean discussed above account for most of the difference between the EXP and CTRL models. Most of the bad forecasts that occur in the EXP model (Fig 45c) occur in the northwestern part of the domain and over south and central Oahu. The CTRL model's bad forecasts (Fig 45d) occur over south and central Oahu and over the ocean to the east and northeast of the island. The CTRL model shows a large increase in false alarms due to the precipitation not being focused over the mountains, which leads to the EXP model outperforming the CTRL model. The more accurate depiction of the Koʻolau Mountain's gradient in the EXP model run provides an increase in accuracy and a decrease in the false alarm rate of the model.

Scaling the high-resolution terrain gradient to calculate the model's lowest level vertical motion improves the skill and accuracy of the model as well as greatly reducing the false alarm ratio.

Discussion and Conclusion

A. HOP Experiments

A 51.7 m x 55.6 m grid spaced linear orographic model that diagnoses the vertical motion over the Island of Oahu was created and shows that vertical velocities in excess of 10 m s^{-1} are possible over the Koʻolau Mountains (Fig 7). Vertical motion of this order of magnitude is not often thought to occur except in the case of severe thunderstorms, but observations (Table 2) show that these vertical motions do occur under trade wind conditions. The location and speed of vertical motion change as the wind direction changes (Fig 6), similar to the findings of Watson and Lane (2012). Vigorous downward motion on the leeward side of the mountains can lead to downslope windstorms. On the windward side, the steep topography of the Koʻolau Mountains cause the horizontal winds over the flat ocean to turn in the vertical direction, which enhances precipitation.

The strong upward motion induced by the terrain leads to an enhancement of precipitation along the Koʻolau Mountains. The correlations between the precipitation and vertical motion during the HOP experiments provide evidence that when the orographic vertical motion is high, more precipitation will occur near the area of enhanced vertical motion. The air off shore has an abundance of moisture, and when the orographic vertical motion lofts that moisture, cloud water content is increased, which leads to more precipitation. During experiments HOP4 and HOP5, the coefficient of determination for the correlation of vertical motion to precipitation were $R^2 = 0.60$ and $R^2 = 0.93$. Because the HOP model does not include blocking, these high correlations show that blocking is not significant during these experiments. The linear upslope lift of the moisture during heavy precipitation events with strong winds and

typical trade wind shower events over the mountains is the primary mechanism for orographic precipitation enhancement.

The thresholds from HOP3 give guidance to operational forecasters about the likelihood of precipitation based on the orographic vertical motion. The lower threshold implies that when the incoming horizontal wind is very light, the chance for orographic precipitation enhancement is diminished greatly. Contrastingly, the higher threshold shows that strong incoming horizontal winds lead to a greater chance of precipitation enhancement, similar to Nugent et al. (2014). This makes sense from a linear modeling perspective because stronger horizontal wind speed leads to a higher Froude number, and the linear model works best when the Froude number is above 1 (Hughes et al. 2009). These thresholds also show, in cases where the winds are very strong or calm that the actual microphysics can be left out when trying to predict precipitation because only the mountain geometry, wind speed, and orientation are needed to obtain these numbers.

The ORI and w_{oro} correlations to precipitation are nearly identical for every HOP experiment. When comparing the ORI to w_{oro} and TPW, the ORI was almost exactly correlated to w_{oro} and not correlated to TPW (Fig 21). Clearly, the w_{oro} term is the dominant term when calculating ORI on the small scales of the HOP model. Although moisture content is important to the precipitation process, on the mesoscale in the area of mountains, the orographic vertical motion is more important than the small-scale variations in the total moisture in the atmosphere. When moisture is present, the pattern of orographic vertical motion will determine where the precipitation will fall. This is exemplified by HOP5. This experiment has constant TPW and varies the winds only by height, but the correlation of ORI to precipitation is very strong.

Using a finite difference scheme and simple microphysics did not produce a meaningful precipitation pattern in the HOP model. The attempt at using Hawaiian specific micrometeorology such as the trade wind inversion and relation of the LCL to the mountain height were too simplified and relied too much on deriving variables from a larger scale data set. A spectral method, with a Fourier transform to calculate precipitation like the one used by Smith and Barstad (2004), is likely to produce a much better result than the HOP model finite differencing scheme.

Although the HOP model produces useful forecast guidance most of the time, the limitations of the HOP model are demonstrated during HOP7. When precipitation is due to a large-scale synoptic storm with light winds, the HOP model does not provide meaningful guidance. The HOP model performed poorly in simulating the precipitation associated with an MCS that occurred over Oahu in August 2015. With a low Froude number due to light winds, the winds were unable to traverse Oahu's mountain ridges, and the vertical velocities were not correlated with the precipitation intensity. Blocking, friction, synoptic influences, and water loading are all removed from the HOP model, so it is unable to simulate precipitation when these atmospheric conditions are important to the precipitation process.

B. WRF Orographic Vertical Motion Modification

A new method to compute the lower boundary condition of the WRF model was derived from the terrain gradient in the HOP model. Instead of fitting the high-resolution terrain to the WRF model domain and then calculating the gradient and multiplying it by the horizontal wind, the high-resolution terrain gradient was fit to the WRF model and used to calculate the vertical motion at the lowest model level. By smoothing the terrain gradient instead of the terrain heights for calculating the lowest level vertical motion, the model produces higher values of vertical

motion along the windward face of the mountain (Fig 39). The new method produces more rain in the area of the mountains when orographic precipitation is occurring (Fig 38). This produced a more accurate forecast in the WRF model because of the change in the vertical motion pattern (Table 6). The model skill increased for forecasting the occurrence of precipitation during the severe thunderstorm event on 09 March 2012, because the terrain gradient is a more realistic depiction for the model. During an entire month of forecasts, the model error is slightly reduced by using the new terrain gradient method (Table 4). The old and new methods are very similar because they are using the same physics and dynamics, but only the lowest level vertical motion is changed. This slight change leads to a small but noticeable improvement in the WRF model forecast. Smoothing the terrain gradient instead of the terrain should be applied to the WRF model over the Hawaiian Islands.

Because of the coarse resolution of the enhanced WRF model, WRF is unable to reproduce observed vertical motions in excess of 10 m s^{-1}, and likely is unable to resolve the stronger updrafts present within the super cell storm. Although the enhanced WRF model produces a better overall precipitation forecast, the large computational cost and numerical instability of running a full physics and dynamics model, prevents it from being able to run timely forecasts with the grid resolution of the HOP model. A combination of the HOP and enhanced WRF models may provide forecasters with the best guidance to make accurate forecasts over Oahu.

Future Work

There is more work that can be done with the HOP model. The precipitation calculation may improve if the decay of w was something other than linear. This would give more insight into how vertical velocity actually varies in the cloud. The precipitation calculation could be done with a spectral method using Smith and Barstad's (2004) model for comparison.

More experiments comparing the GFS ORI and the WRF ORI are needed to see which is works better in general. Several more cases are needed to determine how often the WRF ORI would outperform the GFS ORI. Testing the ORI and w_{oro} relationship in a non-island setting where the there is less abundant moisture is also necessary to see how important w_{oro} is to forcing precipitation.

More cases are also needed for the new WRF boundary condition. This new boundary condition calculation could be incorporated into a future release of the WRF code base or any other model. It should be tested with different boundary layer schemes, w-damping, and physics packages. It can also be applied over a larger area than just Oahu, such as the entire Hawaiian Islands or the Continental United Stated.

References

Barstad, I. and F. Schüller, 2011: An Extension of Smith's Linear Theory of Orographic Precipitation: Introduction of Vertical Layers. *J. Atmos. Sci*., 68, 2695–2709, doi: 10.1175/JAS-D-10-05016.1.

Birchard, T. MS, 1999: Investigation of Radar Reflectivity and Rain Rates in Hawaii.

Bell, M.M., R.A. Ballard, M. Bauman, A.M. Foerster, A. Frambach, K.A. Kosiba, W. Lee, S.L. Rees, and J. Wurman, 2015: The Hawaiian Educational Radar Opportunity (HERO). *Bull. Amer. Meteor. Soc.,* **96**, 2167–2181

Cao, G., T. W. Giambelluca, D. E. Stevens, and T. A. Schroeder, 2007: Inversion Variability in the Hawaiian Trade Wind Regime. *Journal of Climate* 20, 1145-1160.

Chen, Y. and A.J. Nash, 1994: Diurnal Variation of Surface Airflow and Rainfall Frequencies on the Island of Hawaii. *Mon. Wea. Rev.,* 122, 34–56, https://doi.org/10.1175/1520-0493(1994)122<0034:DVOSAA>2.0.CO;2 .

Chen, Y. and J. Feng, 1995: The Influences of Inversion Height on Precipitation and Airflow over the Island of Hawaii. *Mon. Wea. Rev.,* 123, 1660–1676, https://doi.org/10.1175/1520-0493(1995)123<1660:TIOIHO>2.0.CO;2

Cooporative Institute for Research in the Atmosphere. *Orographic Rain Index (ORI) - Detailed Information.* 2010: http://rammb.cira.colostate.edu/research/goes-r/proving_ground/cira_product_list/orographic_rain_index_detailed.asp (accessed September 04, 2015).

Crum, T.D. and R.L. Alberty, 1993: The WSR-88D and the WSR-88D Operational Support Facility. *Bull. Amer. Meteor. Soc.,* 74, 1669–1687.

Durran, D. R., 1990: Mountain waves and downslope winds. Atmospheric Process over Complex Terrain, W. Blumen, Ed., Amer. Meteor. Soc., 59-81.

Espy, J. P., 1841: Philosophy of Storms. Boston, Little and Brown, 552pp.

Gunn, R. and G.D. Kinzer, 1949: THE TERMINAL VELOCITY OF FALL FOR WATER DROPLETS IN STAGNANT AIR. *J. Meteor.,* 6, 243–248.

Harley, T. M., and Y. Chen., 2010: Characteristics of Summer Trade Wind Rainfall over Oahu. *Wea. Forecasting* 25, 1797-1815.

Hong, S-Y., and J-O. J. Lim, 2006: The WRF single-moment 6-class microphysics scheme (WSM6). *J. Korean Meteor. Soc.*, **42,** 129–151.

Houze, R. A., Jr., 2012: Orographic effects on precipitating clouds, *Rev. Geophys*., 50, RG1001, doi:10.1029/2011RG000365.

Hughes, M., A. Hall, and R. Fovell, 2009: Blocking in Areas of Complex Topography, and Its Influence on Rainfall Distribution. *J. Atmos. Sci*., 66, 508–518, doi: 10.1175/2008JAS2689.1.

Janjic, Z. I., 2002: Nonsingular Implementation of the Mellor-Yamada Level 2.5 Scheme in the NCEP Meso Model. *NCEP Office Note No. 437,* 66 pp.

Jiang, Q. and R. Smith, 2003: Cloud Timescales and Orographic Precipitation. J. *Atmos. Sci.*, 60, 1543–1559, doi: 10.1175/2995.1.

Kirshbaum, D. and D. Durran, 2004: Factors Governing Cellular Convection in Orographic Precipitation. *J. Atmos. Sci*., 61, 682–698, doi: 10.1175/1520-0469(2004)061<0682:FGCCIO>2.0.CO;2.

Kodama, K. and G. Barnes, 1997: Heavy Rain Events over the South-Facing Slopes of

Hawaii: Attendant Conditions. *Wea. Forecasting*, 12, 347–367, doi: 10.1175/1520-0434(1997)012<0347:HREOTS>2.0.CO;2.

Kodama, K. and S. Businger, 1998: Weather and Forecasting Challenges in the Pacific Region of the National Weather Service. *Wea. Forecasting*, 13, 523–546, doi: 10.1175/1520-0434(1998)013<0523:WAFCIT>2.0.CO;2.

Kunz, M. and C. Kottmeier, 2006: Orographic Enhancement of Precipitation over Low Mountain Ranges. Part I: Model Formulation and Idealized Simulations. *J. Appl. Meteor. Climatol.,* 45, 1025–1040, doi: 10.1175/JAM2389.1.

Lin, Y., S. Chiao, T. Wang, M. Kaplan, and R. Weglarz, 2001: Some Common Ingredients for Heavy Orographic Rainfall. *Wea. Forecasting*, 16, 633–660, doi: 10.1175/1520-0434(2001)016<0633:SCIFHO>2.0.CO;2.

Lyman, R., T. Schroeder, and G. Barnes, 2005: The Heavy Rain Event of 29 October 2000 in Hana, Maui. *Wea. Forecasting*, 20, 397–414, doi: 10.1175/WAF868.1.

Mlawer, E. J., S. J. Taubman, P. D. Brown, M. J. Iacono, and S. A. Clough, 1997: Radiative transfer for inhomogeneous atmosphere: RRTM, a validated correlated-k model for the longwave. *J. Geophys. Res*., 102 (D14), 16663–16682.

Murphy, M. and S. Businger, 2011: Orographic Influences on an Oahu Flood. *Mon. Wea. Rev*., 139, 2198–2217, doi: 10.1175/2010MWR3357.1.

Nugent, A, R. Smith, J. Minder, 2014: Wind Speed Control of Tropical Orographic Convection. *J. Atmos. Sci*., 71, 2695-2712. doi:10.1175/JAS-D-13-0399.1.

Schär, C. and R. Smith, 1993: Shallow-Water Flow past Isolated Topography. Part I: Vorticity Production and Wake Formation. *J. Atmos. Sci*., 50, 1373–1400, doi:

10.1175/1520-0469(1993)050<1373:SWFPIT>2.0.CO;2.

Schroeder, T.A., 1977: Meteorological Analysis of an Oahu Flood, *Mon. Wea. Rev*., 105:4, 458-468, doi: *10.1175/1520-0493(1977)105<0458:MAOAOF>2.0.CO;2*

Smith, R. and I. Barstad, 2004: A Linear Theory of Orographic Precipitation. *J. Atmos. Sci*., 61, 1377–1391, doi: 10.1175/1520-0469(2004)061<1377:ALTOOP>2.0.CO;2.

Smith, R. B., 2003: A linear upslope-time-delay model of orographic precipitation, mountain hy resources. *J. Hydrol*, 282, 2–9.

Van Nguyen, H., Y. Chen, and F. Fujioka, 2010: Numerical Simulations of Island Effects on Airflow and Weather during the Summer over the Island of Oahu. *Mon. Wea. Rev*., 138, 2253–2280, doi: 10.1175/2009MWR3203.1.

Watson, C. and T. Lane, 2012: Sensitivities of Orographic Precipitation to Terrain Geometry and Upstream Conditions in Idealized Simulations. *J. Atmos. Sci*., 69, 1208–1231, doi: 10.1175/JAS-D-11-0198.1.

Wilks, D. Statistical Methods in the Atmospheric Sciences, Volume 100 3rd Edition. Academic Press, 704pp.

Table 1 – List of HOP experiments showing the input used for the horizontal wind and moisture sources, the observations that the model was correlated to, and the method of correlation

Experiment	Brief Description	Horizontal Wind Source	Microphysics TPW Input	Correlated To	Compare Method
HOP1	Idealized Horizontal Wind	10 m/s idealized	NA	NA	NA
HOP2	Comparison to Vertical Wind Observations	WRF	NA	Vertical Wind Observations	Table 2
HOP3	February 2015 Operational Modeling	WRF	WRF	30 Min WSR-88D Average Reflectivity	Fig 5 Box Correlation
HOP4	Case Study: 09 March 2012	WRF	WRF	30 Min WSR-88D Average Reflectivity	Fig 5 Box Correlation
HOP5	Case Study: 03 November 2013	HERO Sounding	Hero Sounding	DOW Radar	Downwind Cell
HOP6	Case Study: 03 November 2013	WRF	WRF	DOW Radar	Downwind Cell
HOP7	Case Study: 24 August 2015	WRF	WRF	30 Min WSR-88D Average Reflectivity	Fig 5 Box Correlation

Table 2 – Modeled and measured average vertical wind speeds (m s^{-1}) and the percent difference between (Model-Observed) them between 20 October 2015 and 27 November 2015 at the five sampling locations.

Location	Date	Time (HST)	Model W (m/s)	Observed W (m/s)	% Difference
P	20-Oct	15	11.2	9.7	14.9
P	24-Oct	12	7.1	4.5	44.8
P	27-Oct	10	10.2	9.9	2.8
P	27-Oct	11	11.4	12.7	-10.8
P	27-Oct	12	12.4	14.5	-15.9
P	27-Oct	2	12.5	15.3	-20.2
P	5-Nov	9	13.0	8.5	42.1
P	5-Nov	10	12.3	11.3	8.5
D	5-Nov	11	7.9	5.1	43.1
K	7-Nov	9	8.2	11.1	-30.1
M	15-Nov	11	N/A	10.0	N/A
H	27-Nov	15	7.0	5.8	18.8
H	27-Nov	15	9.4	7.5	22.5

Table 3 – Twelve hours of Froude number data from 09 March 2012

Time (UTC)	Froude #
0600	1.20
0700	1.36
0800	1.41
0900	1.36
1000	1.39
1100	1.49
1200	1.17
1300	1.58
1400	1.49
1500	1.51
1600	1.35
1700	1.33
1800	1.21

Table 4 – Summary of January 2016 rainfall observations, modeled rainfall, and errors in the model.

Number of Rain Gauge Stations	56
Rain Gauge Rainfall Total (mm)	1219.4
CTRL Rainfall Total (mm)	668
EXP Rainfall Total (mm)	709.4
Percent Error CTRL	45.2%
Percent Error EXP	41.8%
Total Count of Observed Rain	306
Total Count of No Observed Rain	998
Total Count of Observations	1304
Percent Error CTRL During Rain	23.2%
Percent Error EXP During Rain	22.8%

Table 5 – Precipitation data from the rain gauge at 21.33°N, 157.80°W with precipitation output from the CTRL and EXP model runs through the month of January 2016.

Date	Observed(mm)	CTRL (mm)	EXP (mm)
20160103	0	0	0
20160104	0	0	0
20160105	0	0	0
20160106	37.8	1.4	1.7
20160107	33.5	0.3	0
20160108	0	0	0
20160109	0	0.7	0.7
20160110	0	2.4	4.3
20160111	0	0	0
20160112	0	0	0
20160113	0	0	0
20160114	0	0	0
20160115	0	0.6	0.6
20160118	0	0	0
20160119	0	0	0
20160120	0.3	0	0
20160121	2.5	0.9	0.7
20160122	0	0	0
20160123	0	0.5	0.5
20160124	0	0	0
20160125	1.8	0.3	0.3
20160126	9.7	0	0
20160127	0	0.3	0
20160128	0	0.4	0
Total:	85.6	7.8	8.8

Table 6 – a) Relationship between counts of radar observed precipitation and forecast precipitation occurrence for the EXP model run. b) Same as A but for the CTRL run

a

FORECAST	OBSERVED: YES	OBSERVED: NO
YES	12136	782
NO	2528	40354

b

FORECAST	OBSERVED: YES	OBSERVED: NO
YES	12731	1566
NO	2276	39227

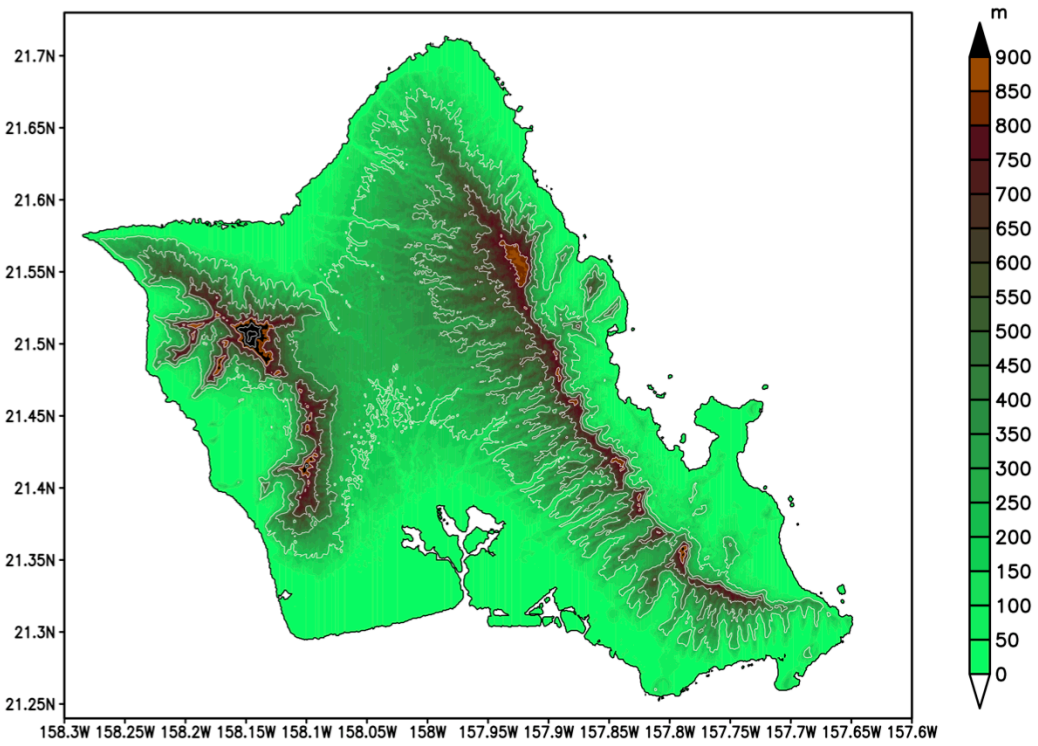

Fig 1 - Topographic map of Oahu. White contours are every 250 m. Color shading is changed every 50 m up to 900 m. Heights above 900 m are black.

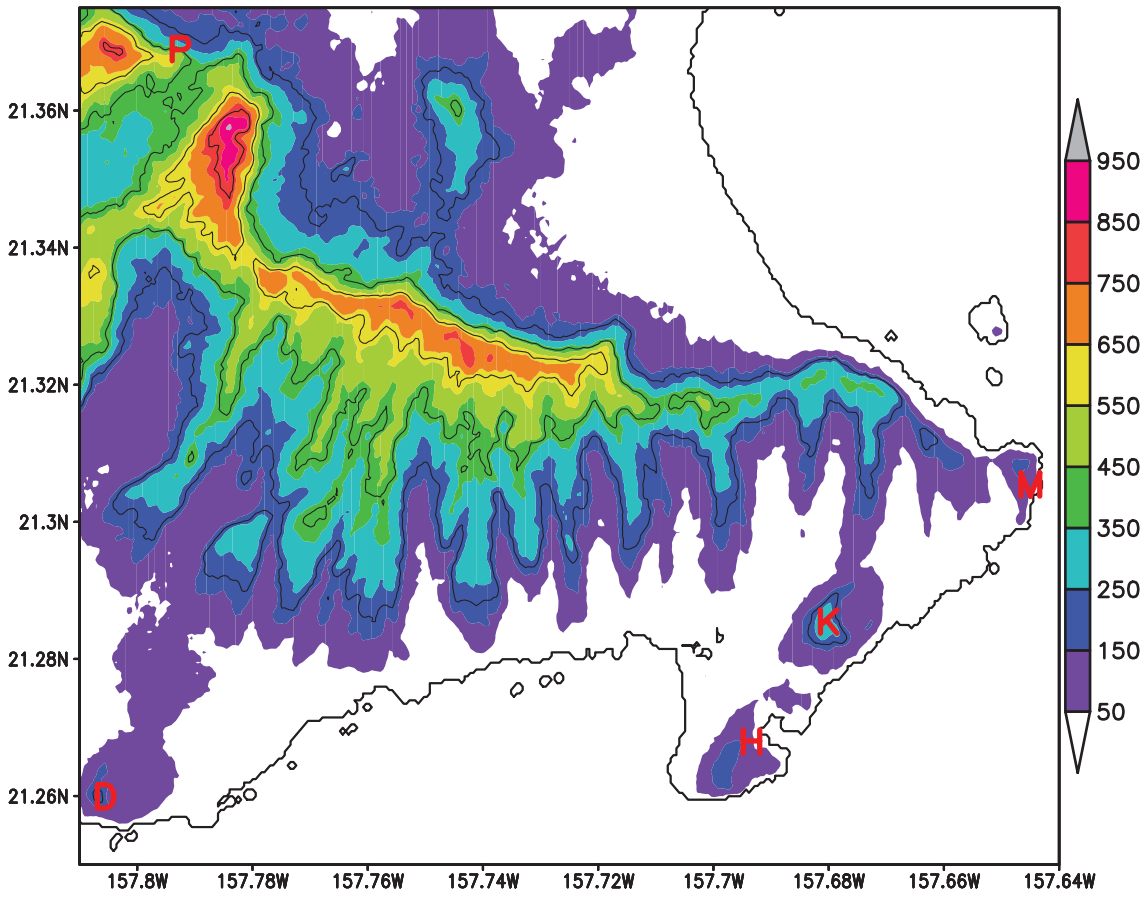

Fig 2 – Terrain heights in meters (color) of southeastern Oahu with contours every 200 m. Wind measurement locations are marked with red colors. D- Diamond Head Trail Summit, K- Koko Crater Summit, H- Koko Head, M- Makapʻu Lighthouse Train, P- Pali-Nuʻuanu Lookout.

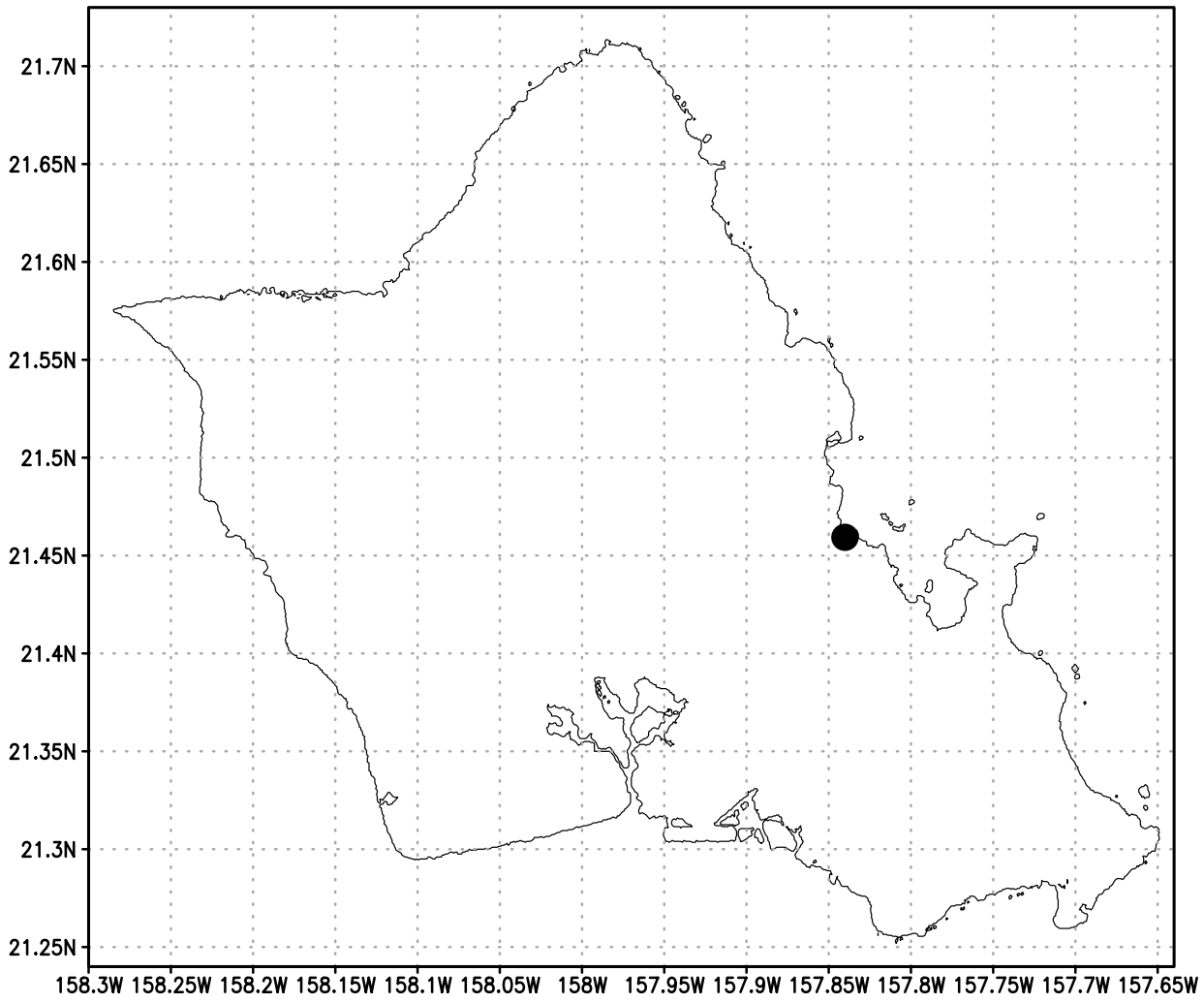

Fig 3 – Map of Oahu with a black dot over Kahaluʻu showing the location of the DOW radar and radiosonde launch site during IOP7 of HERO.

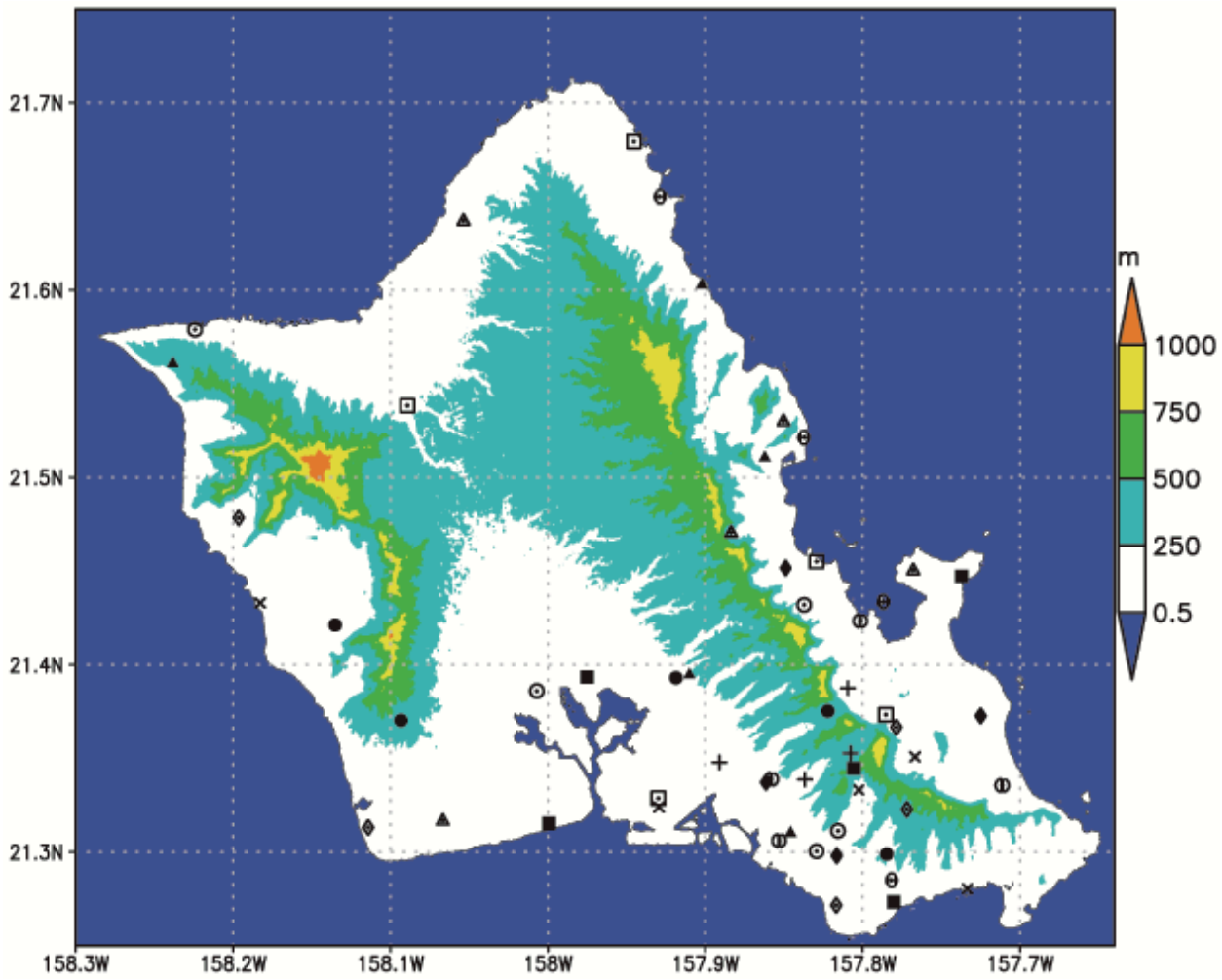

Fig 4 – Map of rain gauge locations around the island of Oahu. Each gauge is marked with a dot, square, diamond, or triangle. High resolution terrain heights are plotted every 250 m.

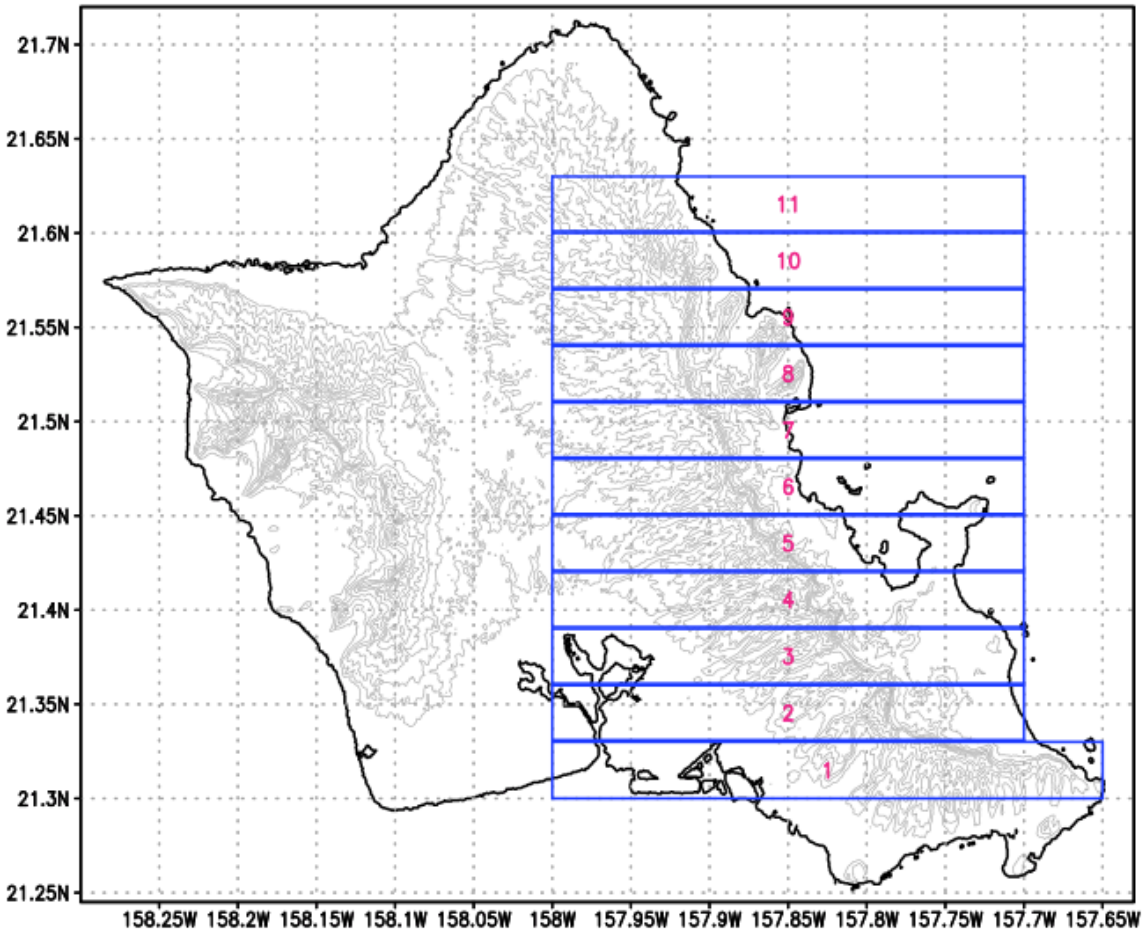

Fig 5 - Topographic Map of Oahu with grey contours every 100 m. Blue numbered boxes are 0.03° latitude in the north-south direction and vary in the east-west direction to cover the Koʻolau Mountains.

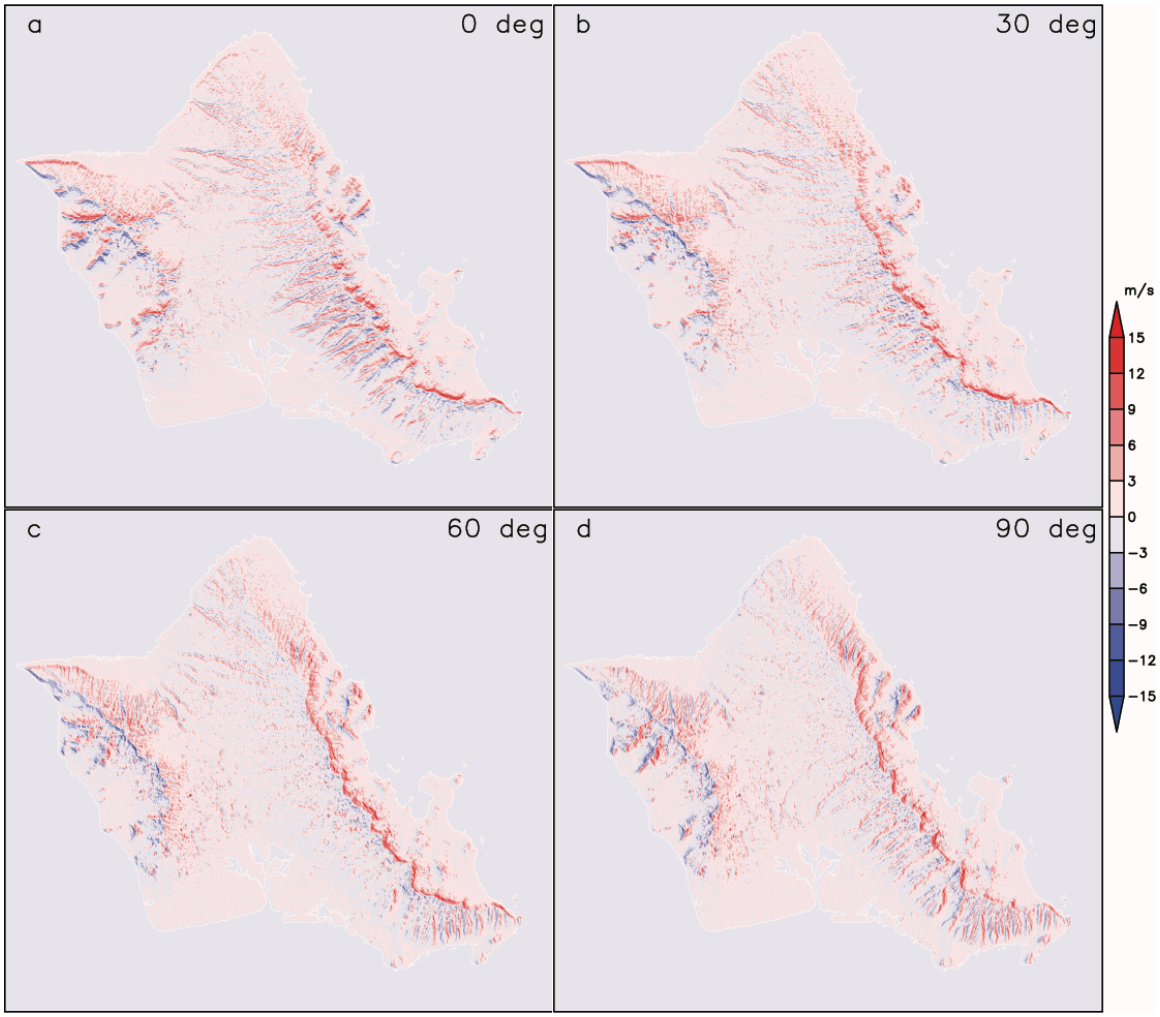

Fig 6 - Idealized high-resolution HOP model vertical motion labeled with the direction of the horizontal wind everywhere 10 m s^{-1} from a) 0°, b) 30°, c) 60°, and d) 90°. The color bar to the right shows the magnitude of the vertical motion, with negative values being downward and positive values being upward.

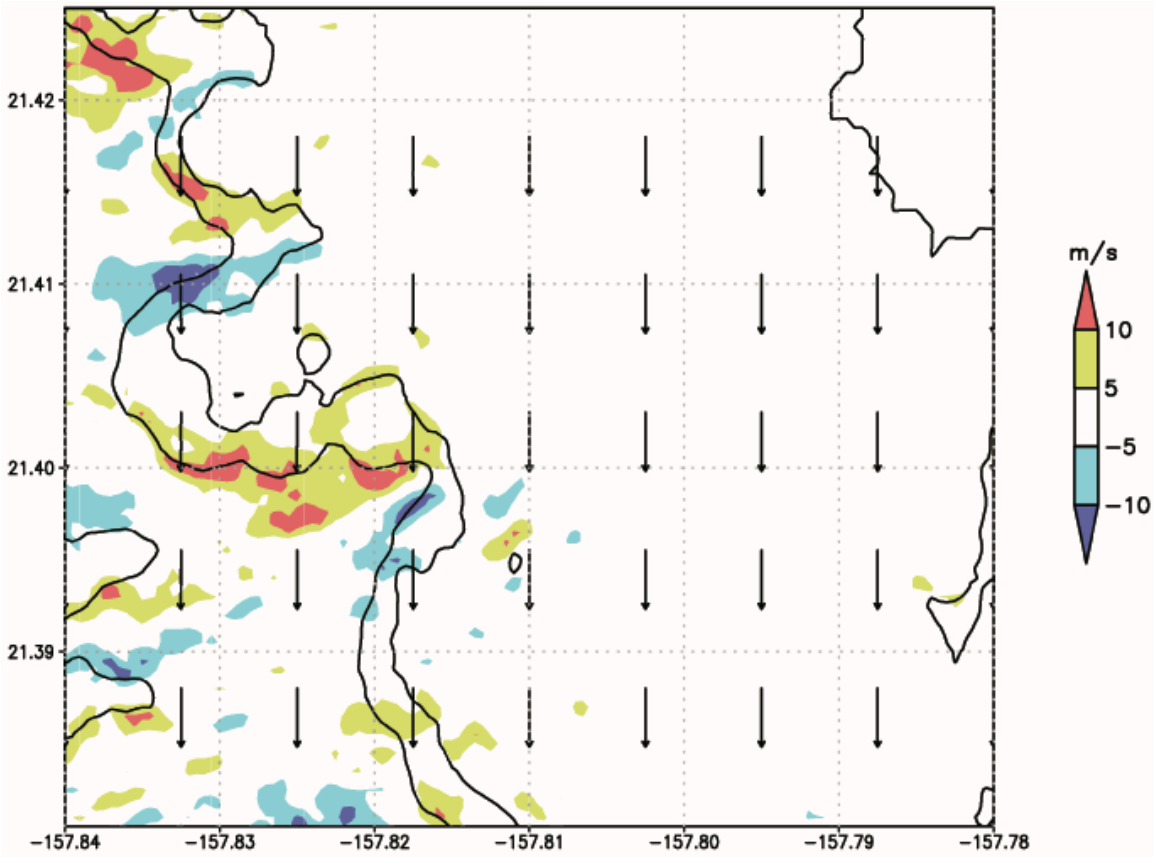

Fig 7 - Vertical motion (color fill) in m s^{-1} over a zoomed in area of the Ko‘olau Mountains using 10 m s^{-1} winds from 0° (vectors). Terrain height contours of 0, 200, and 400 m are drawn in black.

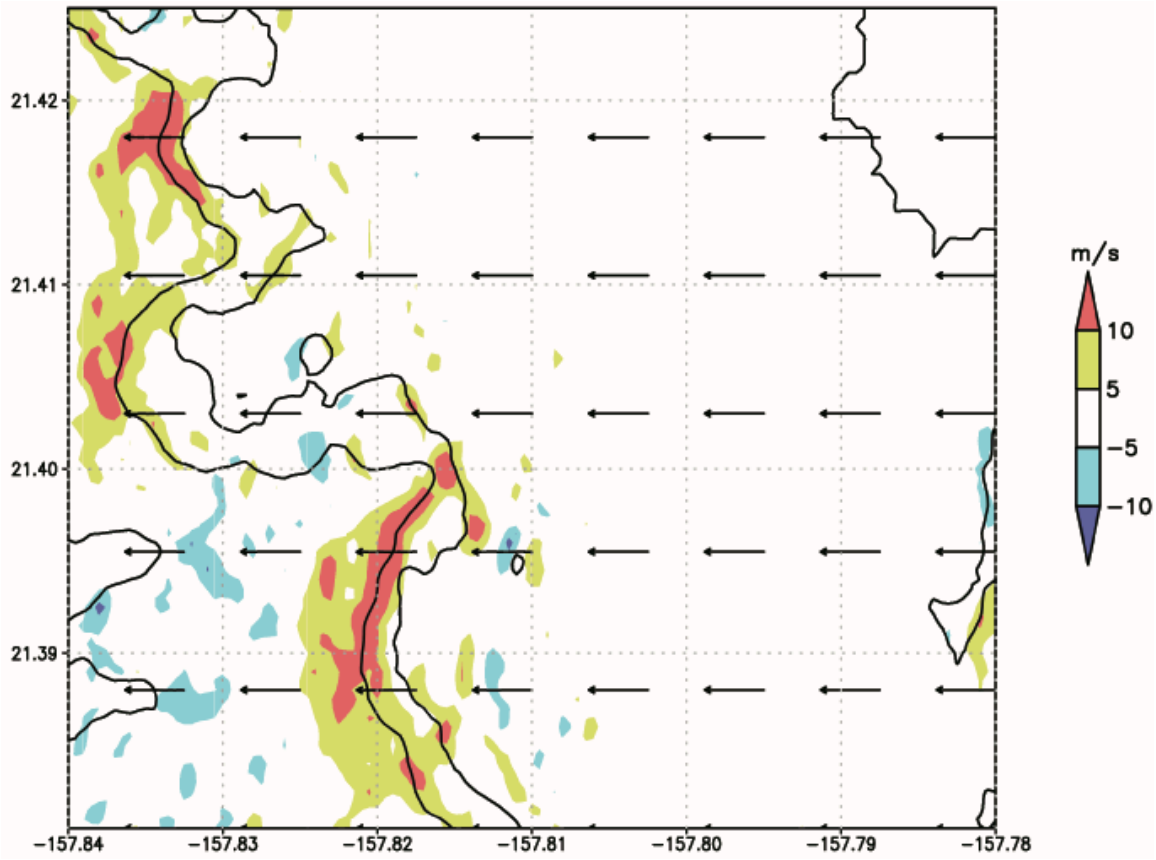

Fig 8 - Same as Fig 7 except horizontal winds are from 90°.

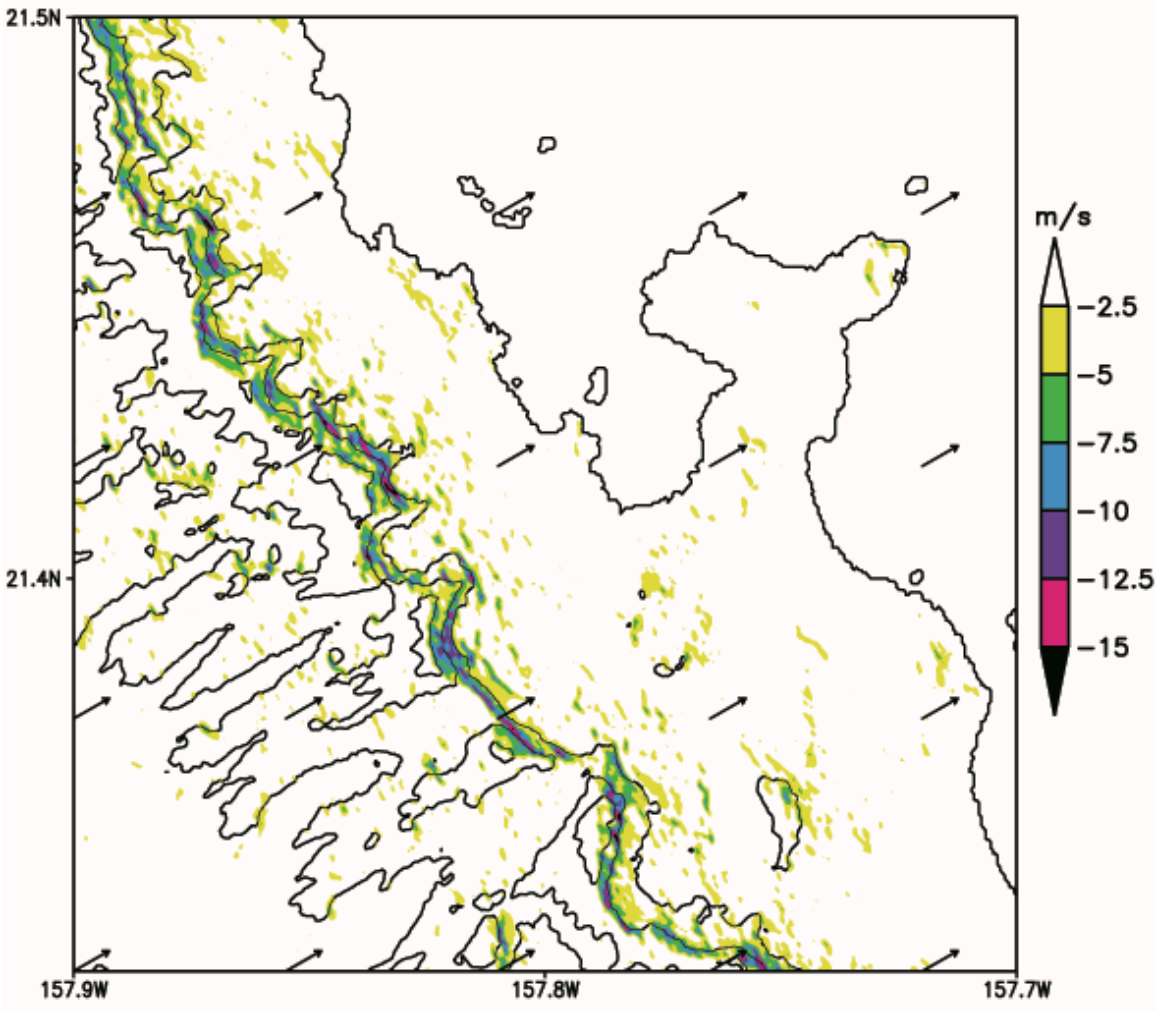

Fig 9 – Downward motion (color) over windward Oahu for 10 m s^{-1} idealized winds from 240° (vectors). Terrain heights are drawn every 250 m.

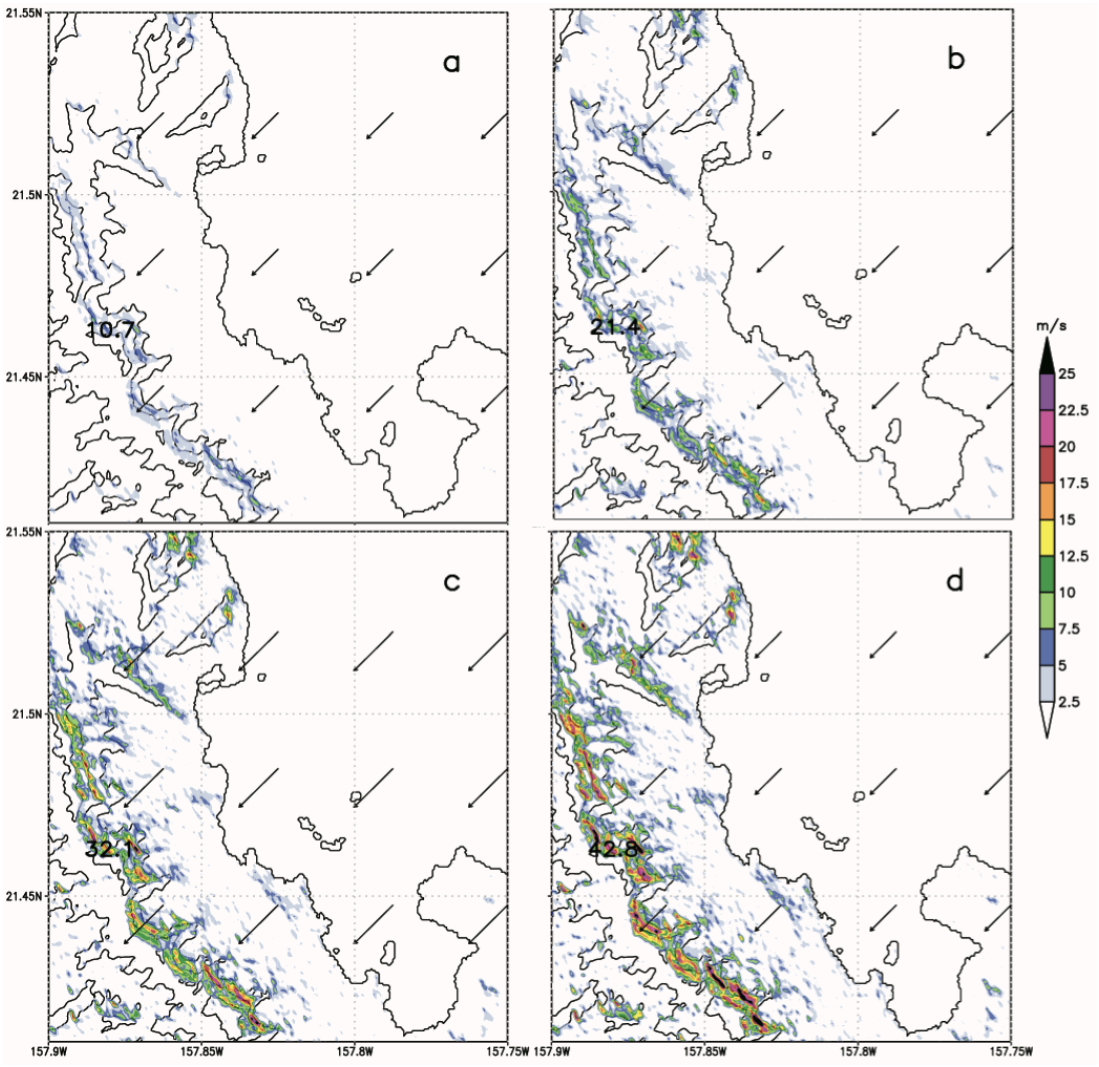

Fig 10 - Idealized HOP upward motion over the Ko‘olau Mountains using horizontal winds from 45° with speed of a) 5 m s^{-1} b) 10 m s^{-1} c) 15 m s^{-1}, and d) 20 m s^{-1}. The maximum vertical velocity for the domain is displayed over its location in m s^{-1}.

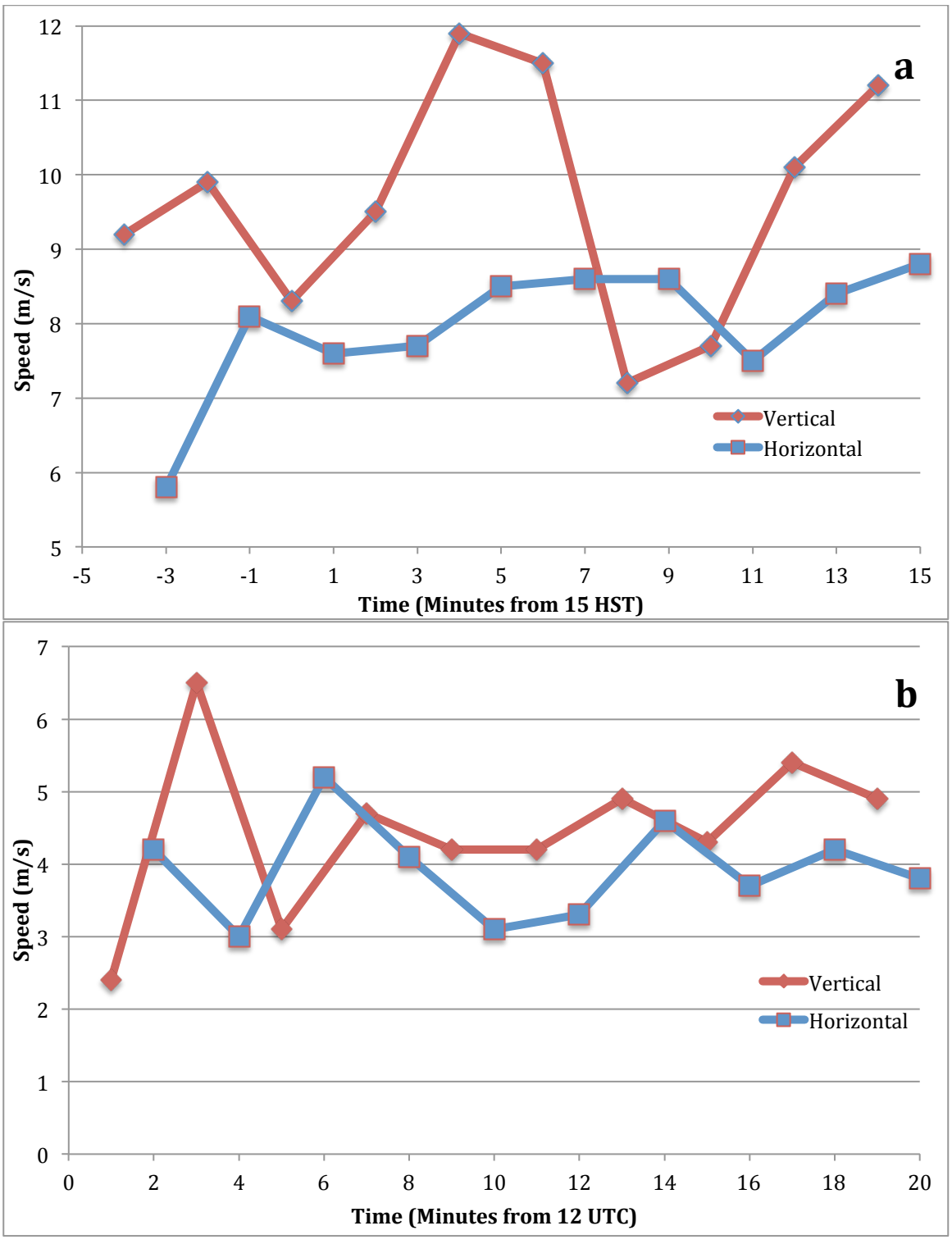

Fig 11 - One-minute averaged horizontal (red) and vertical (blue) wind speeds at the Pali Lookout on a) 20 October 2015 around 1500 HST and on b) 24 October 2015 around 1200 HST.

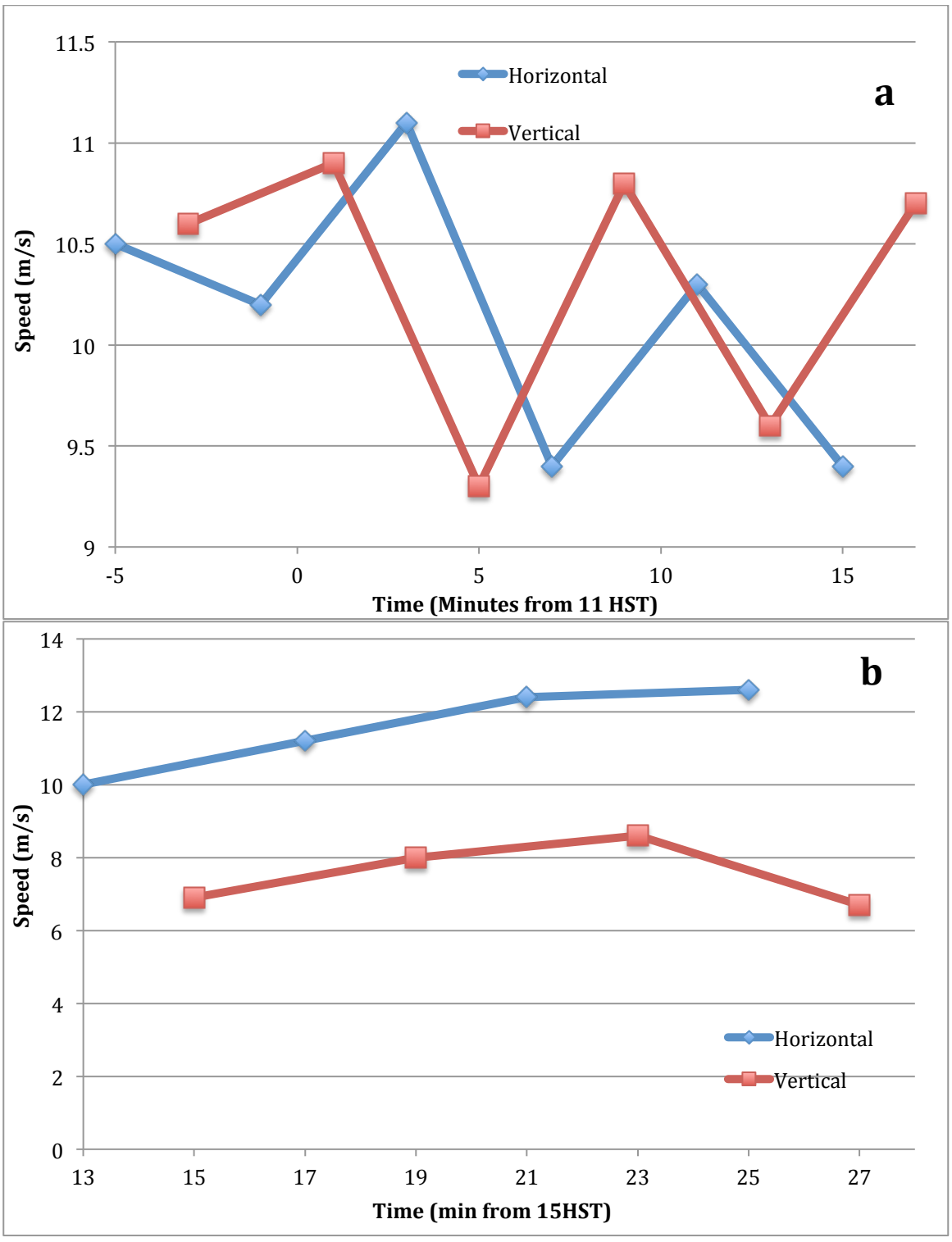

Fig 12 – Same as Fig 11 but a) at the Makapu‘u site on 15 November 2015 around 1100 HST. b) at the Koko-Head site on 27 November 2015 around 1500 HST.

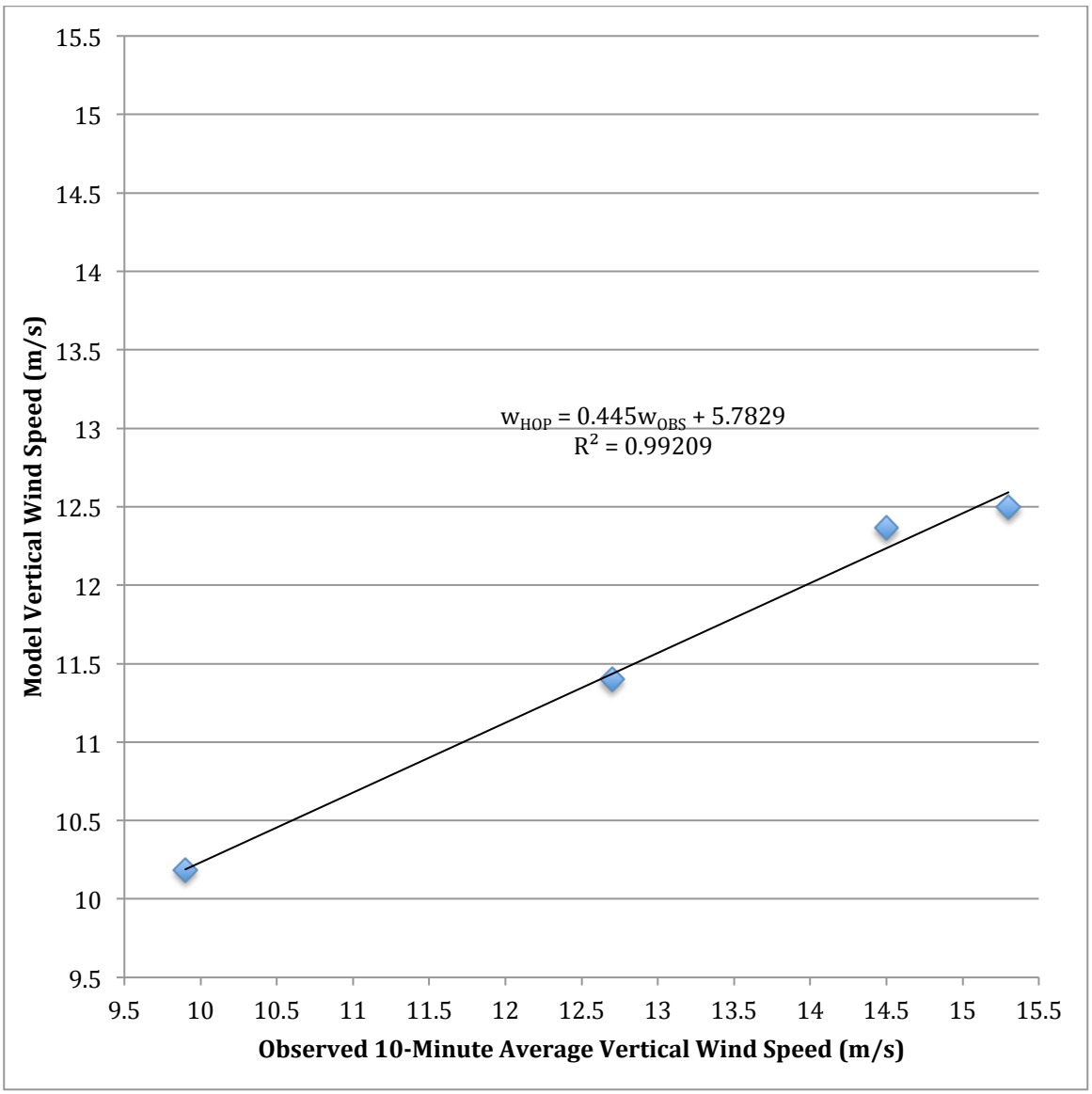

Fig 13 – Modeled (y-axis) vs observed 10-minute average (x-axis) vertical motion speeds in m s^{-1} on 27 October 2015 from 1000 HST to 1400 HST at the Pali Lookout. The best-fit line is displayed with the equation.

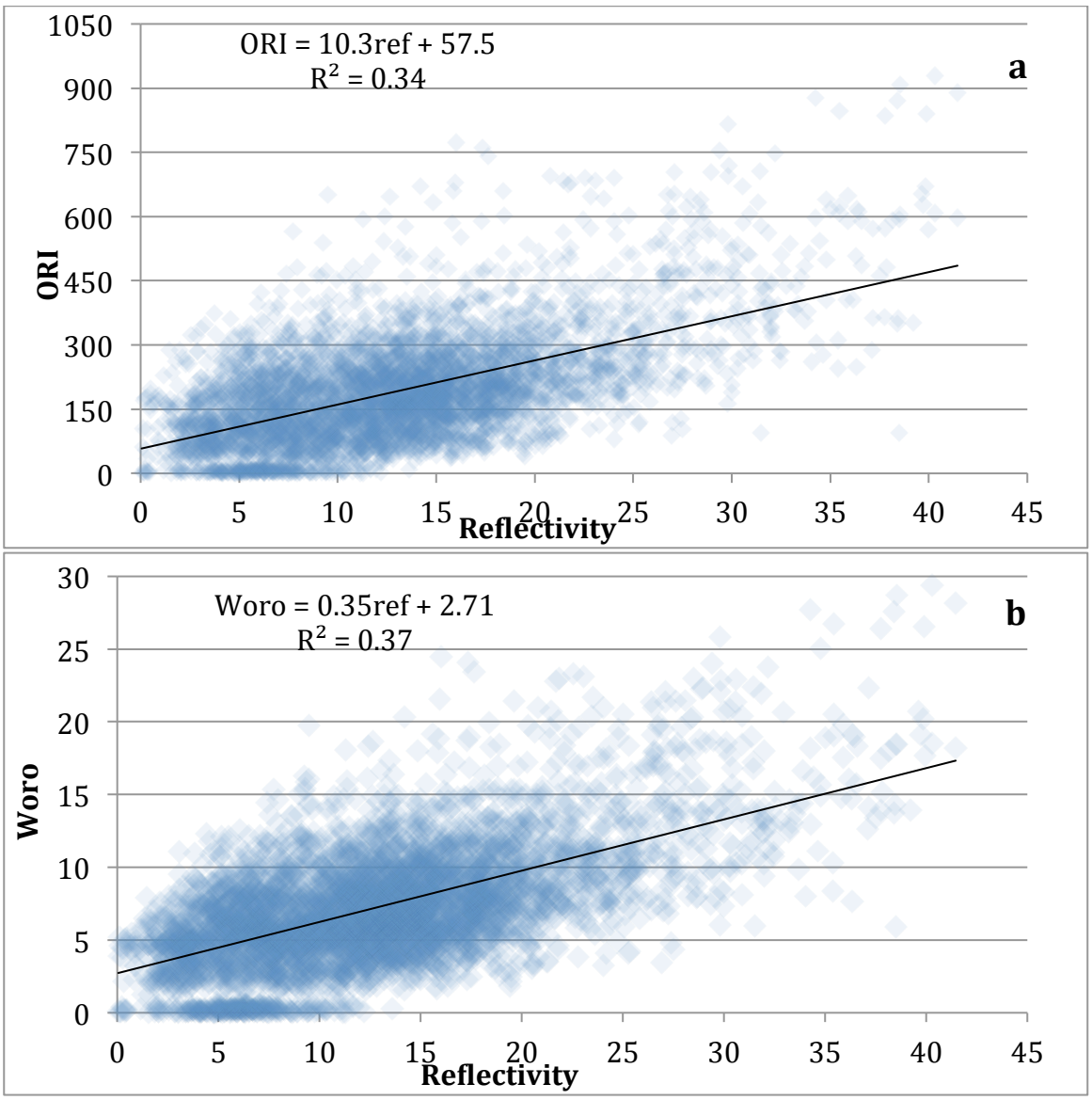

Fig 14 - Comparison of the maximum values of a) ORI (mm m s^{-1}) and b) w_{oro} (m s^{-1}) on the y-axis to the corresponding 15-minute averaged reflectivity maximum on the x-axis from the boxes in Fig 5 from 0 UTC on 03 February 2015 to 14 UTC 27 February 2015. The best-fit trend line is shown with its equation and the coefficient of determination (R^2) is displayed beneath the equation.

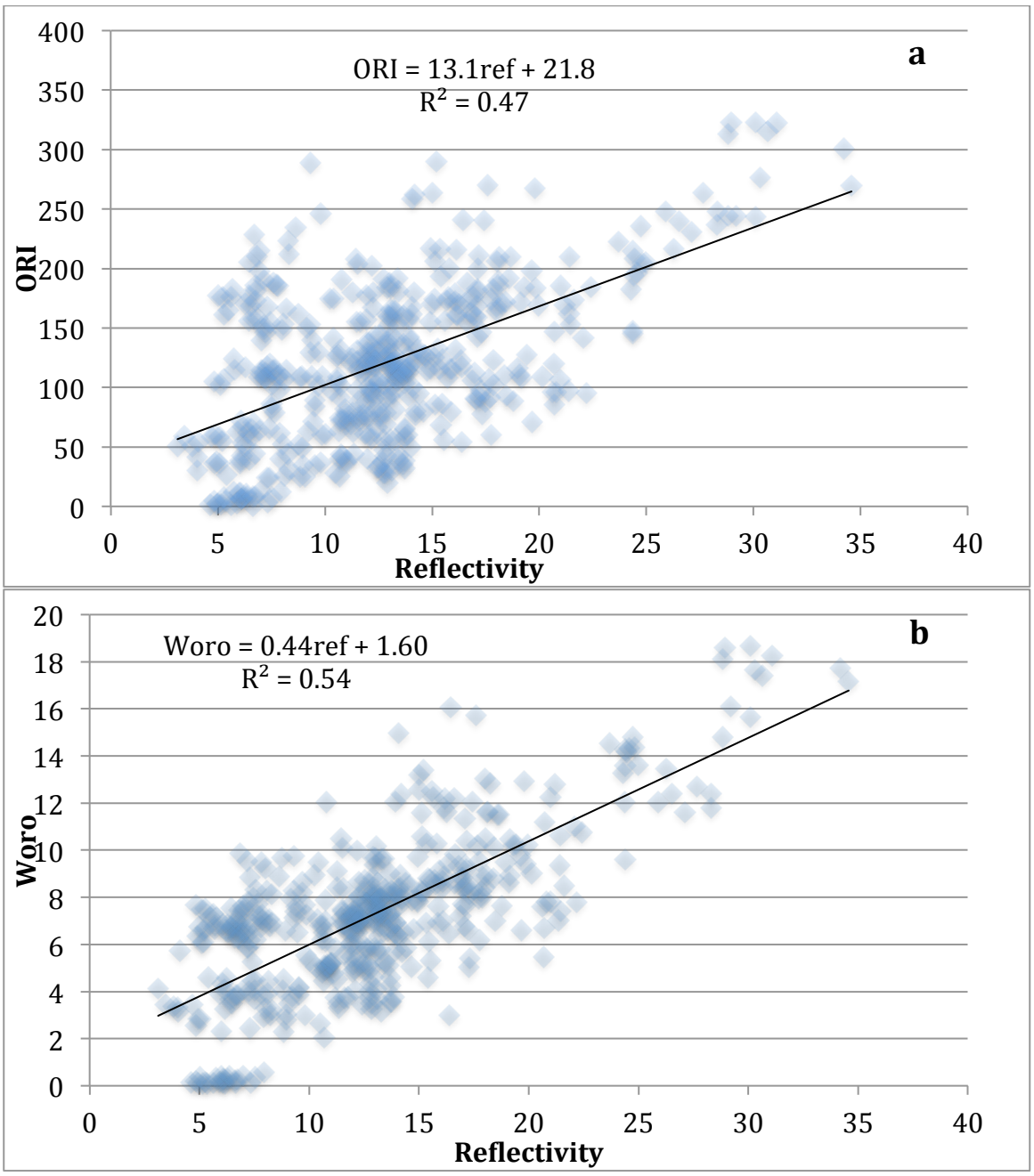

Fig 15 - Comparison of maximum values of a) ORI (mm m s^{-1}) and b) w_{oro} (m s^{-1}) on the y-axis to 15-minute averaged reflectivity on the x-axis from the boxes in Fig 5 averaged for a given time step from 0 UTC on 03 February 2015 to 14 UTC 27 February 2015. The best-fit trend line is shown with its equation and the coefficient of determination (R^2) is displayed beneath the equation.

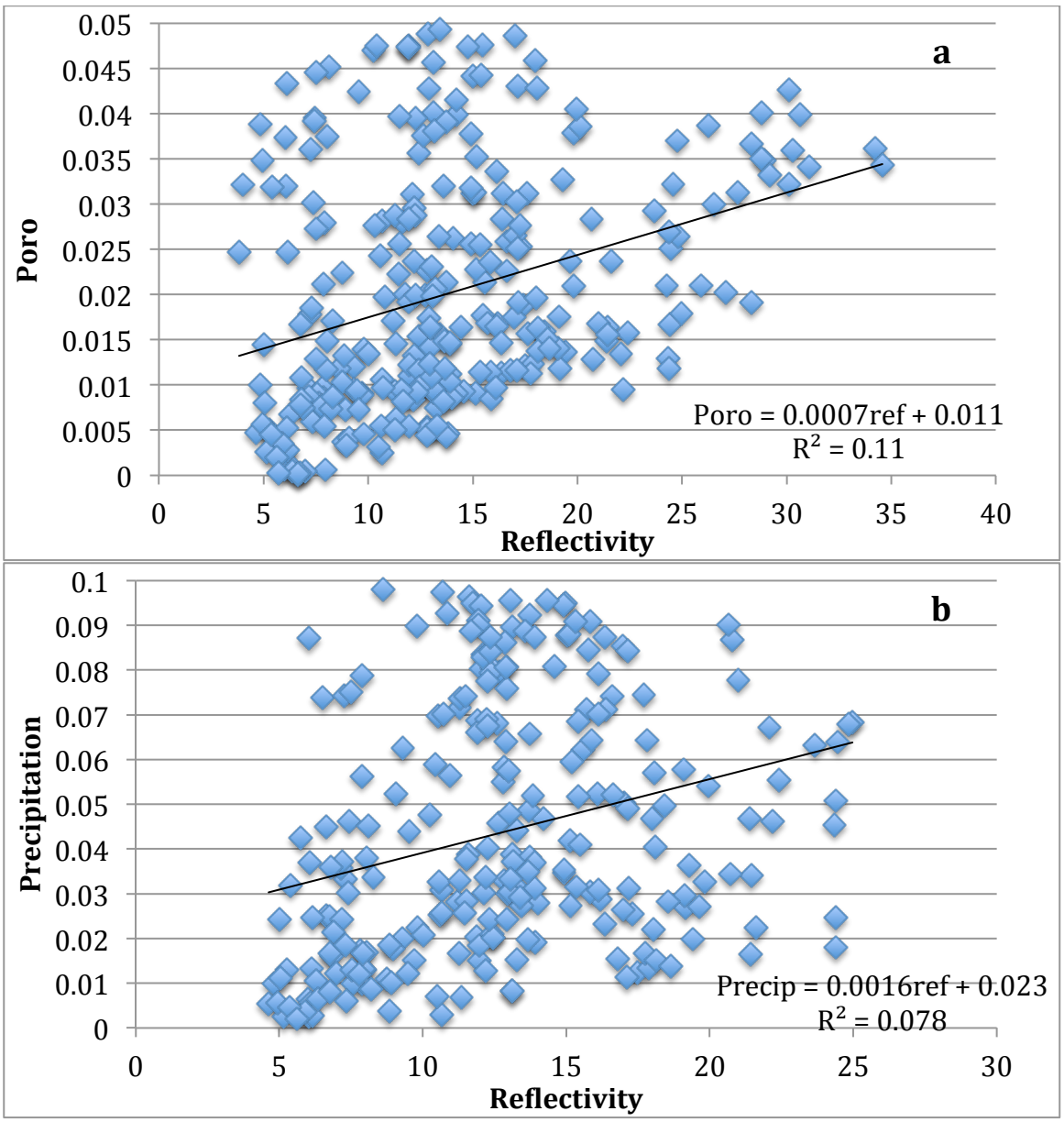

Fig 16 - Comparison of the maximum values of a) orographically generated Precipitation "Poro" (inches) and b) precipitation (inches) on the y-axis to the corresponding 15-minute averaged reflectivity maximum on the x-axis from the boxes in Fig 5 from 0 UTC on 03 February 2015 to 14 UTC 27 February 2015. The best-fit trend line is shown with its equation and the coefficient of determination (R^2) is displayed beneath the equation. The data have been capped at 0.05 in. for poro and 0.1 in. for precipitation.

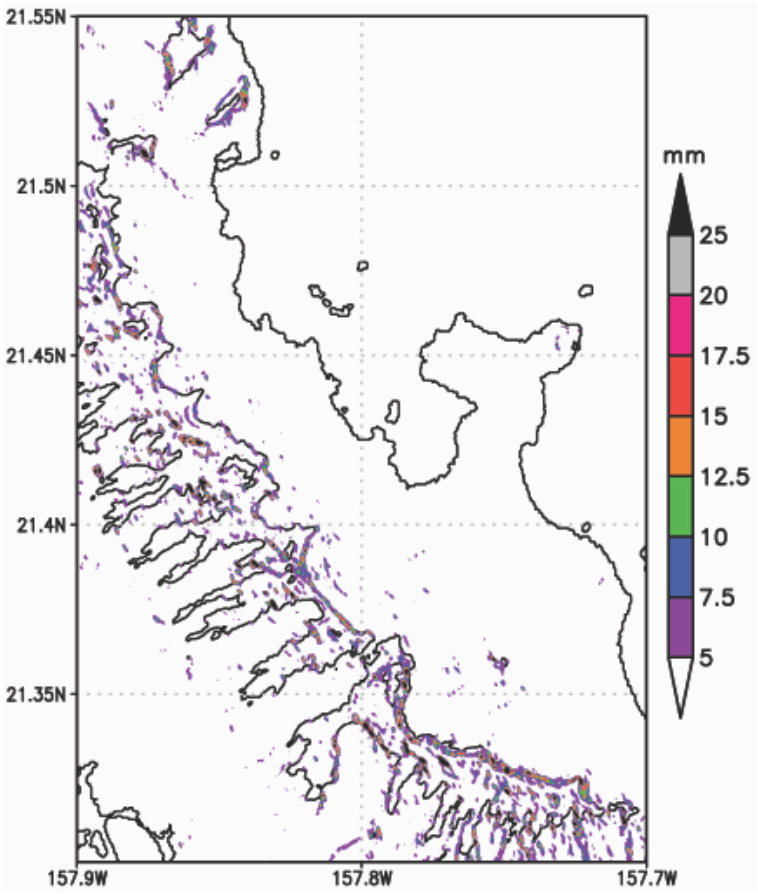

Fig 17 – Total February precipitation (mm) calculated from the w_{oro} and reflectivity relationship from Fig 15b along the Ko‘olau Mountains. Height contours occur every 400 m.

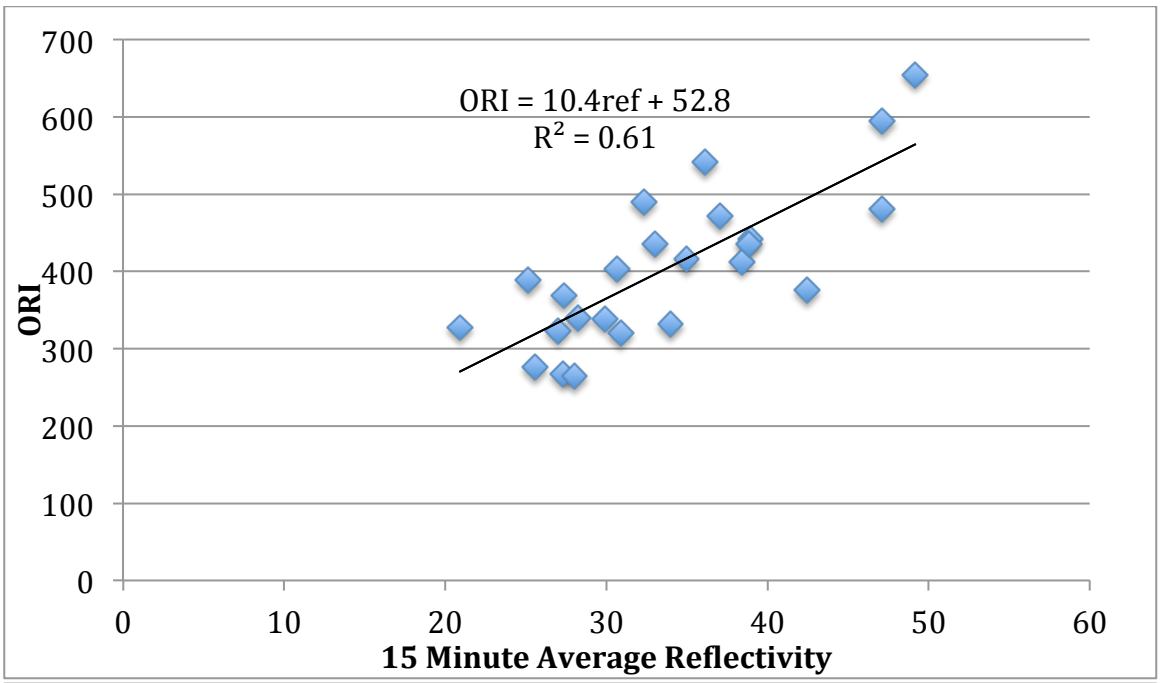

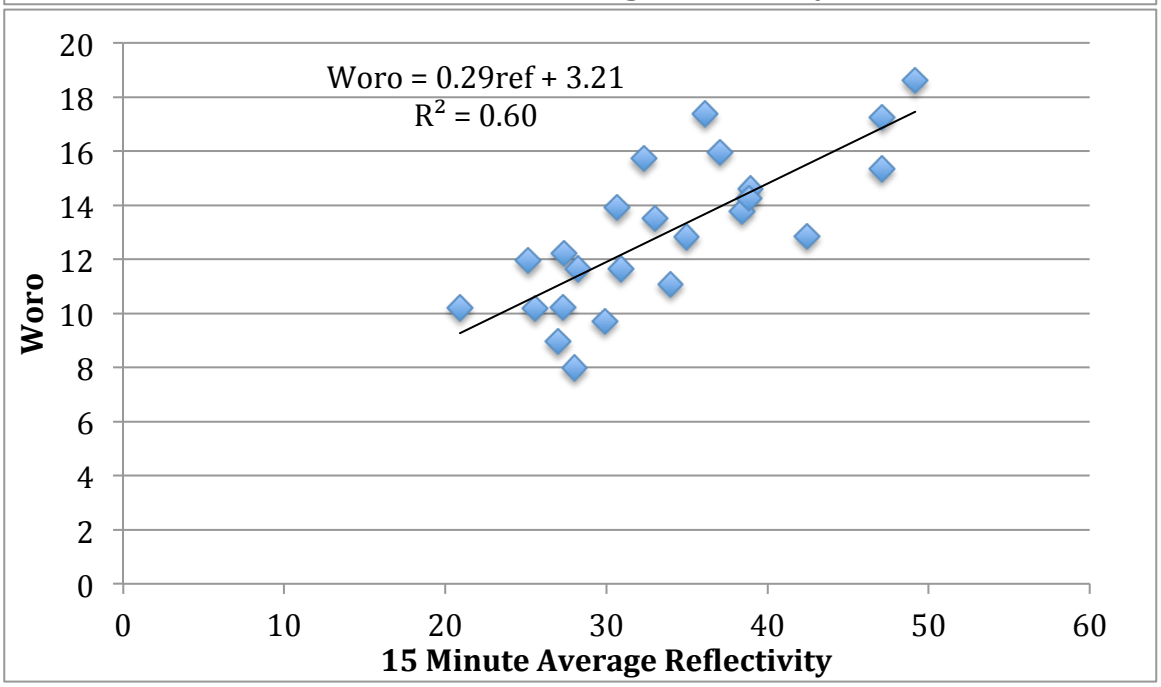

Fig 18 - Comparison of the maximum values of a) ORI (mm m s^{-1}) and b) w_{oro} (m s^{-1}) on the y-axis to 15-minute averaged reflectivity on the x-axis from the boxes in Fig 5 averaged for a given time step on 09 March 2012 from 0 UTC to 23 UTC. The best-fit trend line is shown with its equation and the coefficient of determination (R^2) is displayed beneath the equation.

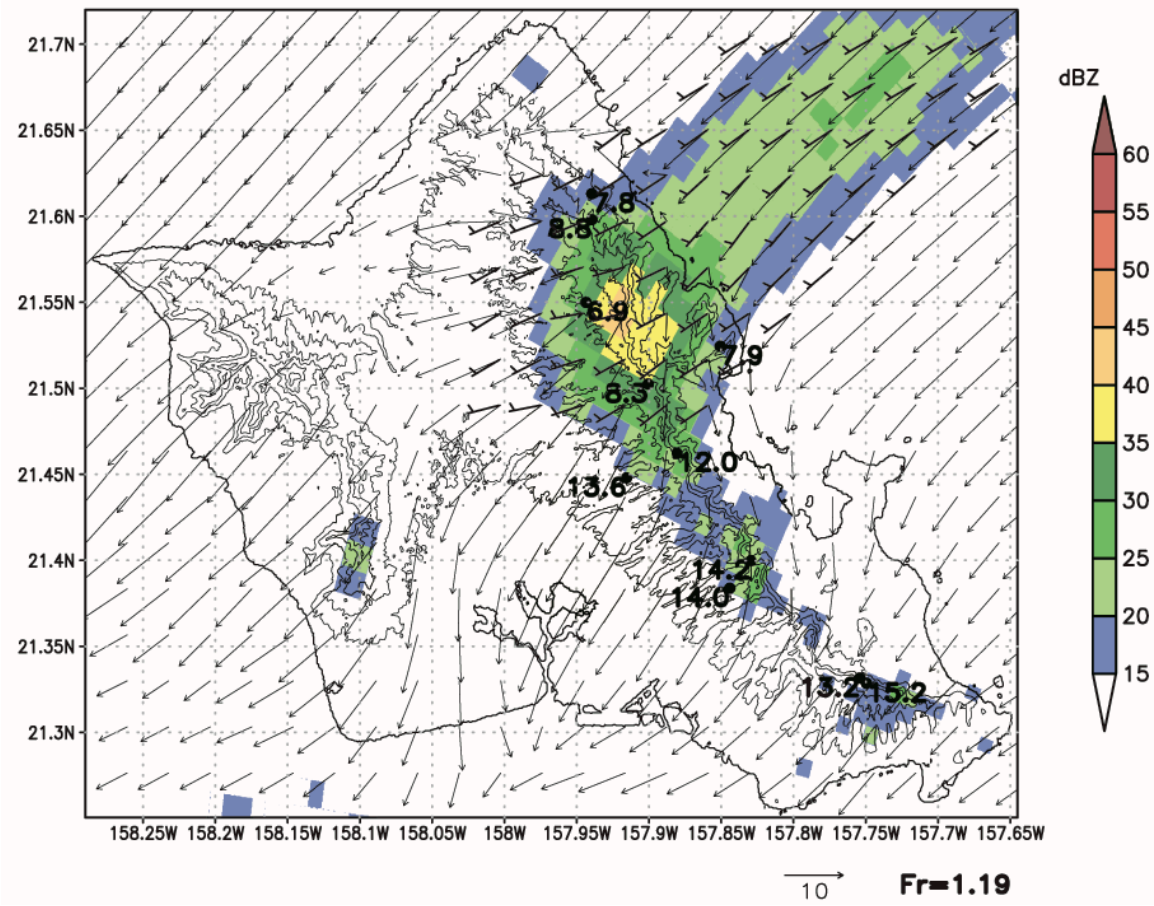

Fig 19 - Maximum forecasted vertical motion found for each boxed region in Fig 5 (black dots) overlaid on 15-minute averaged reflectivity from PHMO at 06 UTC on 09 March 2012 over Oahu. Contours show terrain heights every 200 m. Vectors show lowest sigma level WRF horizontal winds and are relative to the 10 m s^{-s} reference vector below the image. In order to avoid overlap of vectors, wind barbs are average in-cloud winds in m s^{-1}, and each full line represents 10 m s^{-s} and a half line represented 5 m s^{-1}. The Froude number (Fr) is to the right of the reference vector at the bottom of the figure.

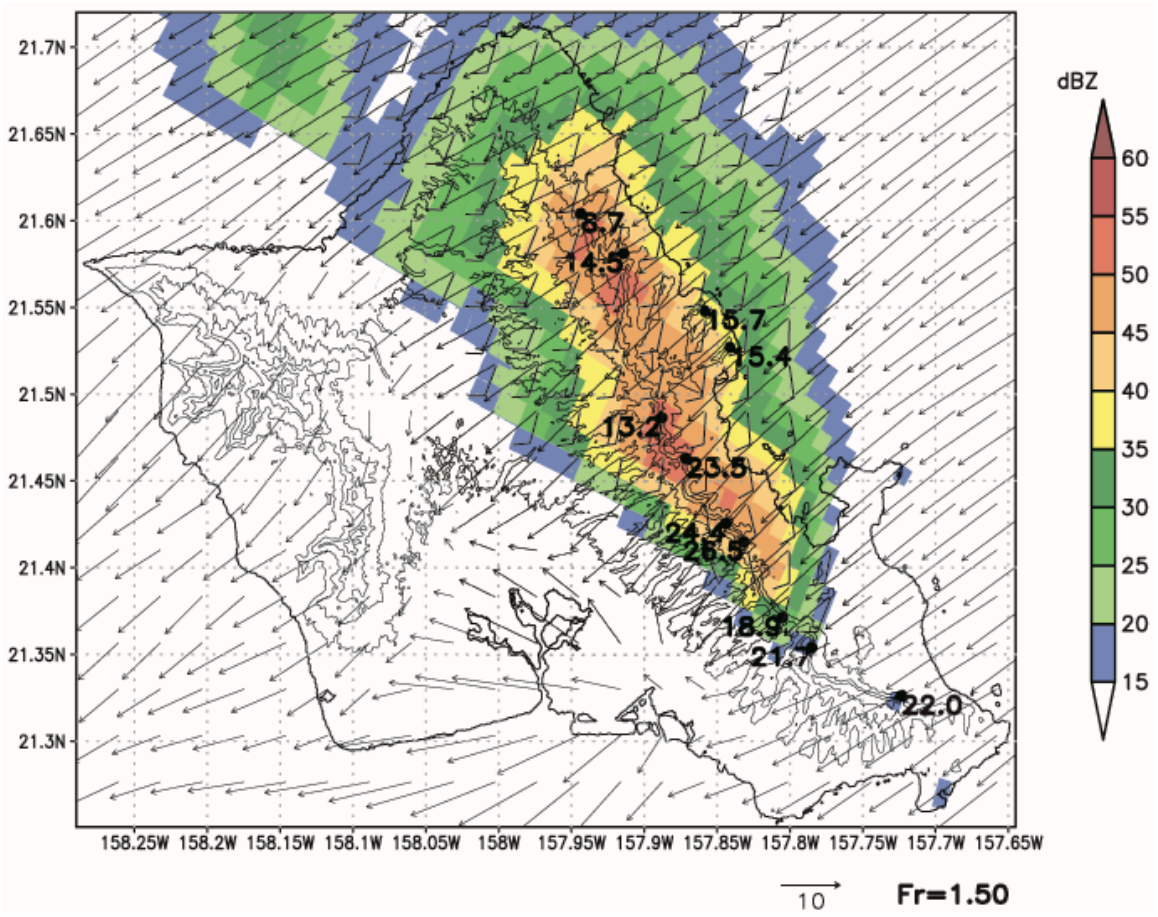

Fig 20 - Same as Fig 19 except at 1500 UTC.

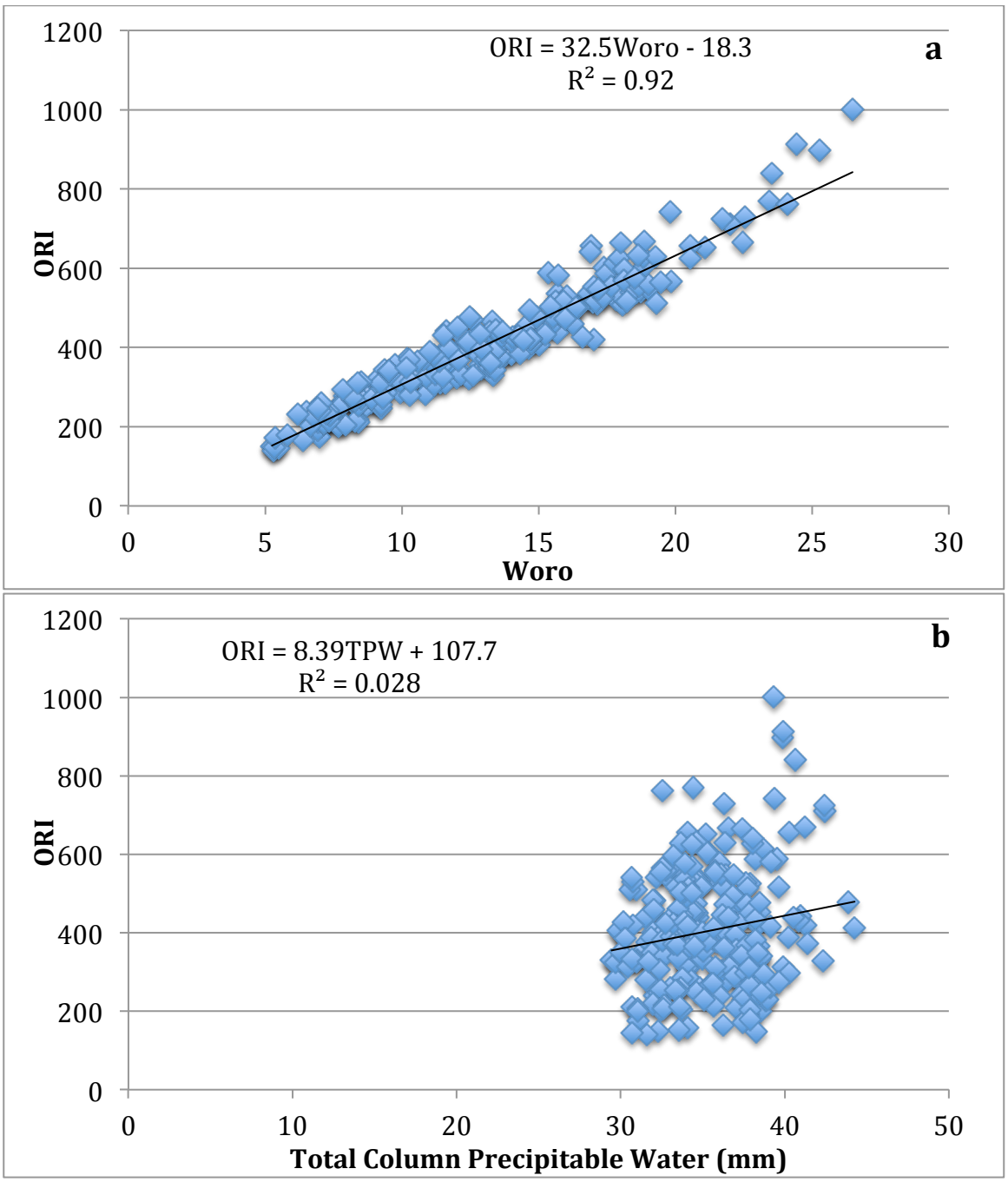

Fig 21 - Comparing orographic rainfall index (ORI) to a) orographically forced vertical motion (w_{oro}) and b) total precipitable water (TPW) on 09 March 2012. The best-fit line is plotted with the coefficient of determination (R^2) below the equation.

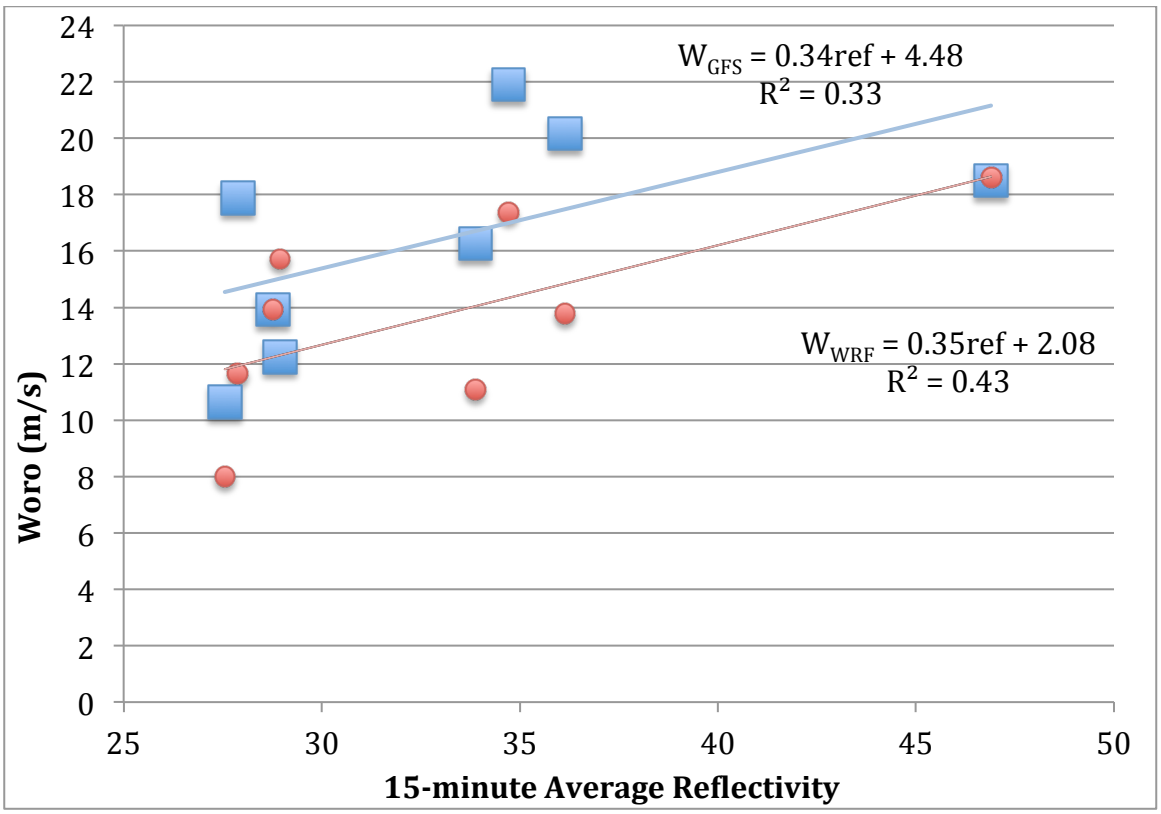

Fig 22 - Averages of the maxima of upward motion from each box in Fig 5 (y-axis) compared to the averages of the maxima of the 15-minute averaged reflectivity (x-axis) in the corresponding times and boxes. The blue squares represent the vertical motion calculated using the 850 hPa winds from the WRF model, and the red dots represent the vertical motion calculated from using the lowest sigma-level winds from the 3 km WRF model. The blue line and red line represent the best-fit line for each corresponding set of data, with the equations and coefficient of determination (R^2) displayed.

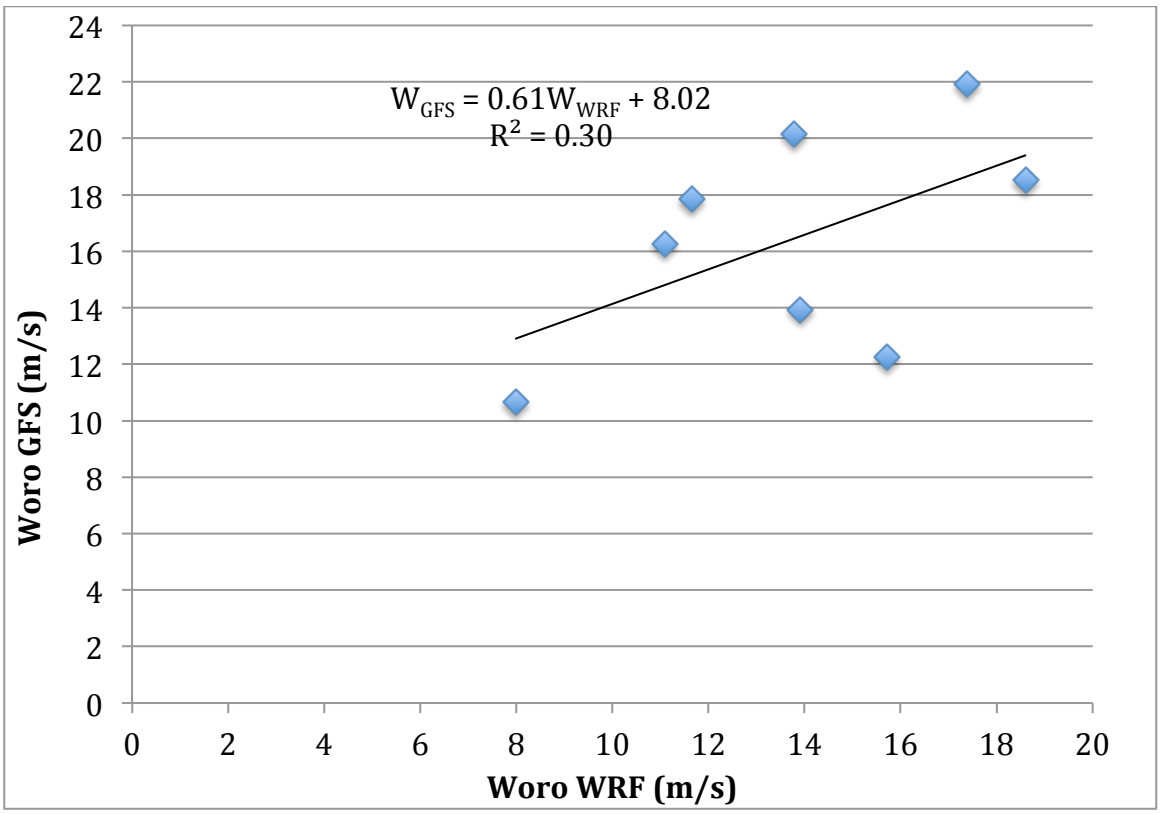

Fig 23 - Correlation between the average of the upward motion maxima found using the GFS 850 hPa (y-axis) wind and 3 km WRF lowest sigma-level wind (x-axis) at the same forecast time using the HOP model. The best-fit line is plot with the coefficient of determination (R^2) below the equation.

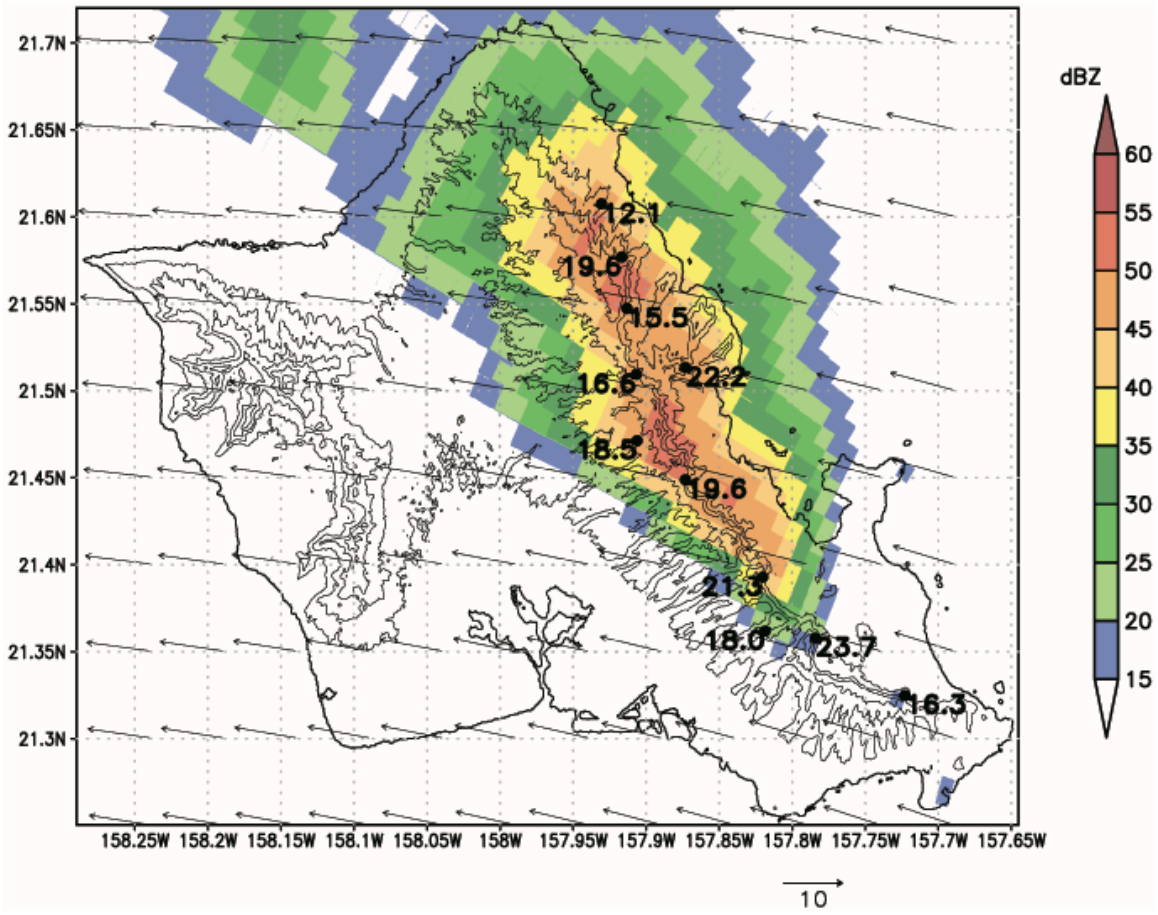

Fig 24 - Maximum forecasted vertical motion found using the GFS 850 hPa wind (vectors) for each boxed region in Fig 5 (dots) overlaid on 15-minute averaged reflectivity from PHMO at 15 UTC on 09 March 2012 over Oahu. Contours show terrain heights every 200 m.

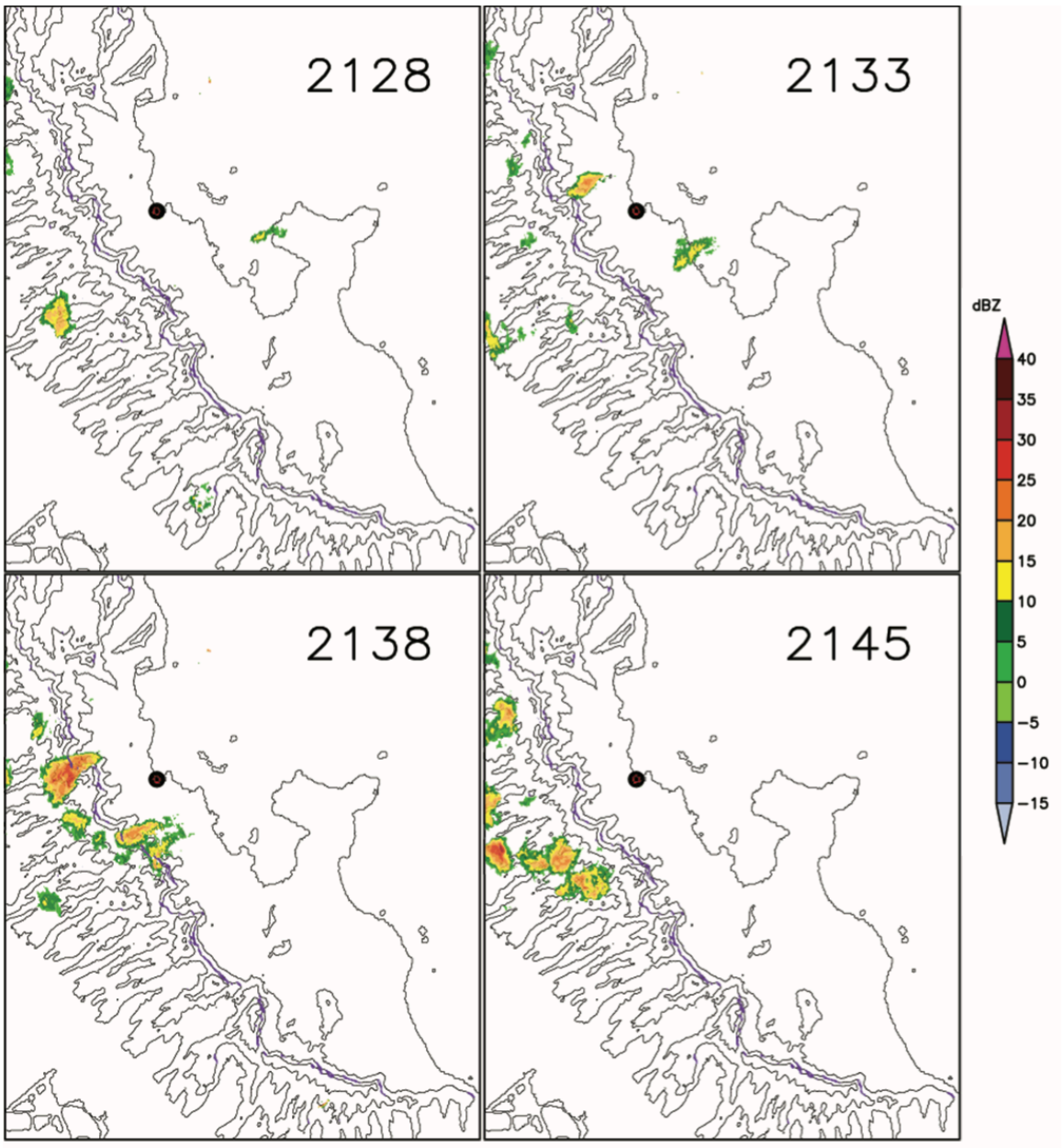

Fig 25 - Composite radar images over Oahu from 2128 UTC to 2145 UTC on 03 November 2013. Black dot indicates the radar site. Terrain is drawn every 200 m.

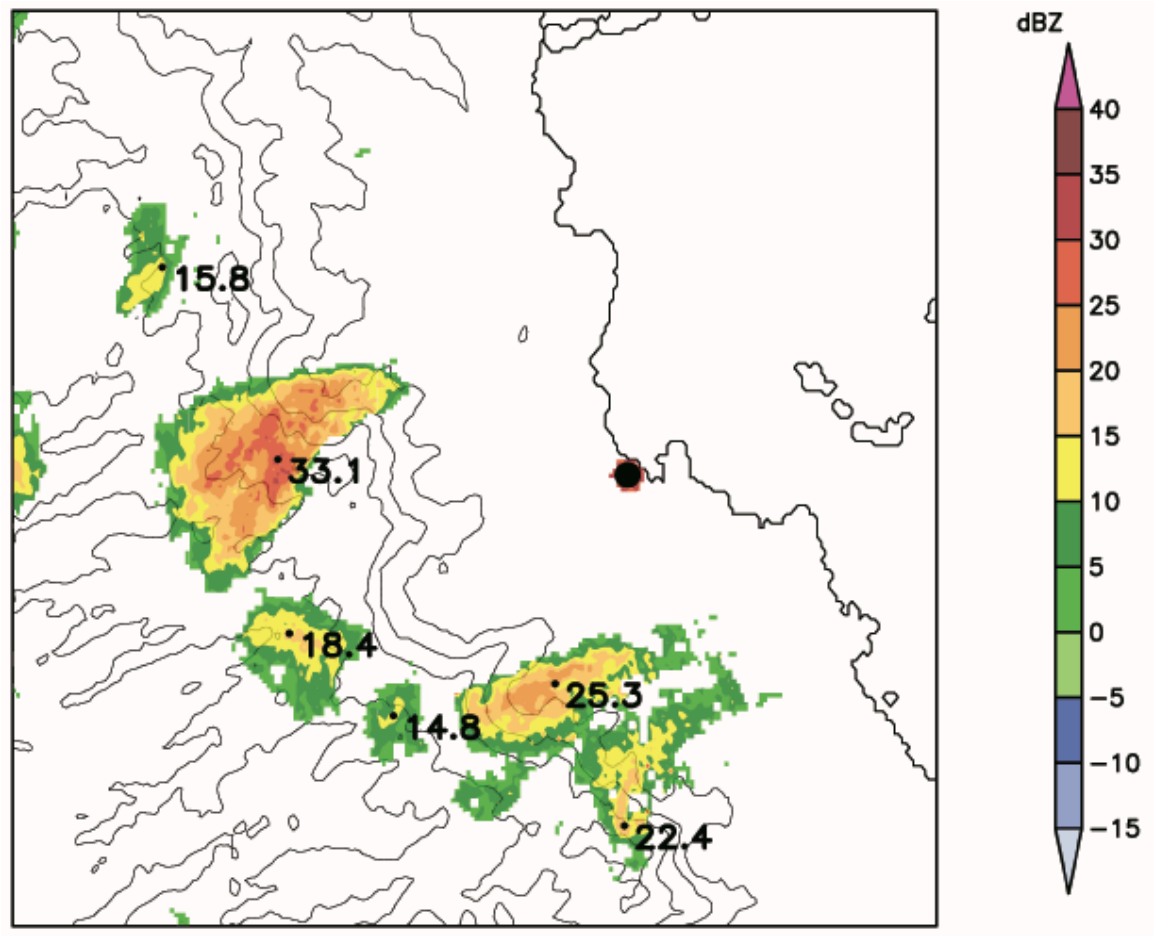

Fig 26 - Composite reflectivity from the DOW at 2138 UTC on 03 November 2013 near Kahaluʻu. The radar site is marked by a black dot outlined in red. Cell maximum reflectivities are marked with a dot and their reflectivity values are plotted to the right.

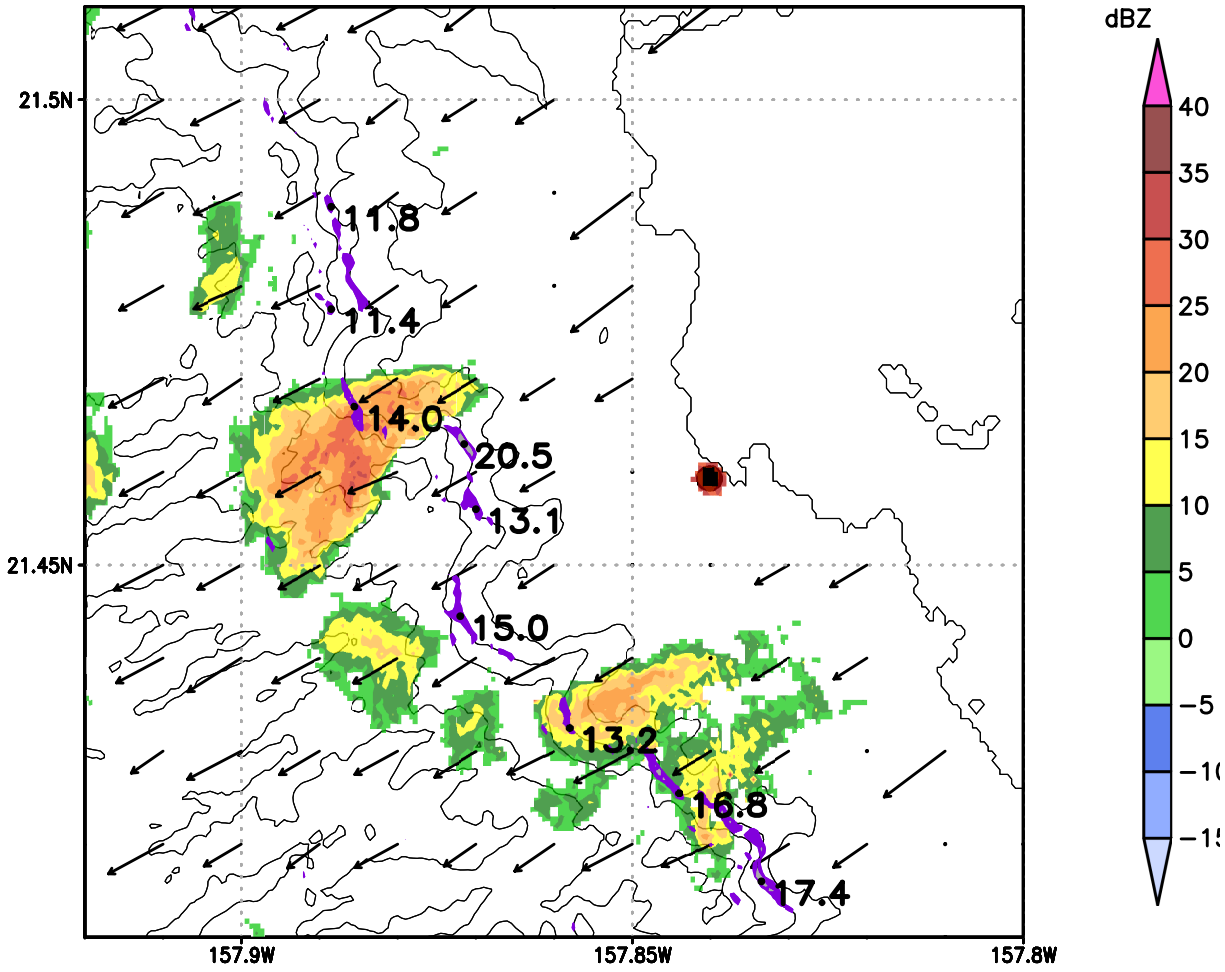

Fig 27 – Same as Fig 26, except with HOP vertical motion overlaid in purple (≥8 m s^{-1}) and gray (≥13 m s^{-1}), and black vectors scaled to the 10 m s^{-1} vector at the bottom derived from the 2140 UTC sounding used as the initial condition for the HOP model run. Vertical motion maxima in each 0.01° latitude rectangle are marked with a dot and their values are plotted.

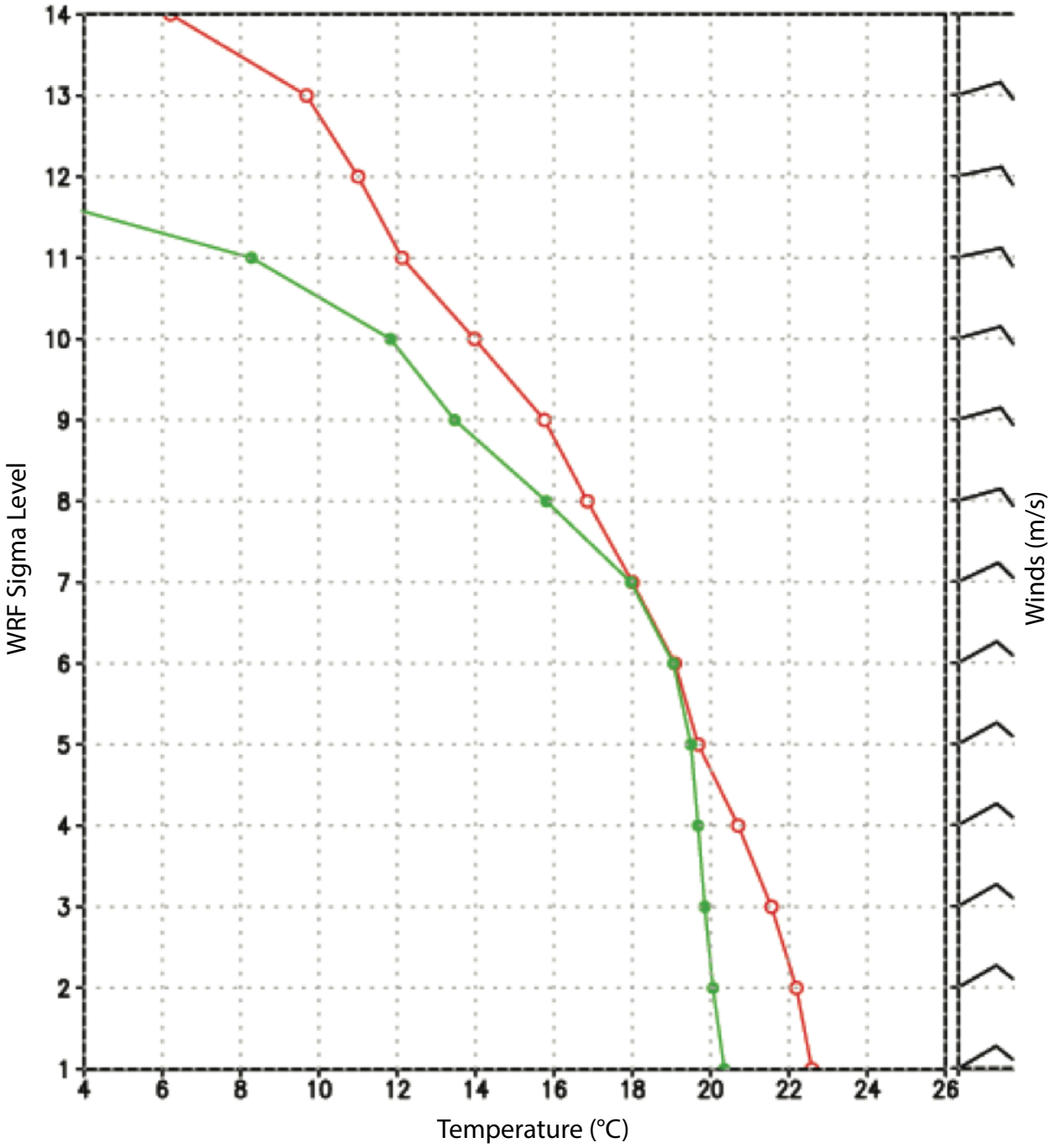

Fig 28 – Air temperature (red), dew point, (green), and wind profile at the DOW radar site on 03 November 2013 at 2100 UTC from the WRF model output. Each full line on the wind barb represents 10 m s^{-s}. The x-axis is temperature (°C) and y-axis is the WRF model sigma level.

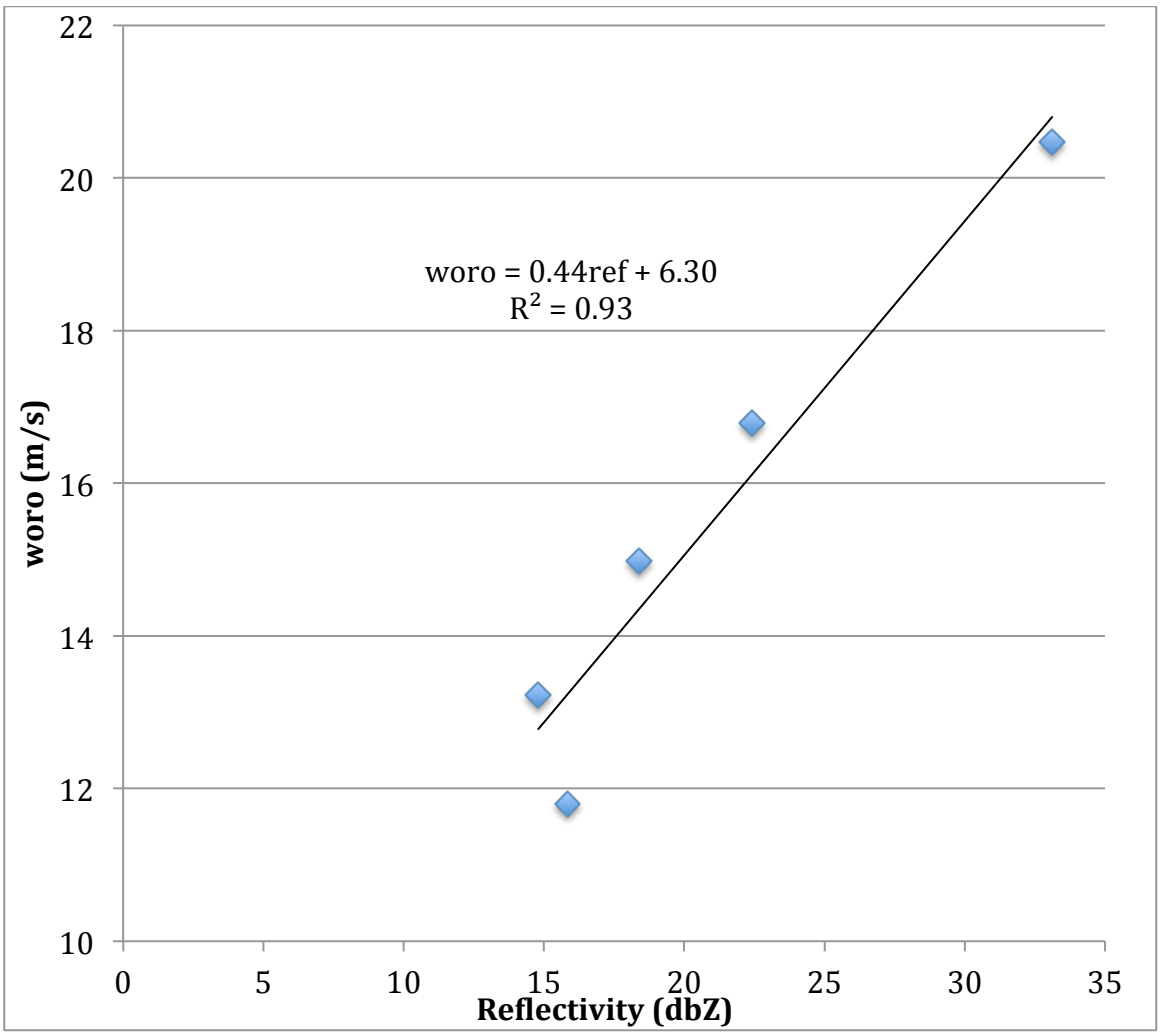

Fig 29 - Maximum vertical motion calculated from sounding winds (y-axis) and spatially corresponding maximum cell reflectivity (x-axis). The best-fit line is plot with the coefficient of determination (R^2) below the equation.

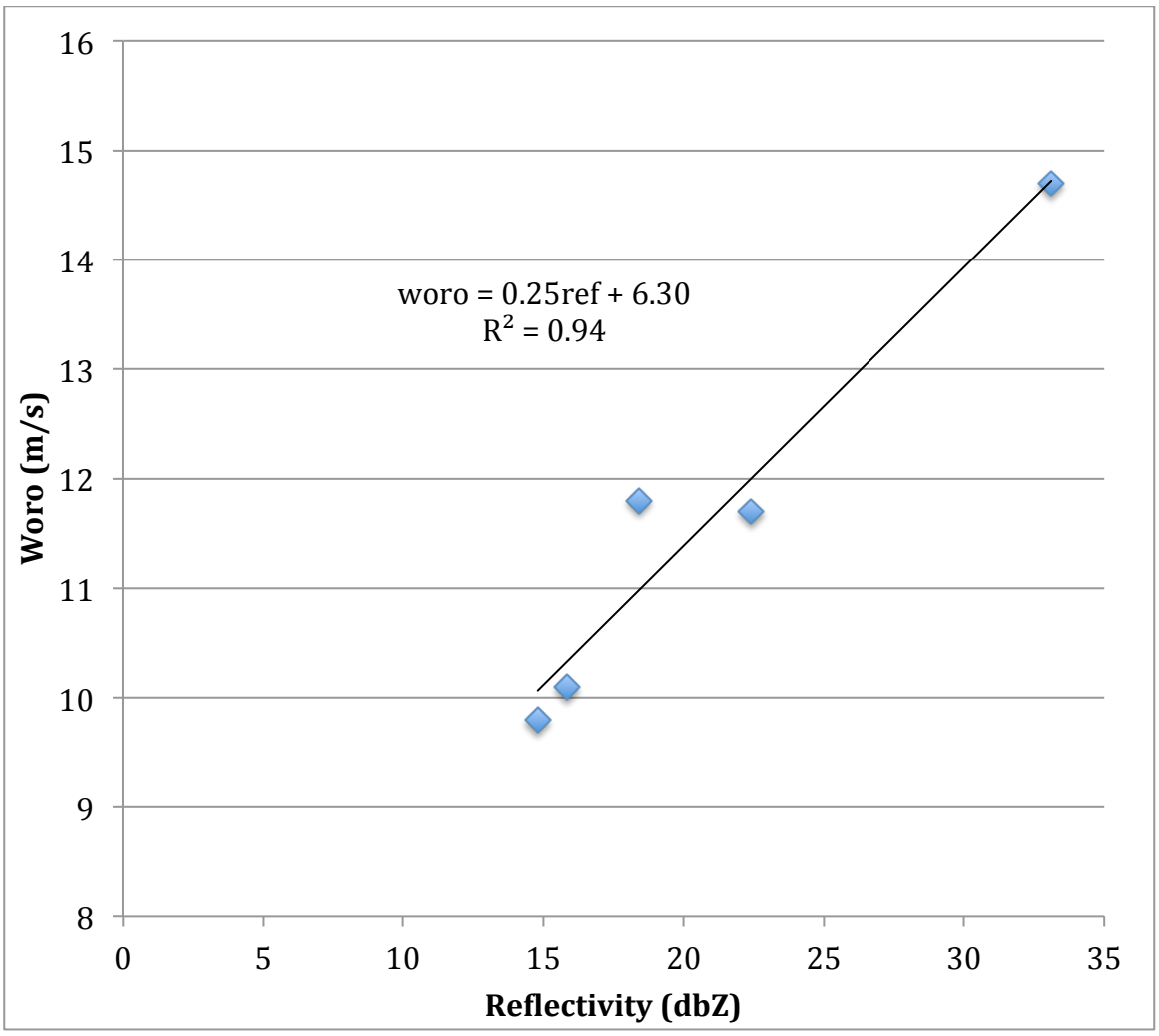

Fig 30 - Maximum vertical motion calculated from operational WRF lowest sigma level winds (y-axis) and spatially corresponding maximum cell reflectivity (x-axis). The best-fit line is plot with the coefficient of determination (R^2) below the equation.

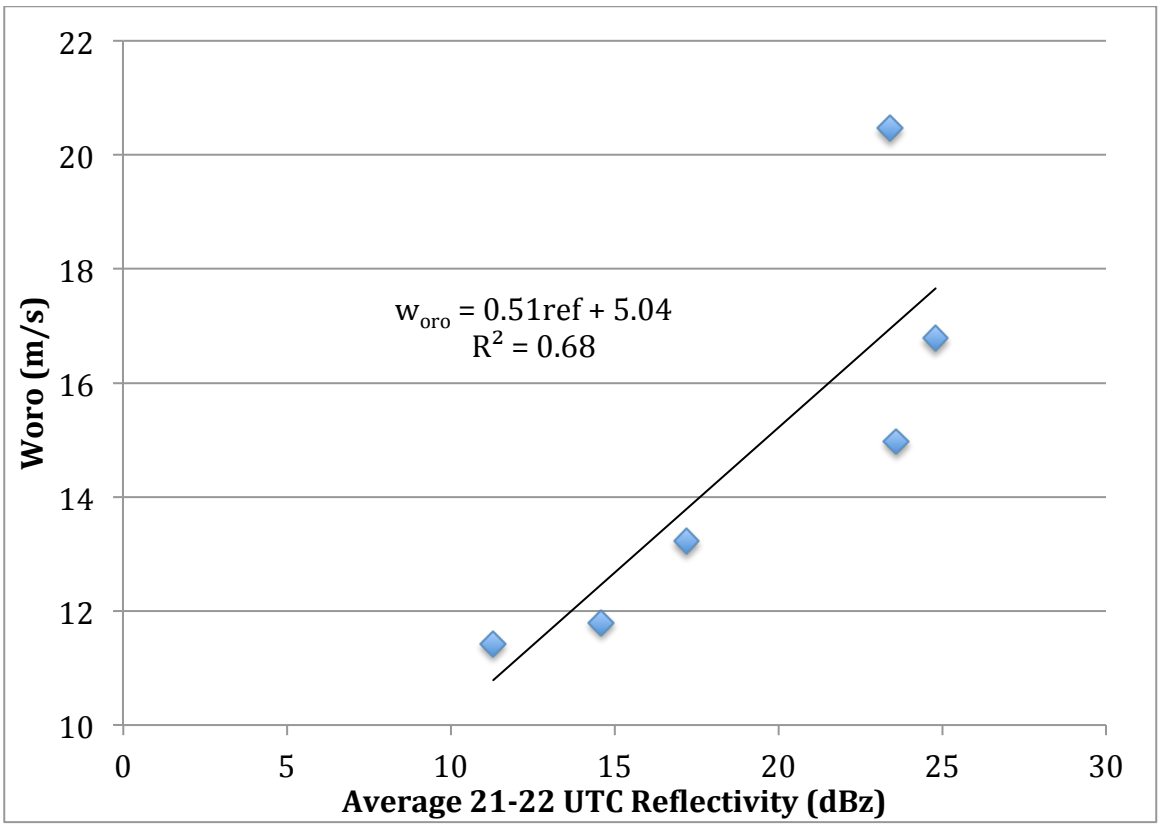

Fig 31 - Maximum vertical motion (y-axis) and down wind corresponding maximum average cell reflectivity (x-axis). The best-fit line is plot with the coefficient of determination (R^2) below the equation.

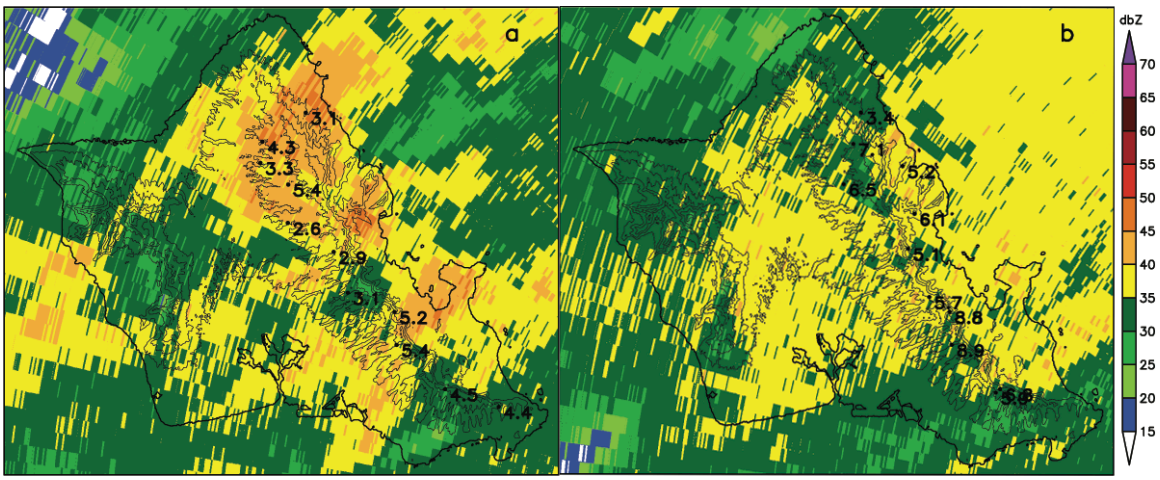

Fig 32 - 15 minute averaged radar reflectivity over Oahu on 24 August 2015 at a) 1500 UTC and b) 1600 UTC. Number values show maximum vertical motion calculated by the HOP model in each of the boxes from Fig 5.

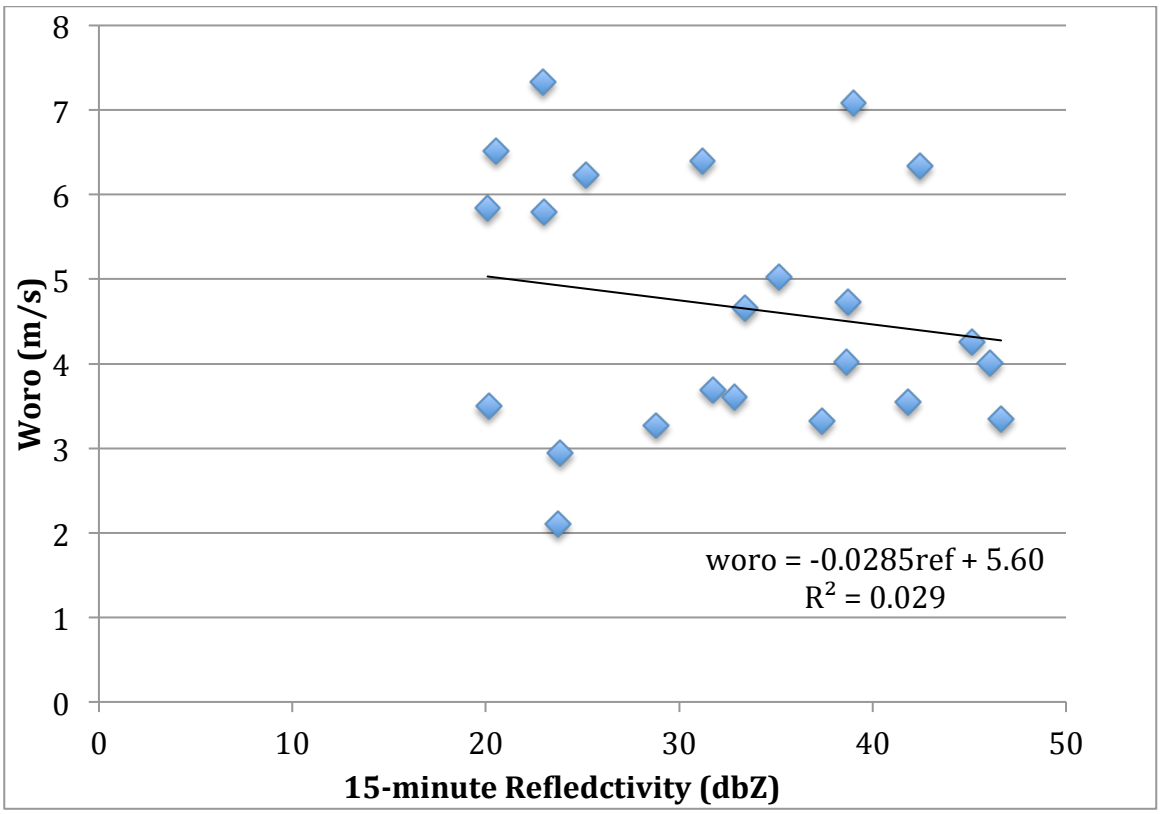

Fig 33 - Comparison of maximum HOP vertical motion averaged for a given time step and 15 minute averaged reflectivity maxima from boxes in figure 2 from 1 UTC on 24 August 2015 to 0 UTC 25 August 2015. The best-fit trend line is shown with its equation and the coefficient of determination (R^2) is displayed beneath the equation.

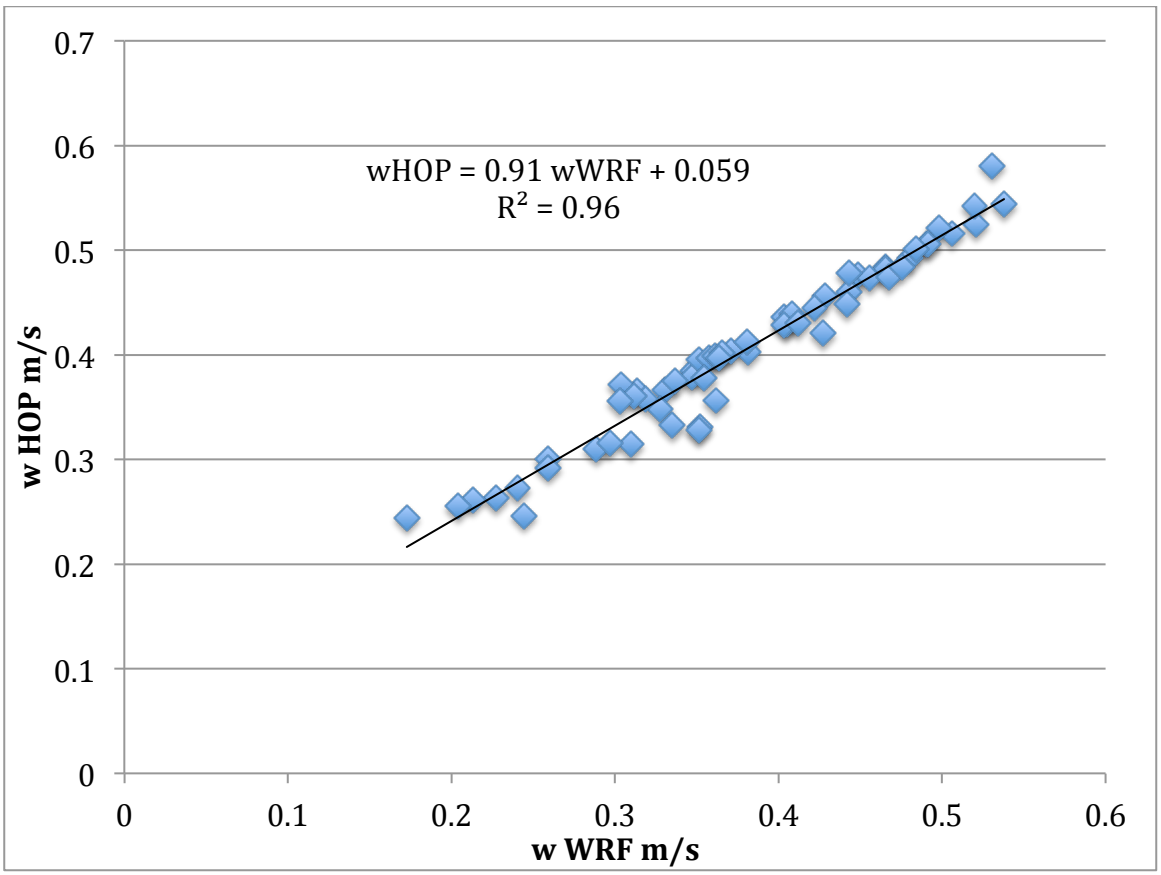

Fig 34 - Sixty hour comparison between the vertical motion from the WRF model (x-axis) and the vertical motion from the HOP model run at 3 km (y-axis) starting at 0 UTC on 01 November 2014 at 21.437 N, 157.859 W. The best-fit line is plotted with the coefficient of determination displayed beneath the line equation.

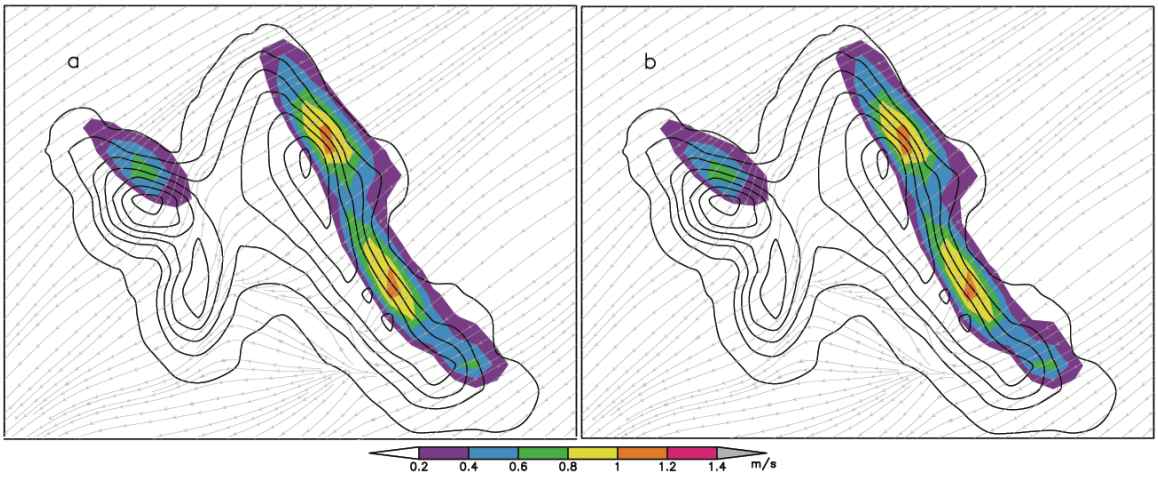

Fig 35 - Vertical motion (color) and wind streamlines for the a) low-resolution HOP model and b) lowest sigma level WRF model at 1500 UTC on 09 March 2012 over the island of Oahu using 3000 m resolution for both models.

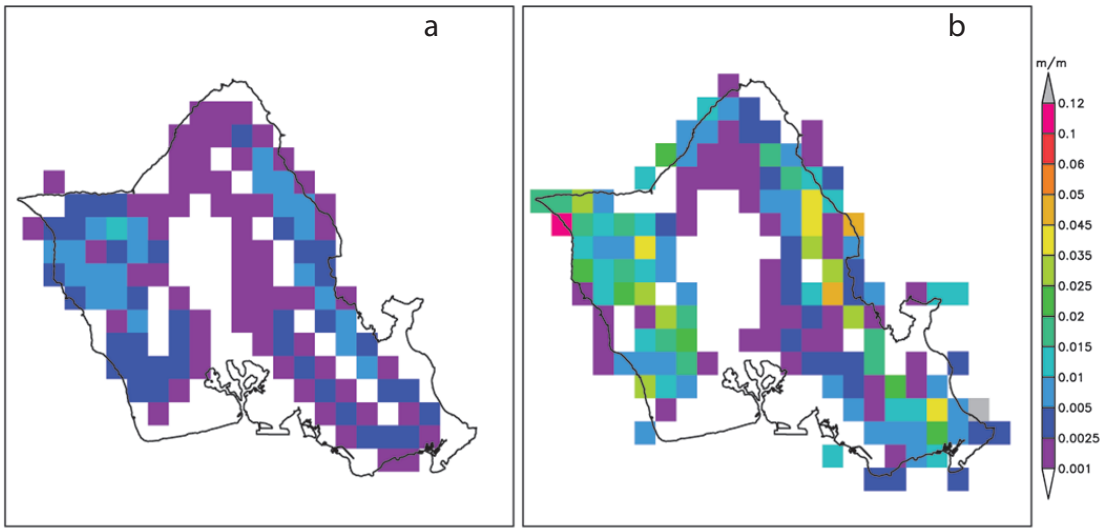

Fig 36 - Terrain gradient used at each grid point in WRF over Oahu for a) CTRL and b) EXP.

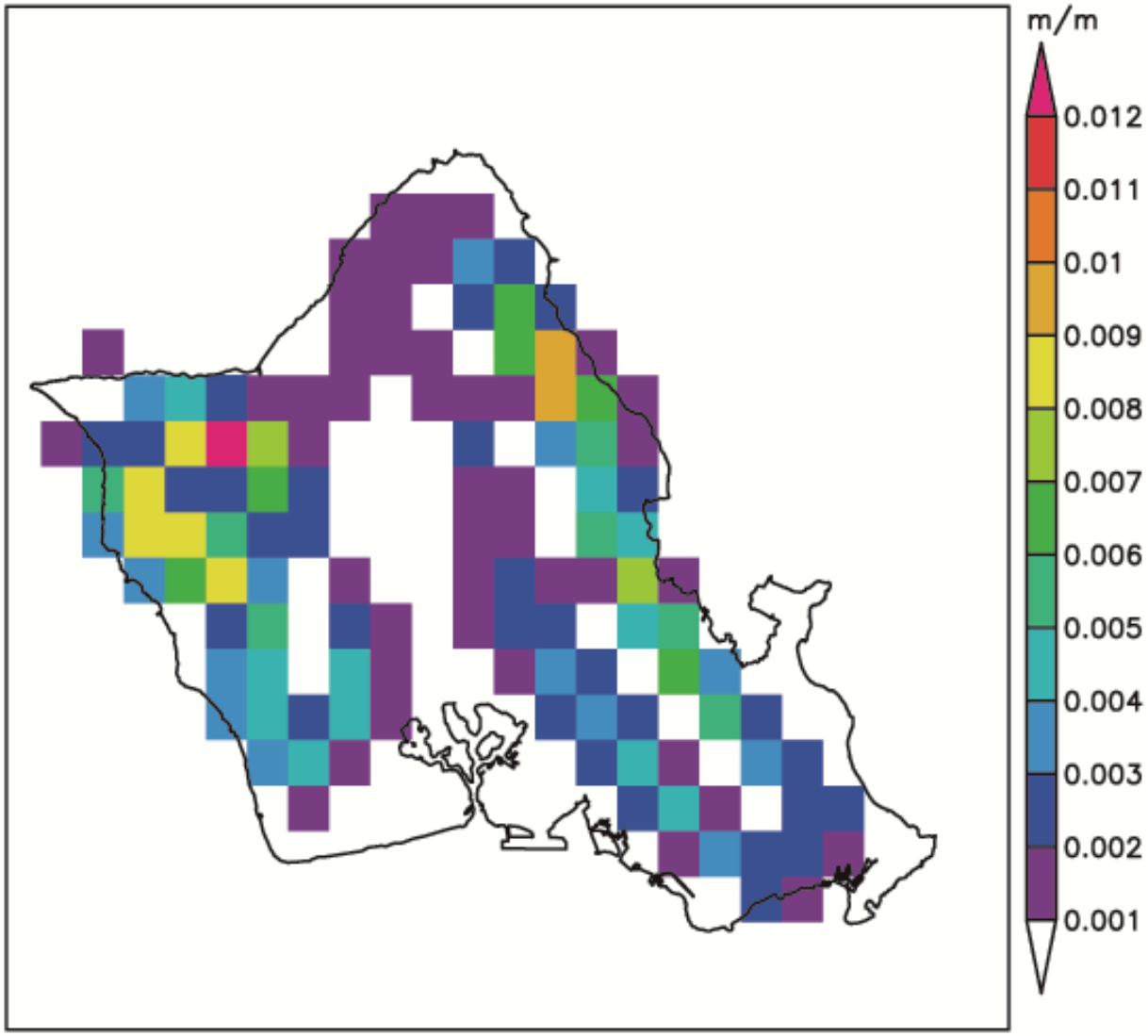

Fig 37 – WRF terrain gradient over Oahu in the CTRL model. The same as Fig 36a but with a different scale.

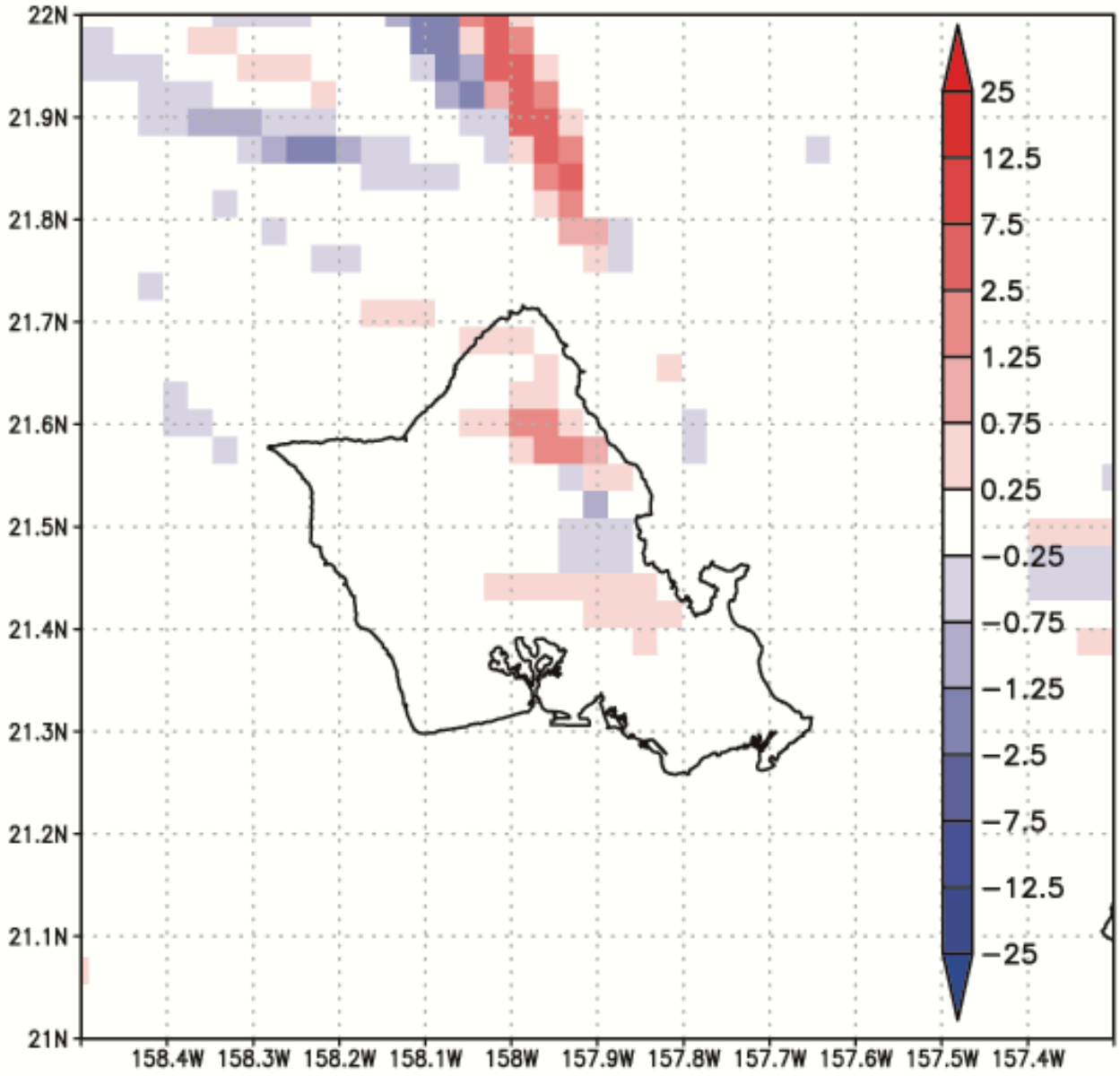

Fig 38 – Total precipitation difference (mm) between EXP and CTRL models over and around the Island of Oahu on 06 January 2016. Positive values indicate where the EXP model produced more precipitation than CTRL.

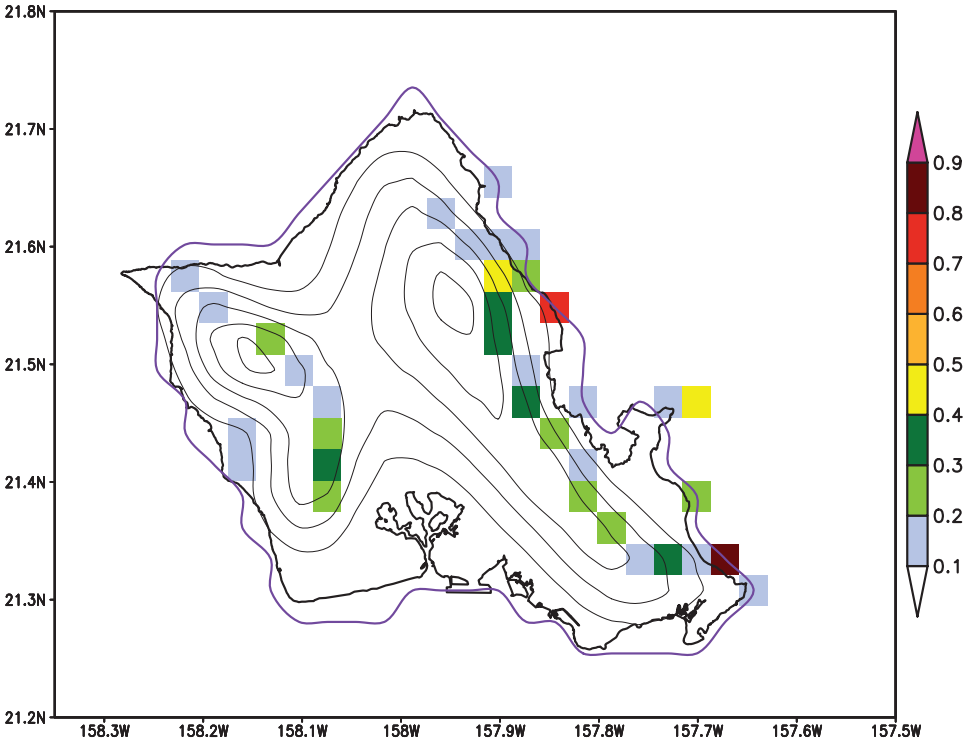

Fig 39 – Difference between the average vertical motion (m s^{-1}) from EXP minus CTRL showing positive values only over the Island of Oahu. Thick black line shows high-resolution coastline of the island, black contours occur every 100 m. The purple line represents the WRF model landmask.

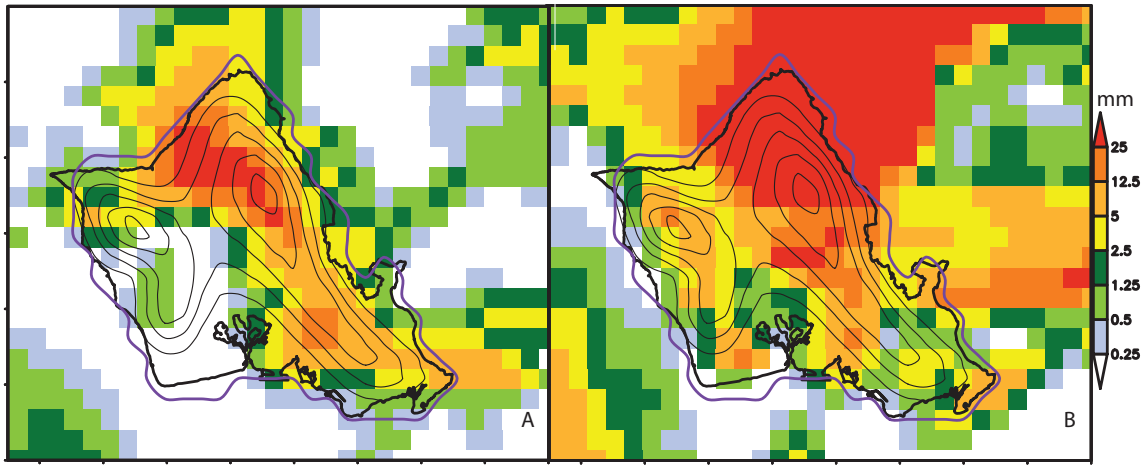

Fig 40 – Total precipitation (mm) from 0000 UTC to 1800 UTC from the WRF model for the A) EXP run and B) CTRL run over the Island of Oahu. The terrain lines are the same as in Fig 39.

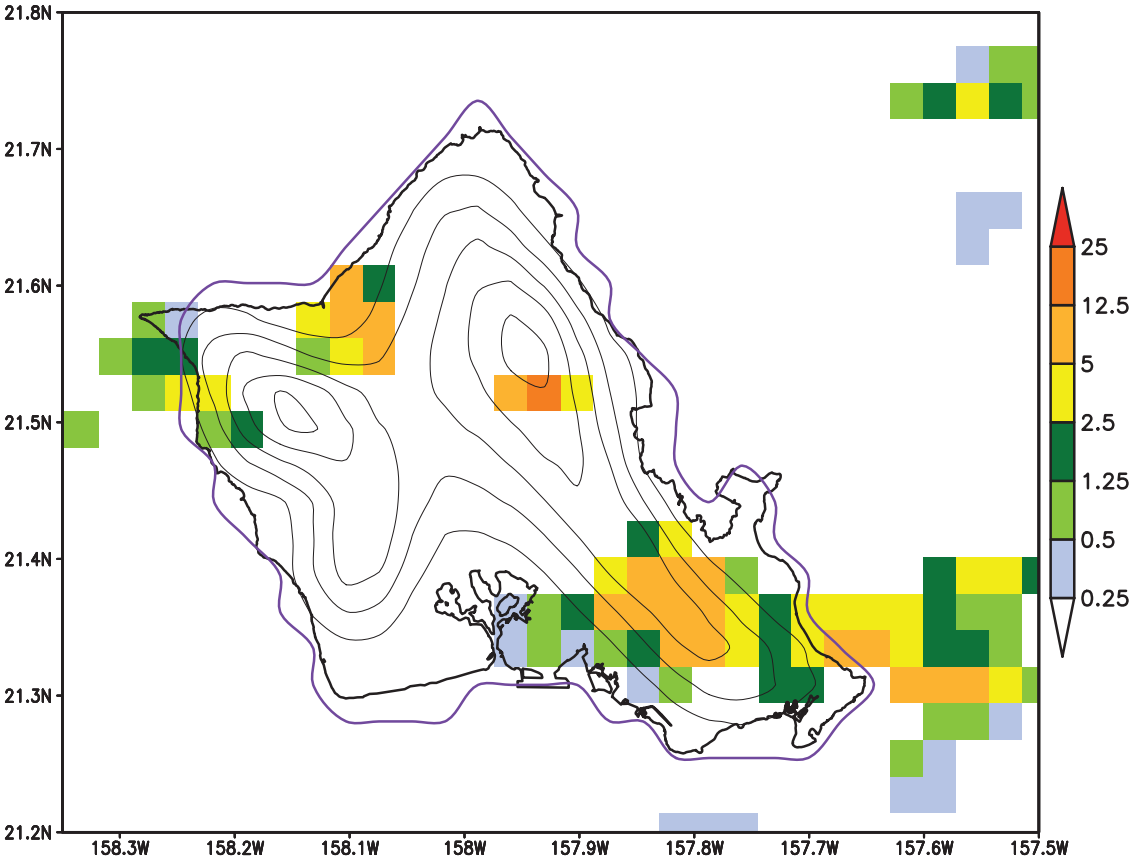

Fig 41 – The difference in total rainfall between EXP and CTRL from 0000 UTC to 1800 UTC showing positive values only. This is essentially Fig 40A minus Fig 40B. The terrain is the same as Fig 39.

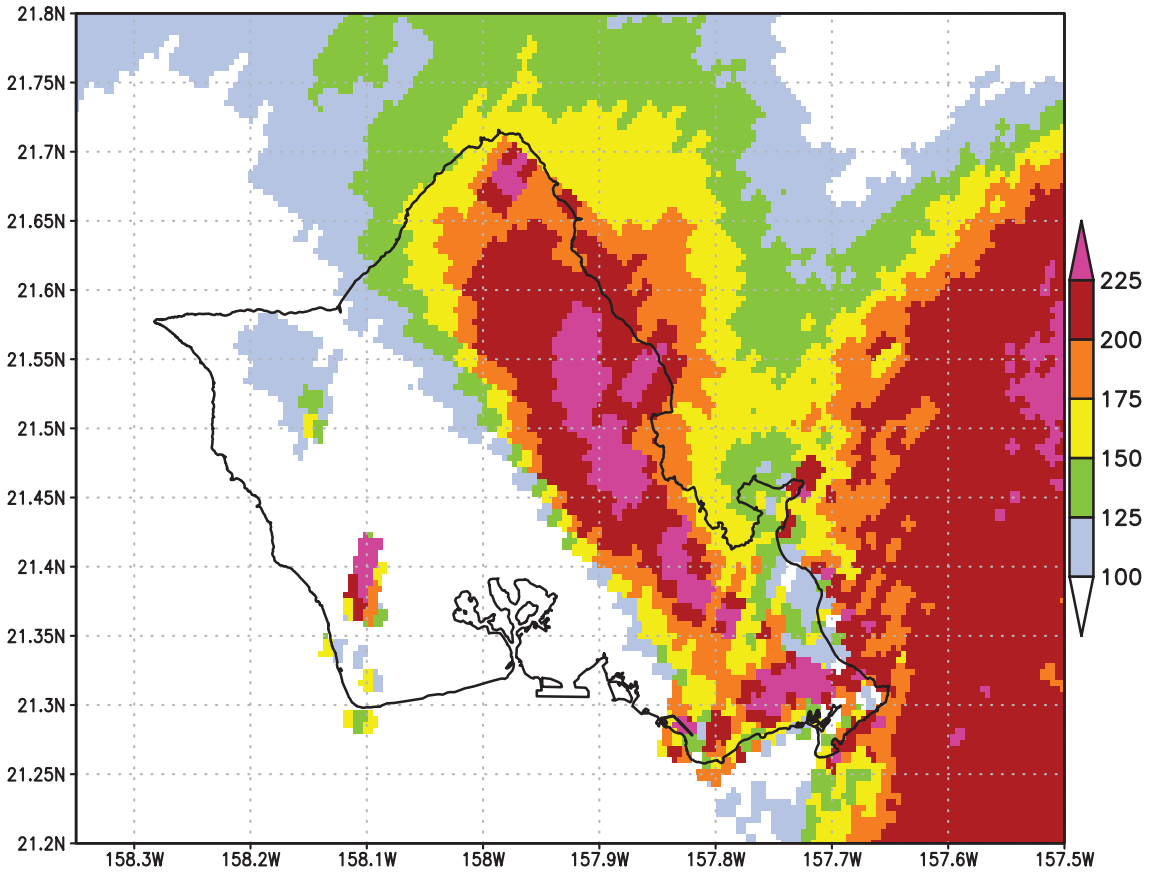

Fig 42 – Number of times a radar return of at least 0 dBZ occurred at a given point from 0003 UTC to 1801 UTC over the island of Oahu (outlined in black).

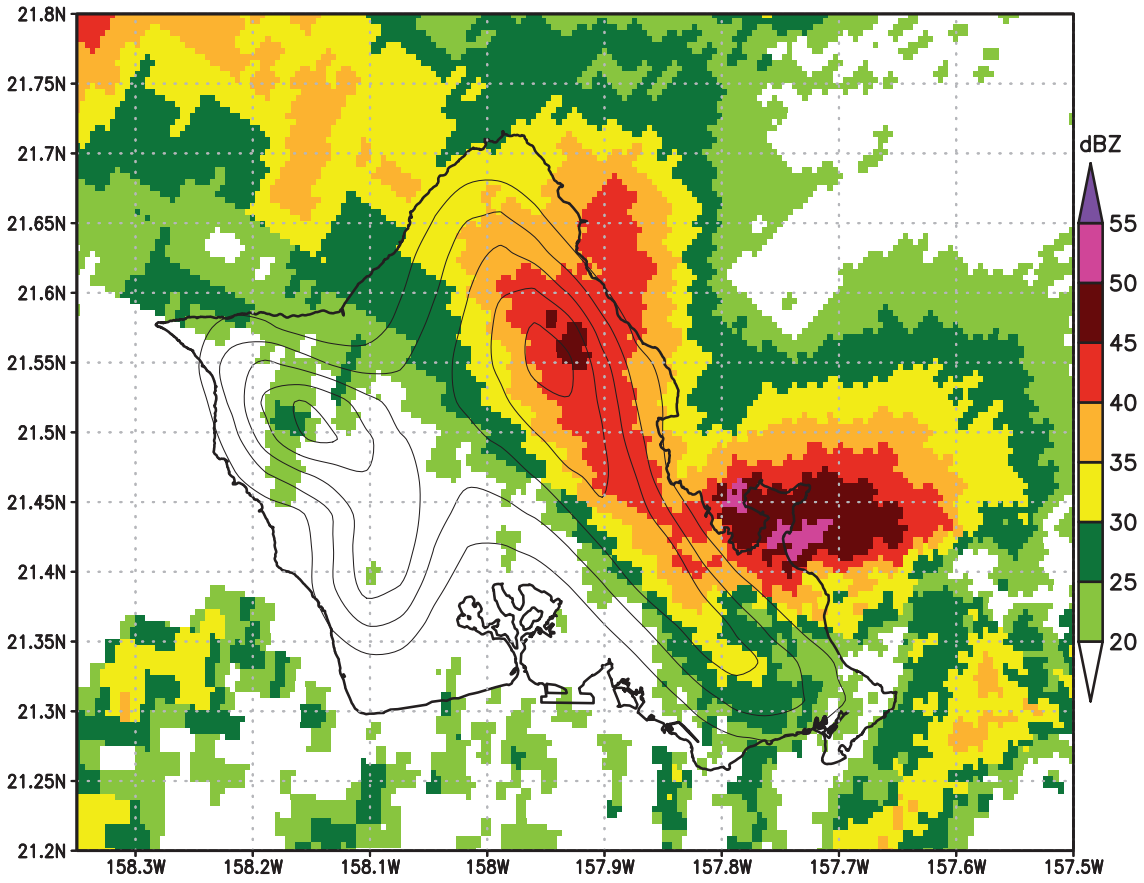

Fig 43 – Average radar reflectivity from PHMO over the Island of Oahu from 0003 UTC to 1801 UTC on 09 March 2012 with terrain contours from the WRF model every 100 m.

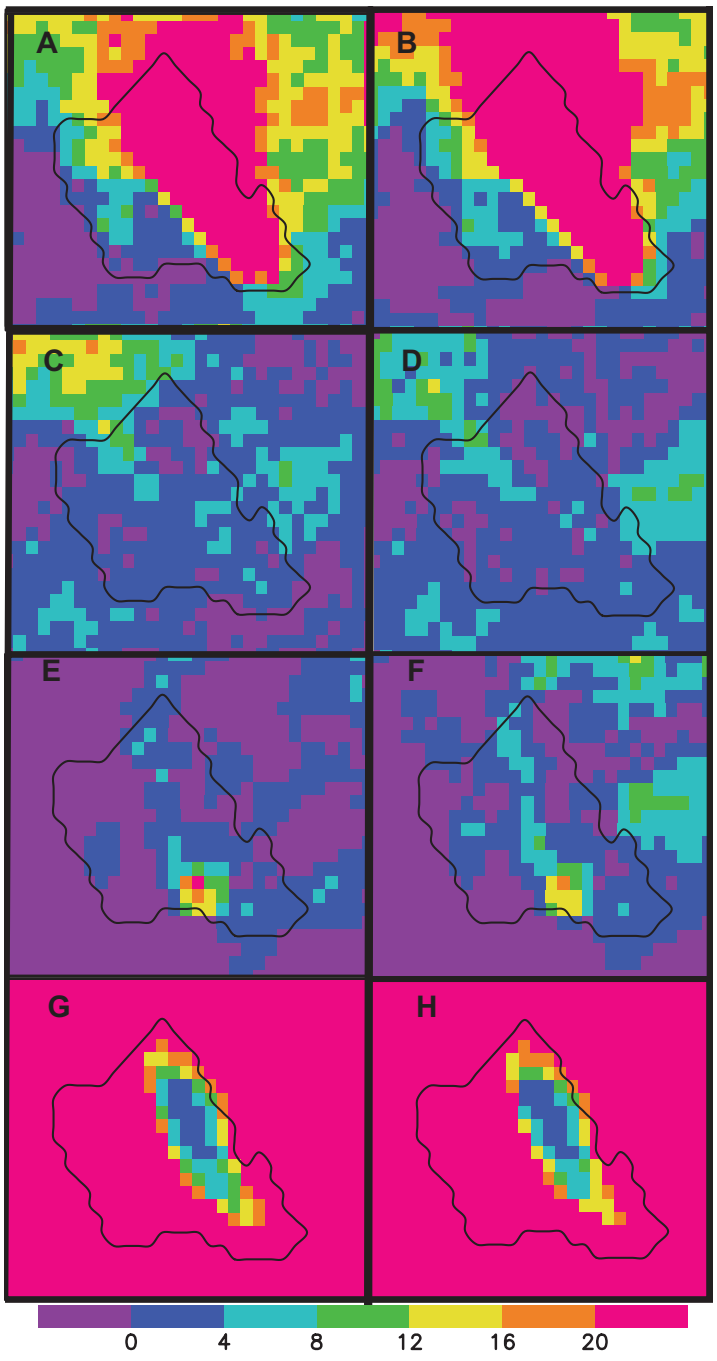

Fig 44 – Number of forecasts where A) The EXP run correctly predicted precipitation to occur (hit). B) Same as A but for the CTRL run. C) The EXP run predicted no precipitation, but precipitation did occur (miss). D) Same as C but for the CTRL run. E) The EXP run predicted precipitation, but the precipitation did not occur (false alarm). f) Same as E but for the CTRL

run. G) The EXP run correctly predicted no precipitation to occur (correct rejection). H) Same as G but for the CTRL run. The color bar at the bottom applies to all panels.

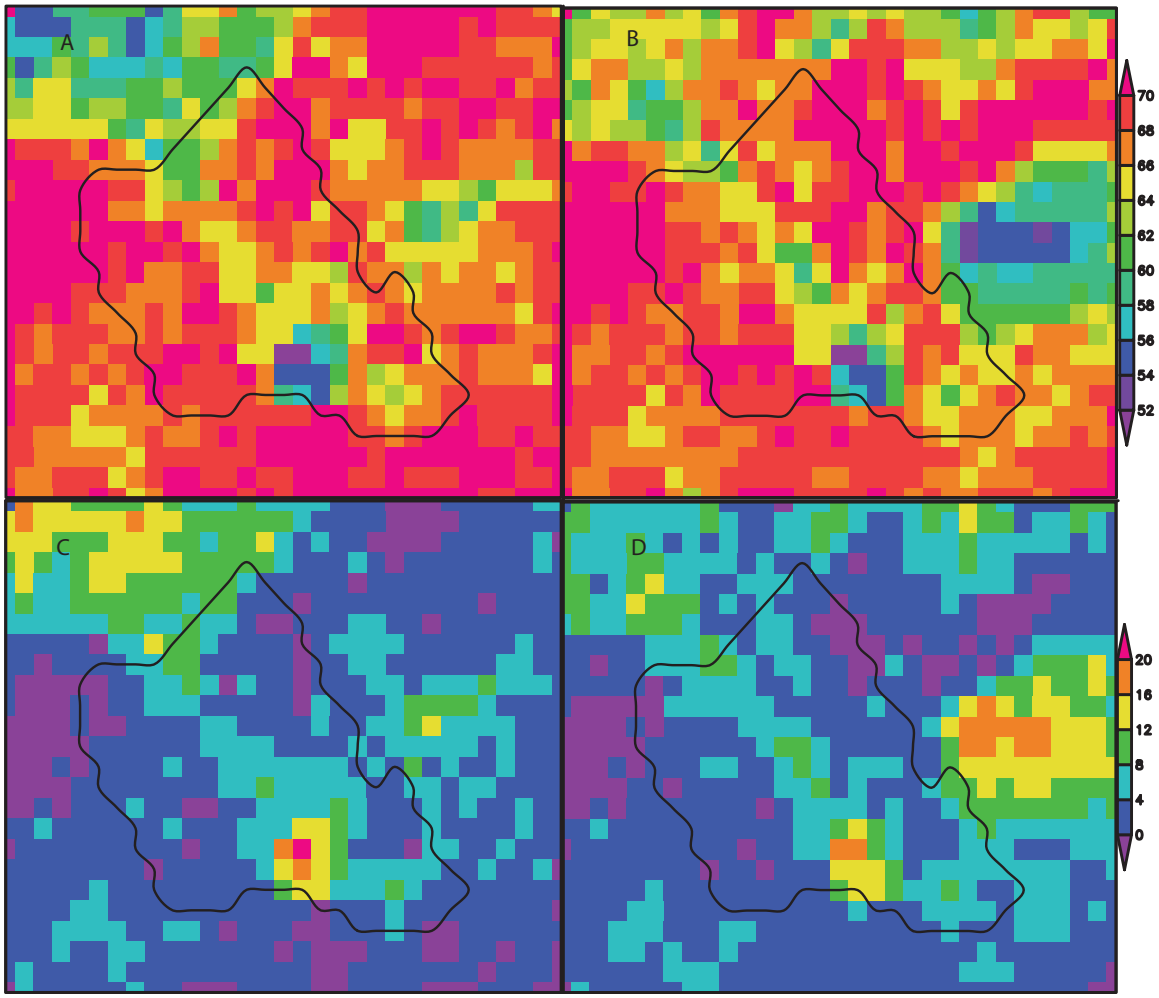

Fig 45 – A) Total number of correct precipitation forecasts from EXP. B) Same as A but from CTRL. C) Total number of incorrect forecasts from EXP. D) Same as C but from CTRL.